Journal of Physics:
Condensed Matter

TOPICAL REVIEW • OPEN ACCESS

Fundamentals of plane wave-based methods for energy band calculations in solids

To cite this article: Shengxin Yang *et al* 2025 *J. Phys.: Condens. Matter* **37** 233001

OPEN ACCESS
IOP Publishing
Journal of Physics: Condensed Matter
J. Phys.: Condens. Matter **37** (2025) 233001 (55pp)
https://doi.org/10.1088/1361-648X/adcf6b

Topical Review

Fundamentals of plane wave-based methods for energy band calculations in solids

Shengxin Yang, Kan-Hao Xue* and Xiangshui Miao

School of Integrated Circuits, Huazhong University of Science and Technology, Wuhan 430074, People's Republic of China

E-mail: xkh@hust.edu.cn

Received 7 December 2024, revised 10 April 2025
Accepted for publication 22 April 2025
Published 20 May 2025

Abstract

The plane-wave method with pseudopotentials has been the most widely used approach in solid-state electronic structure calculations. There is, however, usually a substantial gap from the fundamental physics to a practical code that could yield the detailed energy band structure for a solid. This review aims at giving a comprehensive introduction to the problem setting, fundamental strategy as well as various techniques involved in a typical plane-wave-based code. It starts from college quantum mechanics and ends up with some up-to-date topics such as the optimized norm-conserving Vanderbilt pseudopotential and the efficient diagonalization process of the Hamiltonian. It attempts to explain the mathematics and physics at the undergraduate level, and fundamental questions like 'why density functional theory', 'why plane wave basis' or 'why pseudopotential' are to be emphasized.

Keywords: density functional theory, band structure, eigenvalue, pseudopotential, plane-wave method, Hamiltonian diagonalization

1. The problem setting

The electronic energy band structure of a solid is of ultimate significance for its properties and functionalities. Consider, for example, a college-level example regarding the direct or indirect excitation in a semiconductor. It is well-known that silicon exhibits an indirect band gap [1], whose intrinsic valence band—conduction band excitation has to be accomplished with the assistance of phonons [2]. Consequently, direct band gap semiconductors, such as certain III–V semiconductor materials [3–6], are preferred in specific optoelectronic devices [7]. The electronic band diagram for a solid is usually given as continuous curves, but the following questions arise naturally. (i) What is the meaning of a band diagram? (ii) How is the band diagram exactly calculated? Regarding the relevant topics, several classic reviews have been published. Early in 1979, Ihm *et al* [8] established the momentum-space formalism for the total energy calculation in solids. The famous review by Payne *et al* emphasized the iterative minimization techniques for *ab initio* total energy calculations [9]. For density functional theory (DFT), a comprehensive review was given by Jones in 2015 [10], and some other reviews and books contain even more details [11–17]. With these works already available, the present paper aims at introducing the fundamental physical problems, classical or new techniques as well as a typical solution using plane waves in this respect, with the

---

[*] Author to whom any correspondence should be addressed.

contents *kept at an undergraduate level*. Hence, the starting point is college quantum mechanics, and particular emphasis has been placed on establishing rigorous problem definitions. Key challenges pertaining to numerical accuracy and computational efficiency are systematically elucidated through illustrative solution pathways.

1.1. The meaning of $\boldsymbol{k}$ *in a band diagram*

A band diagram is an E–k relation for a solid, where E is the electronic energy eigenvalue of a specified state, and k is the wavevector. A real solid is a three-dimensional (3D) object, thus k should become $\boldsymbol{k}$ to illustrate its vector nature. Nevertheless, it is very difficult to demonstrate a 3D vector on papers, thus one tends to draw the band diagrams only along several pre-determined k lines within the first Brillouin zone. It is for such convenience that k appears like a scalar in a band diagram. One of the cardinal tenets in quantum mechanics is the wave-particle duality, emanating from the de Broglie relations [18], *i.e.*

$$\begin{aligned} E &= \hbar\omega \\ \boldsymbol{p} &= \hbar\boldsymbol{k} \end{aligned} \quad . \tag{1-1}$$

Therefore, an electronic E–k relation naturally represents the ω–k relation for the 'matter wave' of the electron, which is named the dispersion relation. Any wave—be it sound, light or matter wave—should possess its own dispersion relation. By definition, the phase velocity of the wave is

$$v_p = \frac{\omega}{k} \tag{1-2}$$

where k is the modulus of $\boldsymbol{k}$. If many such waves constitute a wave packet, then the group velocity is defined as

$$v_g = \frac{\mathrm{d}\omega}{\mathrm{d}k} \tag{1-3}$$

and it should equal the velocity of the electron, provided that the electron may be described by a wave packet.

The dispersion relation is not specific to the electrons in a solid. Even in the simplest case, *i.e.* a free electron in one-dimension (1D), one can draw the dispersion relation. Figure 1 demonstrates a comparison regarding the electronic dispersion relation (the same as the band diagram, except for a constant $\hbar$ factor). The energy eigenstate of a free electron in 1D adopts the canonical plane wave form

$$\psi_k(x) = \mathrm{e}^{ikx} \tag{1-4}$$

where the temporal phase factor $\exp(-i\omega t)$ is intentionally omitted for brevity, and normalization is not yet considered at this juncture. Its dispersion relation is a parabola, under the non-relativistic assumption. It follows from the shape of figure 1(a) that, such dispersion relation has no limit for the magnitude of k. Moreover, the allowed values of k extend continuously on the real axis. In other words, all allowed k values constitute an uncountably infinite set, which can never be enumerated like $\{k_1, k_2, k_3, k_4, \ldots\}$. The quantity k has a definite physical meaning here, since $\hbar k$ is exactly the momentum eigenvalue of this plane wave. Even so, the entire set of allowed k values cannot cover all possible states for the free electron. These are merely the energy eigenstates. The electron is permitted to be in a superposition state, which may stem from two, three, 100, or even an infinite number of plane waves. Yet, plane waves are more important since they constitute the bases for all possible states. In a solid, one again cares more about the energy eigenstates for the electron. These states are named Bloch states [19, 20]. The dispersion relation representing the energy band diagram of a solid has a distinct appearance, like that in figure 1(b). Two salient features are immediately identified. On the one hand, the k values are restricted to the first Brillouin zone, no longer extending to infinity. On the other hand, each k value corresponds to an infinite set of energy eigenvalues, not merely one as in the 1D free electron case.

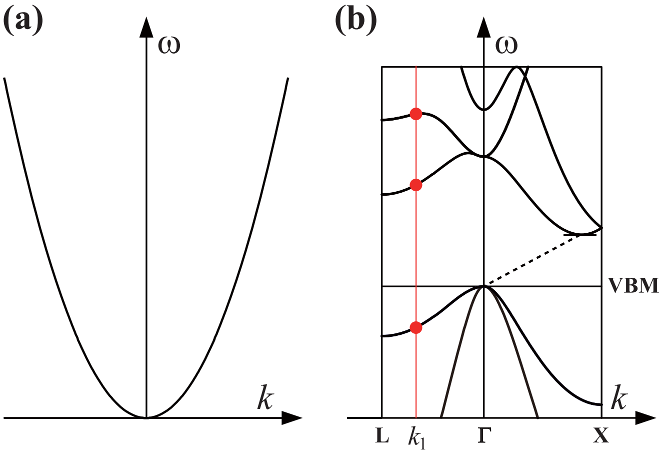

Figure 1. (a) The dispersion relation for a free electron in 1D; (b) dispersion relation (equivalent to band structure) for electrons in silicon, where a specific k point k_1 corresponds to multiple ω values and therefore multiple energy eigenvalues.

Additional special features of the band diagram can be revealed when considering its exact way of calculation. While the curves on the band diagram are continuous, actually only a few k points were calculated. The continuous curves are nothing but mathematical interpolation, for each band, between the energy eigenvalues belonging to these discrete k points [21, 22]. Moreover, the band structure computation does not follow the commonly misconceived 'band-wise' manner (*i.e.* sequential band tracing where the second band is processed only after the entire first band is obtained), which is analogous to electronic state-filling protocols. Instead, the eigensystem of each k point is computed in a single diagonalization step, with all k points processed independently. This scheme enables both (i) concurrent extraction of all eigenstates at a given k point, and (ii) complete computational independence among distinct k points. Such a 'k-resolved' methodology constitutes the prevailing paradigm in modern first-principles computational frameworks. Hence, a specific k point was selected in the beginning. Only subsequently, a limited but sufficient amount of energy eigenvalues at this k point, from the lowest to the highest, could be computed. To sum up, the key problem

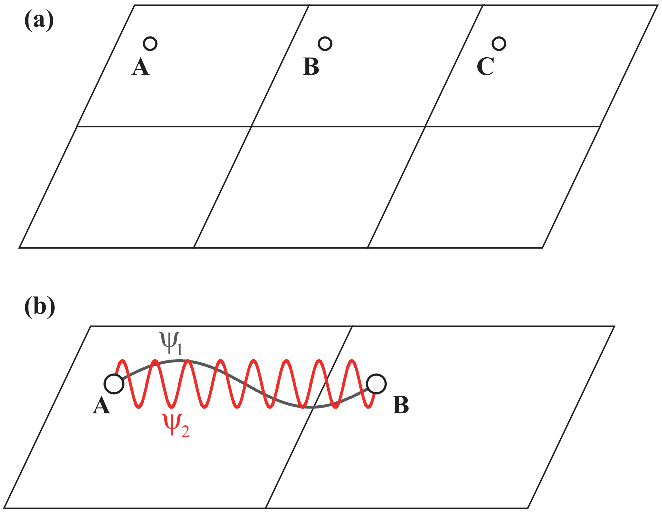

Figure 2. (a) Three equivalent locations in a periodic solid; (b) Bloch waves with very distinct expectations of the kinetic energy could share the same $\boldsymbol{k}$ point of the first Brillouin zone.

of energy band calculation is to obtain the electronic energy eigenvalues for any given k value in the first Brillouin zone. In this context, the meaning of k is an essential point for interpreting the band diagram and electronic structure in a solid.

Although k is well-known as the wavevector, and $\hbar k$ is defined as the 'crystal momentum', k is in fact an indication of the energy eigenvalue. This is clear when referring to college textbook examples such as the 1D infinite potential well [23], and can be generalized to extended systems. Under a stationary bound state in a 1D infinite potential well, $k = \sqrt{2mE}/\hbar$ is still a 'non-integer version' of the 'quantum number' for the energy, *i.e.* $k = n(\pi/a)$ where n is the true quantum number and a is the width of the well. However, $\hbar k$ is no longer the expectation value of the momentum operator, implying that k is an indicator of energy rather than momentum. Besides, in solids k has a more intuitive definition. A solid, actually an ideal crystal, is special in that it has translational symmetry. A small unit cell may be constructed, which repeats itself in 3D to generate the entire crystal. The periodicity requires that, any observable quantity, such as the electron density $n(\boldsymbol{r})$, must possess the same translational symmetry in any electronic energy eigenstate. Figure 2(a) illustrates three equivalent locations in adjacent unit cells, where the ideal crystal condition yields

$$n(\boldsymbol{r}_\mathrm{A}) = n(\boldsymbol{r}_\mathrm{B}) = n(\boldsymbol{r}_\mathrm{C}) \tag{1-5}$$

as long as electrons are in their stationary states. The same argument cannot be simply used for the wavefunction of a Bloch state in the solid, because the exact (complex) value of the wavefunction ψ is not measurable—only $|\psi|^2$ is measurable. Therefore, even if the normalization condition is considered, ψ is not uniquely defined due to an unknown phase factor. However, since $|\psi|^2$ is periodic, $\psi(\boldsymbol{r}_\mathrm{A})$ and $\psi(\boldsymbol{r}_\mathrm{B})$ at most differ by a phase factor $\exp(i\delta)$

$$\psi(\boldsymbol{r}_\mathrm{B}) = \psi(\boldsymbol{r}_\mathrm{A})\,\mathrm{e}^{i\delta}. \tag{1-6}$$

Meanwhile, the translational symmetry and the infinitely large crystal assumption lead to

$$\psi(\boldsymbol{r}_\mathrm{C}) = \psi(\boldsymbol{r}_\mathrm{B})\,\mathrm{e}^{i\delta} = \psi(\boldsymbol{r}_\mathrm{A})\,\mathrm{e}^{2i\delta}. \tag{1-7}$$

Hence, δ must be proportional to the distance of translation, thus a quantity k_x may be introduced such that

$$\psi(\boldsymbol{r}_\mathrm{B}) = \psi(\boldsymbol{r}_\mathrm{A})\,\mathrm{e}^{ik_x a} \tag{1-8}$$

where a is the lattice constant along the x-direction. The physical meaning of k_x is clear in that it characterizes how rapidly the phase factor of the wavefunction evolves, under translational operations along the a-axis of the crystal. Now if k_x is shifted by a reciprocal lattice constant G_x,

$$k_x \to k_x + G_x \tag{1-9}$$

then the same form is derived

$$\begin{aligned}\psi(\boldsymbol{r}_\mathrm{B}) &= \psi(\boldsymbol{r}_\mathrm{A})\,\mathrm{e}^{ik_x a}e^{2\pi i} = \psi(\boldsymbol{r}_\mathrm{A})\,\mathrm{e}^{ik_x a}\mathrm{e}^{iG_x a}\\ &= \psi(\boldsymbol{r}_\mathrm{A})\,\mathrm{e}^{i(k_x+G_x)a}.\end{aligned} \tag{1-10}$$

For this reason, a Bloch state in a solid is written as

$$\psi(\boldsymbol{r}) = u(\boldsymbol{r})\,\mathrm{e}^{i\boldsymbol{k}\cdot\boldsymbol{r}} \tag{1-11}$$

where $u(\boldsymbol{r})$ has the exact lattice periodicity. It turns out that when traversing from A to B, the same plane-wave-like factor $\exp(i\boldsymbol{k}\cdot\boldsymbol{r})$ is encountered, no matter whether starting from k_x or $k_x + G_x$ in the x-direction. However, the cases of k_x and $k_x + NG_x$ (N is an arbitrary non-zero integer) do differ because their $u(\boldsymbol{r})$ parts are different. In the example of figure 2(b), ψ_2 changes its phase with a faster speed than ψ_1 when moving from A to B, thus the average kinetic energy of ψ_2 is supposed to be higher than that of ψ_1.

It is now evident why the band diagram of a solid exhibits infinitely folded band structures within the Brillouin zone. A $\boldsymbol{k}$ point in the first Brillouin zone does not only point to a single possible $\boldsymbol{k}$ value. Rather, it represents a class of (unfolded) $\boldsymbol{k}$ values that go beyond the first Brillouin zone, and it corresponds to a class of energy eigenvalues. The rest $\boldsymbol{k}$ values outside the first Brillouin zone are typically linked to higher energy states, which are shifted into the first Brillouin zone by integer times of reciprocal basis vectors. Hence, in 1D infinite potential well, a k point directly indicates an energy eigenvalue through $E = \hbar^2 k^2/2m$ (m is the mass of the particle), but in a solid each $\boldsymbol{k}$ point in the first Brillouin zone is connected to an infinite number of energy eigenvalues. It is accordingly the aim of this paper to review the strategies to obtain these eigenvalues.

An additional comment should be given for the number of allowed $\boldsymbol{k}$ points in the first Brillouin zone of a solid. In the classical treatment, the crystal is first conceptualized as a finite system. The subsequent imposition of periodic boundary conditions [24] yields a discrete spectrum of permitted $\boldsymbol{k}$ values, mirroring the quantization mechanism in the 1D infinite potential well example. Yet, later the volume of the crystal goes to infinity. Then the $\boldsymbol{k}$ values become quasi-continuous, and there are infinitely many of them. Although this procedure finally yields an infinite number of $\boldsymbol{k}$ values, they constitute a countable set. This is intrinsically different from the 1D free electron case, and the key to this transformation lies in the restriction from boundary conditions.

1.2. The generic method to obtain the band structure

The energy band theory is a mean-field theory that adopts a one-electron perspective. The governing equation could be selected as an effective single-particle Schrödinger equation

$$\widehat{H}_{\text{eff}}\,\psi_{i,\boldsymbol{k}}(\boldsymbol{r}) = \varepsilon_{i,\boldsymbol{k}}\psi_{i,\boldsymbol{k}}(\boldsymbol{r}) \tag{1-12}$$

where

$$\widehat{H}_{\text{eff}} = -\left(\frac{\hbar^2}{2m_e}\right)\nabla^2 + V_{\text{eff}}(\boldsymbol{r}). \tag{1-13}$$

Here m_e is the mass of an electron, $\boldsymbol{k}$ is a pre-selected wavevector and $i = 1,2,3,\ldots$ denotes the band index. The uncertainty lies in the V_{eff} term, which is an effective potential that the electron feels, originating from the interactions with all the nuclei in the solid as well as all other electrons. There is no theory that can precisely tell the form of V_{eff} in a straightforward manner. Solid-state physicists tended to assume a mathematical form for V_{eff} according to physical intuition, in the early time. Chemists always require that V_{eff} is not from assumption, but it has to be calculated. Unfortunately, to derive V_{eff} for the electronic state $\psi_{i,\boldsymbol{k}}$, one has to know the exact conditions for all other electrons, which are yet to be determined. Hence, it was Hartree who first proposed to use a self-consistent field method [25], which involves a guess of V_{eff} in the beginning. However, after solving the single-particle Schrödinger equations for all the occupied states, one could compute a new V_{eff} term, which is different from that just used. This means that the calculation is not yet self-consistent. In principle, the new V_{eff} may be used to construct a new Schrödinger equation (in practice one usually mixes the old and new information, rather than simply using the new V_{eff}, cf section 4.4), which could be solved to generate the third version of V_{eff}. Repeating this process may finally achieve self-consistency, and V_{eff} is finally determined through computation rather than assumption. Although exchange and correlation effects were not considered in Hartree's original work, this self-consistent field concept holds ultimate significance and has been used until today. To sum up, V_{eff} may be assumed in one-time (non-self-consistent), or it could be calculated through iteration over and over again (self-consistent). In each case, one has to solve a Schrödinger equation like equation (1-12). In a non-self-consistent calculation, this equation is merely solved once. In a self-consistent calculation, this equation has to be solved for multiple times, each time with a different V_{eff}.

We leave the determination of V_{eff} to later discussions, but now it is high time to search for a generic method, in order to solve a given equation (1-12). The classical strategy to solve a partial differential equation is

(i) to transform the equation into several ordinary differential equations, through separation of variables;
(ii) find the solutions to these ordinary differential equations, usually by checking the mathematical handbooks.

Nevertheless, there is no guarantee that such methodology could work for a complicated effective potential in a solid, and it is not applicable to a general-purpose code that aims at obtaining the band structures for all kinds of solids. Hence, one has to resort to the series method, which originated from the French mathematician Fourier, who tried to solve the heat conduction equation in the early 19th century. For an effective Hamiltonian like equation (1-13), a generic method below could be proposed to derive its eigenvalues.

(i) Select a proper set of basis for the electronic state, labeled as $|\phi_1\rangle, |\phi_2\rangle, |\phi_3\rangle, \ldots$, which are orthonormal. This is feasible for a bound state, because the dimension of the Hilbert space will be countably infinite.
(ii) Truncate the basis set and only keep the first N terms $|\phi_1\rangle, |\phi_2\rangle, |\phi_3\rangle, \ldots |\phi_N\rangle$. The value of N must be sufficiently large such that the error caused by neglecting the remaining basis states is not significant.
(iii) Set up a new representation using the set of these N bases, and the Hamiltonian could be expressed as an $N \times N$ matrix (we use bold font to denote matrices and vectors in this work)

$$\boldsymbol{H}_{\text{eff}} = \begin{bmatrix} \langle\phi_1|\widehat{H}_{\text{eff}}|\phi_1\rangle & \langle\phi_1|\widehat{H}_{\text{eff}}|\phi_2\rangle & \langle\phi_1|\widehat{H}_{\text{eff}}|\phi_3\rangle & \cdots & \langle\phi_1|\widehat{H}_{\text{eff}}|\phi_N\rangle \\ \langle\phi_2|\widehat{H}_{\text{eff}}|\phi_1\rangle & \langle\phi_2|\widehat{H}_{\text{eff}}|\phi_2\rangle & \langle\phi_2|\widehat{H}_{\text{eff}}|\phi_3\rangle & \cdots & \langle\phi_2|\widehat{H}_{\text{eff}}|\phi_N\rangle \\ \langle\phi_3|\widehat{H}_{\text{eff}}|\phi_1\rangle & \langle\phi_3|\widehat{H}_{\text{eff}}|\phi_2\rangle & \langle\phi_3|\widehat{H}_{\text{eff}}|\phi_3\rangle & \cdots & \langle\phi_3|\widehat{H}_{\text{eff}}|\phi_N\rangle \\ \vdots & \vdots & \vdots & \ddots & \vdots \\ \langle\phi_N|\widehat{H}_{\text{eff}}|\phi_1\rangle & \langle\phi_N|\widehat{H}_{\text{eff}}|\phi_2\rangle & \langle\phi_N|\widehat{H}_{\text{eff}}|\phi_3\rangle & \cdots & \langle\phi_N|\widehat{H}_{\text{eff}}|\phi_N\rangle \end{bmatrix}. \tag{1-14}$$

Since $\widehat{H}_{\text{eff}}$ was originally written within the position representation, and each basis vector has its own wavefunction, any matrix element could be obtained through an integration over the real space. For instance,

$$\langle\phi_2|\widehat{H}_{\text{eff}}|\phi_3\rangle = \int_{\infty} \mathrm{d}\boldsymbol{r}\phi_2^*(\boldsymbol{r})\widehat{H}_{\text{eff}}\,\phi_3(\boldsymbol{r})\,. \tag{1-15}$$

(iv) A unitary transformation matrix $\boldsymbol{S}$ could be identified, by computers, to diagonalize $\boldsymbol{H}_{\text{eff}}$

$$\boldsymbol{S}^{\dagger}\boldsymbol{H}_{\text{eff}}\boldsymbol{S} = \begin{bmatrix} \varepsilon_1 & 0 & 0 & \cdots & 0 \\ 0 & \varepsilon_2 & 0 & \cdots & 0 \\ 0 & 0 & \varepsilon_3 & \cdots & 0 \\ \vdots & \vdots & \vdots & \ddots & \vdots \\ 0 & 0 & 0 & \cdots & \varepsilon_N \end{bmatrix} \tag{1-16}$$

and the diagonal matrix elements are exactly the energy eigenvalues.

This is the most fundamental principle to obtain the energy eigenvalues for a specific $\boldsymbol{k}$ point, but the practical implementation is far more complicated. Several issues remain, such as how to find the proper basis set and why the truncation makes sense, and note that the direct diagonalization of $\boldsymbol{H}_{\text{eff}}$ could be extremely time-consuming when the basis set is large (*i.e.* N is big). The relevant techniques to resolve these issues will be reviewed below.

2. Techniques and the relevant reasonings

There are several aspects of the problem that deserve in-depth discussions. First of all, a proper basis set is required [26], which allows for convenient truncation, and it is up to the user to prefer accuracy (keeping more terms) or speed (keeping less terms). Secondly, algorithm for the diagonalization of the Hamiltonian must be optimized. However, before considering these techniques, it is worthwhile to note that self-consistent calculation of energy band structures is already the prevailing solution nowadays [27, 28], due to its intrinsically predictive nature (from first principles) and its capability of handling unknown materials. This feature is of increasing significance because the spirit of material genome engineering [29] is prevailing nowadays in new material design. Hence, the method of determining V_{eff} will be reviewed first, which involves the celebrated DFT.

2.1. Why DFT?

Provided that one needs to find V_{eff} through calculation, it is the first question to ponder: why it is not straightforwardly available? This is because one starts from the effective one-electron equation. In the original many-electron Schrödinger equation with a complicated multiple-electron wavefunction, the potential term is ready since it comes from the given external potential (sometimes absent) plus the nucleus potential, where all the nuclei are regarded as fixed after the Born-Oppenheimer approximation [30]. Following the convention of DFT, we shall merge the two types of potentials, and henceforth the term ‘external potential’ includes all contributions from the nuclei. However, it is almost impossible to obtain the multiple-electron wavefunction accurately. Electrons have interactions with each other, and it is improper to use separation of variables for such a correlated problem. The complexity in obtaining the multiple-electron determinant wavefunctions is formidable when there are many electrons involved. No direct way is afforded to guess the effective potential that a single electron feels, from the original many-electron Schrödinger equation. In the case of non-self-consistent band structure calculations, this is not a big problem since V_{eff} may be obtained through fitting to experimental data [22, 31], and its mathematical form is intrinsically by assumption and physical intuition. In self-consistent calculations, however, the derivation protocol of V_{eff} dictates the ultimate computational accuracy, given that the basis set can be made arbitrarily complete.

In history, DFT [32, 33] was not originally designed for carrying out the one-electron approximation, but it has become the standard now. Originally, DFT was about using electron density n, instead of the wavefunction, to describe the ground state of a solid or a molecule. An even earlier attempt was given, independently by Thomas [34] as well as Fermi [35], but the so-called Thomas-Fermi method suffers from accuracy problems, even after the inclusion of exchange by Dirac [36] and the gradient correction by Weizsäcker [37]. Hohenberg and Kohn [32] first proved a one-to-one correspondence between the (non-degenerate) ground state electron density and the external field, for a given solid (a generalization of the theorem to degenerate ground states was given later by Levy [38]). Hence, even if one has no knowledge about the electronic wavefunctions, the entire information regarding ground state $n(\boldsymbol{r})$ already hints at all the definite properties of this solid. Of course, to extract these information from $n(\boldsymbol{r})$ still seems to be a formidable task, especially regarding the kinetic energy. Kohn and Sham realized [33], probably partly from the inaccuracy of the Thomas–Fermi method, that the kinetic energy operator should not be abandoned. That is to say, one still needs the wavefunction, but not the multiple-electron wavefunction. One-electron wavefunction seems to be a good choice to extract at least most of the kinetic energy information. Hence, Kohn and Sham proposed a new ansatz in 1965 [33], that one can always set up a model system that has the same ground state electron density as the prototype system, but in the model system there is no electron correlation. In other words, the ansatz of Kohn and Sham was that, one can do independent-particle approximation for the model system, while the difference between the two systems will be captured by another term in the total energy expression. The total kinetic energy (T_s) in the model system is readily available, once one obtains the one-electron wavefunctions, but T_s is not equal to the total electronic kinetic energy (T) in the prototype system. An exchange-correlation energy term (E_{XC}) is included in the total energy expression of the prototype system, which has three components.

- The exchange energy that must be considered when doing one-electron approximation, which only exists for electrons with parallel spin;
- The correlation energy, which is mainly for electrons with opposite spins but also exists for electrons with parallel spin;
- The difference in total electronic kinetic energy between the prototype system and the Kohn-Sham auxiliary system, *i.e.* T–T_s.

The surprising discovery is that, putting the three difficult terms together, the resulting E_{XC} term, which is a very complicated functional of $n(\boldsymbol{r})$, can usually be approximated as

$$E_{\mathrm{XC}}\left[n\left(\boldsymbol{r}\right)\right] \approx \int \mathrm{d}\boldsymbol{r}\epsilon_{\mathrm{XC}}\left(n\left(\boldsymbol{r}\right)\right)n\left(\boldsymbol{r}\right) \qquad (2\text{-}1)$$

without losing the computational accuracy seriously in most cases. Here ϵ_{XC} is an exchange-correlation energy density term, representing the exchange-correlation energy per electron. This approximation transforms the intricate functional $E_{\mathrm{XC}}\left[n\left(\boldsymbol{r}\right)\right]$ to a much simpler function $\epsilon_{\mathrm{XC}}\left(n\right)$, and is named the local density approximation (LDA) because ϵ_{XC} is merely an ordinary function of the local electron density n. We write $\epsilon_{\mathrm{XC}}\left(n\left(\boldsymbol{r}\right)\right)$ instead of $\epsilon_{\mathrm{XC}}\left[n\left(\boldsymbol{r}\right)\right]$ in order to emphasize that it is not a functional. The approximate function form of $\epsilon_{\mathrm{XC}}\left(n\right)$ can be derived based on the simulation to the uniform electron gas model [39], or through interpolation [40]. More elaborate approximations beyond LDA have also be proposed [41–46], with wide usage nowadays. The Kohn-Sham ansatz cannot be proven, but the empirical success of DFT supports its feasibility *a posteriori*. For our purpose, the Kohn-Sham ansatz has provided a proper way of doing the one-electron approximation, that is, such approximation should be done only for the model system where electrons are uncorrelated. As long as E_{XC} is sufficiently accurate, the one-electron approximation would make sense, and the intrinsic accuracy of the calculated band structure relies on the quality of E_{XC}.

By establishing a rigorous foundation for the one-electron approximation, DFT has become the cornerstone of modern self-consistent electronic structure calculations in solids. This has nothing to do with the basis selection. For example, WIEN2k [47] is an all-electron code that uses augmented plane-waves (APWs) plus local orbitals, while Siesta [48] is a pseudopotential-based code using localized bases; both codes nevertheless use DFT for the description of exchange and correlation effects, which are important for the accuracy regarding one-electron approximation. The popularity of DFT in self-consistent band structure calculations is already well-known [49–52].

An apparent distinction exists between non-self-consistent and self-consistent band structure calculations. For the former, the fixed Hamiltonian is diagonalized to yield energy eigenvalues for both occupied and unoccupied states, and a separation of them may even be performed after plotting the band diagram. In the latter case, however, whether a state is occupied now becomes crucial. The reason lies in that, only those occupied states contribute to the next V_{eff} term, and $n(\boldsymbol{r})$ must be calculated during each iteration step. The relation between V_{eff}, one-electron wavefunction $\psi_{i,\boldsymbol{k}}\left(\boldsymbol{r}\right)$ and $n(\boldsymbol{r})$ is illustrated in figure 3.

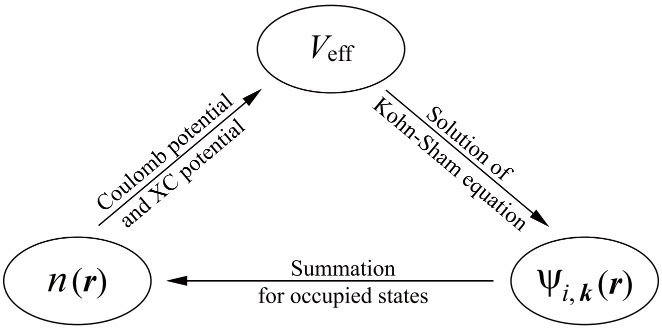

Figure 3. The basic self-consistent procedure using density functional theory.

Of course, DFT is not the only way for self-consistent electronic structure calculations. The pioneering works of self-consistent field calculations are those of Hartree [25] and Hartree–Fock [53]. Self-consistency has been well respected in the computational chemistry community. Indeed, quantum chemistry-based methods afford another route of self-consistent calculation, and are widely applied to molecules. These methods are based on many-electron wavefunctions (Slater determinants [54]), and the well-known Hartree–Fock self-consistent field method is the first cornerstone. In that case, the exchange effect between parallel-spin electrons is exactly considered, while the correlation effect is neglected. Löwdin defined the correlation energy as the energy difference between the true ground state and that of a Hartree–Fock ground state [55], which is always negative. The problem lies in that, the governing equation for Hartree–Fock involves the Coulomb interaction between electrons, which depends on the solution. Hence, the Hartree–Fock equation is not a fixed partial differential equation (for which the ground state must possess the lowest possible total energy), but in mixing certain excited states (also Slater determinants) linearly, the partial differential equation gets modified, allowing for even lower possible total energies. Hence, post-Hartree–Fock methods involve analysis of excited states that are originally believed to be less energetically favorable from a single determinant point of view. Each such state is named a configuration, and the so-called configuration interaction (CI) method can be regarded as an extension of the original variational method in Hartree–Fock: only single-determinant wavefunctions are used to minimize the total energy in Hartree–Fock, but in the CI method, one searches within a greater scope including multiple-determinants. However, accounting for all the configurations is extremely difficult, thus one may consider single-electron excitations, double-electron excitations, and so forth. Then comes the coupled cluster method that could be regarded as an even more advanced version of CI. These quantum chemistry methods have a clear background, and it is possible to achieve the desired accuracy by incorporating the proper number of configurations. The route is to improve the accuracy of correlation gradually, while keeping the exchange exact. In contrast, both exchange and correlation are intrinsically

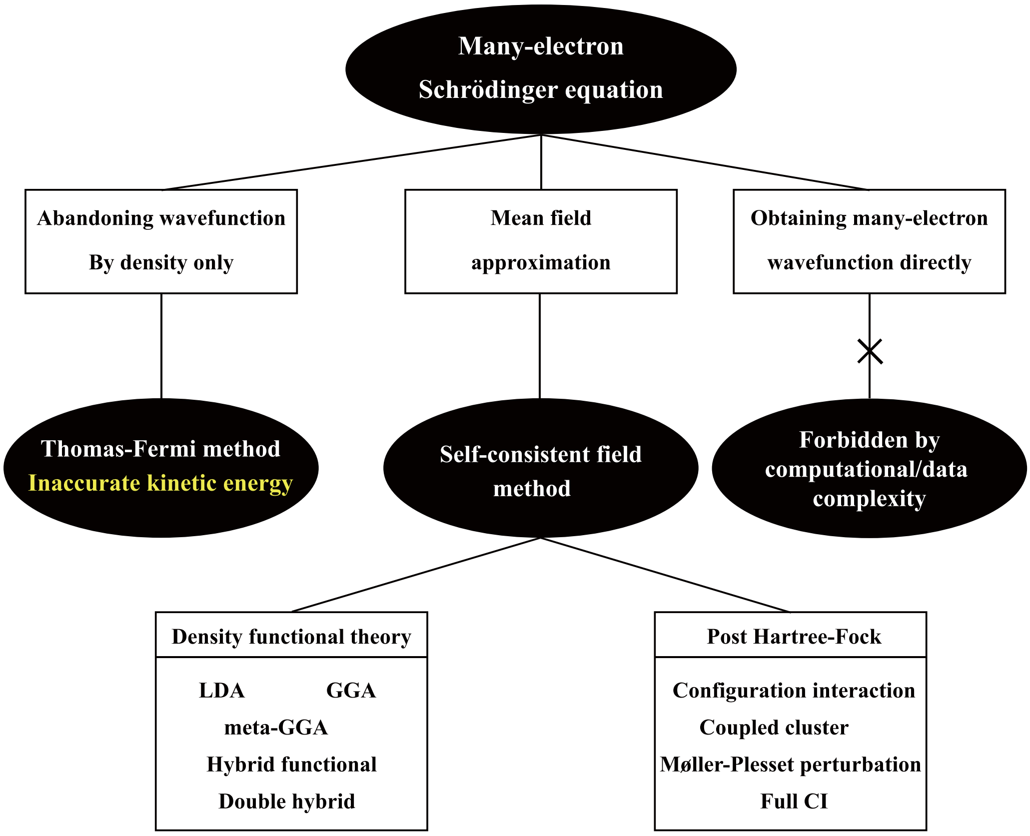

Figure 4. Various strategies in solving the many-electron Schrödinger equation: Thomas–Fermi method, density functional theory and post Hartree–Fock methods.

approximate in DFT. Although Hartree–Fock plus correlation is widely used in computational chemistry, there is still some difficulty in applying it to extended solids. The reason lies in that, the non-local exchange term in Hartree–Fock is much harder to handle in an extended solid compared with an isolated molecule. It inevitably causes a slow converging speed in solid-state calculations. This also partly answers why hybrid functionals [56–58] and even double hybrid functionals [59–63] are very common in molecular calculations, but computations at the LDA and generalized gradient approximation (GGA) [41, 42] levels are still popular in the solid-state community. On account of the great benefit in computational speed, DFT in general fits solid-state electronic structure calculations even though it suffers from inaccurate (but usually acceptable) exchange and correlation. A rough comparison of DFT and other methods in solving the many-electron Schrödinger equation is provided in figure 4.

Besides DFT and many-body wavefunction-based quantum chemistry methods, there is yet still an intermediate route. It is known that density matrices could give the same descriptions as wavefunctions. Density matrix functional theory (DMFT) [64] is a close relative to DFT with certain discrepancies. Unlike DFT, the kinetic energy in DMFT is exactly expressed in terms of the one-particle reduced density matrix, or its eigenvalues and eigenvectors (also named the natural orbitals and their occupation numbers). In its original conception by Gilbert [65], no Kohn-Sham-like eigenvalue equations were found due to the unexpected degeneracy for the partially occupied orbitals. In a recent work by Wang and Baerends [66], self-consistent eigenvalue equations have been established by the introduction of an information theoretical entropy to model the correlation energy. The eigenvalue equations are very close to the Hartree–Fock equations, while the occupation numbers follow the Fermi–Dirac distribution. Potential energy curves over the full range of nuclear distance in agreement with wavefunction methods or experiments were found [67, 68], not limited to the equilibrium distance. DMFT may open a new possibility for band structure calculation, though at the current stage the available codes are very rare.

2.2. *Why plane waves?*

Basis selection is the next key step in a band structure calculation. Plane waves are common choices for solid-state calculation, but they are by no means the only option. Atomic bases (local atomic orbitals such as 1s, 2s, 2p, 3s, …) are widely used in band structure calculations as well [48]. In quantum chemistry, many advanced local basis sets have been developed [69]. The special features regarding the plane wave basis are two folds.

- There is some formal similarity between the plane waves and the energy eigenstates in a solid, *i.e.* the Bloch waves. A Bloch wave has the mathematical form of equation (1-11), which is a plane wave $\exp(i\boldsymbol{k}\cdot\boldsymbol{r})$ times a periodic function $u(\boldsymbol{r})$. Hence, a Bloch state is regarded as an extended state that is typical for electrons in a solid. In contrast, the electronic states in a molecule are far from that of a plane wave.

- The plane wave set is intrinsically orthonormal, but atomic orbitals in a solid are in general not orthogonal. For any specific atom A in a solid, its 1s, 2s and 2p orbitals are orthogonal to each other, but the 1s orbital of atom A is not orthogonal to the 2p orbital of atom B. Atomic states could extend to a far distance, showing overlapping with each other. The Wannier functions [70, 71] are both local and orthogonal to each other, but one does not know the Wannier functions (the Fourier transform of the Bloch functions that are to be obtained) unless the electronic band structures are already derived. While atomic orbitals in a solid are not orthogonal, there are certain tricks to use them as the bases, at the cost of complexity in coding. The great advantage of using an atomic basis set resides in its efficiency in calculating very large supercells [72]. In this paper, however, we focus on plane wave bases because they are simple and best illustrate the fundamental methodology shown in section 1.2.

Notwithstanding the conceptual 'simplicity' of the plane waves, one must be aware of the actual meaning of the plane wave basis that is used in solid band structure calculations. It is not like the 1D $\exp(ikx)$ form with k varying continuously over all real numbers. Rather, band structure calculation for a solid involves a selected wavevector $\boldsymbol{k}$, and it is more proper to label the resulting Bloch wave using this $\boldsymbol{k}$ value and its band index (subscript i, but not to be confused with the imaginary unit i that only appears within the phase factor)

$$\psi_{i,\boldsymbol{k}}(\boldsymbol{r}) = u_{i,\boldsymbol{k}}(\boldsymbol{r})\,\mathrm{e}^{i\boldsymbol{k}\cdot\boldsymbol{r}}. \tag{2-2}$$

Since $\mathrm{e}^{i\boldsymbol{k}\cdot\boldsymbol{r}}$ already has the plane wave form, the exact term that needs to be expanded is $u_{i,\boldsymbol{k}}(\boldsymbol{r})$, which has the same periodicity as the crystal lattice. The knowledge from Fourier analysis informs us that, a periodic function only has its Fourier components at discrete k values. In other words, a periodic function, if continuous, can always be expanded as a Fourier series. Here $u_{i,\boldsymbol{k}}(\boldsymbol{r})$ has the lattice periodicity, thus its Fourier series only involves those components that are linear combinations of the reciprocal lattice vectors,

$$u_{i,\boldsymbol{k}}(\boldsymbol{r}) = \sum_{\boldsymbol{G}_m} c_{i,m}(\boldsymbol{k})\,\mathrm{e}^{i\boldsymbol{G}_m\cdot\boldsymbol{r}} \tag{2-3}$$

where $\boldsymbol{G}_m$ runs over all reciprocal lattice basis vectors and their linear combinations, and $c_{i,m}(\boldsymbol{k})$ is the expansion coefficient. Consequently, the Bloch state is expanded in a discrete plane wave set as

$$\psi_{i,\boldsymbol{k}}(\boldsymbol{r}) = \sum_{\boldsymbol{G}_m} c_{i,m}(\boldsymbol{k})\,\mathrm{e}^{i(\boldsymbol{k}+\boldsymbol{G}_m)\cdot\boldsymbol{r}}. \tag{2-4}$$

Therefore, the plane wave basis set involves wavevectors $\boldsymbol{k}+\boldsymbol{G}_1$, $\boldsymbol{k}+\boldsymbol{G}_2$, $\boldsymbol{k}+\boldsymbol{G}_3$, *etc*. Since there are infinitely many $\boldsymbol{G}_m$ terms, a proper truncation strategy must be specified. Note that the kinetic energy of the plane wave with wavevector $\boldsymbol{k}+\boldsymbol{G}_m$ is

$$\frac{\hbar^2|\boldsymbol{k}+\boldsymbol{G}_m|^2}{2m_e}$$

which is relevant to the modulus of $\boldsymbol{k}+\boldsymbol{G}_m$. The simplest criterion is thus setting up a cutoff (E_{cut}) for the kinetic energy of these plane waves. This involves placing the plane wave components in an ascending order of $|\boldsymbol{k}+\boldsymbol{G}_m|$, and all plane waves possessing kinetic energies greater than E_{cut} will be omitted. Hence, the plane wave basis set is extremely user-friendly because one simply sets a high E_{cut} for accuracy and a low E_{cut} for efficiency. A proper choice of E_{cut} is of primary importance for the calculation, which will be discussed in the next section.

2.3. *Why pseudopotentials?*

The concept of pseudopotential [73, 74] was initially proposed as an extension of the orthogonalized plane wave (OPW) method [75], and now proves extremely useful. The computational challenge arises when a standard plane wave basis set like that introduced in section 2.2 is used. The origin of this difficulty is that, plane waves are not appropriate to describe the behavior of electrons at those regions close to the nuclei. The nucleus potential is strong, and valence electrons have to be orthogonal to the core electrons in terms of their wavefunctions. Consequently, the electronic wavefunctions oscillate significantly near the nuclei, involving plane wave components with extremely high kinetic energies. There are in general two strategies to resolve this problem. One is to divide the space into core regions and an interstitial region, yielding the concept of APW, initially proposed by Slater [76]. The core regions are augmentation regions, where electrons are described using linear combination of atomic orbitals. The other is to modify the plane wave basis itself, without discriminating the core regions from the rest of the real space. The OPW method of Herring [75] is in this category. An OPW is smooth for those regions far from the cores, but oscillates severely in the core regions. This explains why electrons sometimes tend to be free in a solid, even though a solid involves very strong attractive nucleus potentials.

The necessity of pseudopotentials is documented as follows. While APWs and OPWs are feasible to use, they are still complicated basis sets. If one would like to expand the wavefunctions in terms of the original plane waves, one still faces the oversized basis set problem with a large E_{cut}. Yet, since the core electrons are usually unimportant for chemical bonding, in many applications there is no need to calculate them. The valence electrons, on the other hand, feel the screened nucleus potential that is much weaker. Hence, the pseudopotential becomes a natural approach, which is particularly useful if one selects the original plane wave basis set to expand the wavefunctions.

3. Pseudopotentials in the plane-wave methodology

The antecedent of modern pseudopotential is the OPW method, though a similar thought dates back to the early work of Hellmann [77]. The work by Phillips and Kleinman [73] is regarded as the beginning of modern pseudopotentials. The earliest pseudopotentials usually required the norm-conserving condition, leading to the concept of norm-conserving pseudopotential (NCPP) [78]. The work of Kleinman and Bylander (KB) [79] was a breakthrough since it not only reduces the computational cost in large cell calculations, but the proposal of writing the pseudopotential in terms of projectors has a much more profound influence. This further leads to the famous ultrasoft pseudopotential (USPP) of Vanderbilt [80], as well as the projector augmented-wave (PAW) method that was first proposed by Blöchl [81]. These two methods permit violating the norm-conserving condition to achieve faster speed, with the aid of compensation terms. However, this inevitably requires additional complexity in programming, and may face difficulty in certain applications such as density functional perturbation theory (DFPT) [82]. Hence, new investigations have been still carried out following the NCPP route, including the optimized norm-conserving Vanderbilt (ONCV) pseudopotential by Hamann [83].

There have been numerous reviews on the pseudopotential concept [84–88], and Schwerdtfeger has given an excellent review [74] on the pseudopotential approximation in the electronic structure theory. In this work, the focus is put on the mathematical representation of various pseudopotential theories. From now on, we shall turn to the atomic unit system, in which

$$m_e = e = \hbar = \frac{1}{4\pi\varepsilon_0} = 1. \tag{3-1}$$

Not only does it possess a simple mathematical form, but it is also the choice of various practical codes. Moreover, we shall keep the symbol E to represent quantities like the total energy of a solid, while for electronic energy eigenvalues, a new symbol ε will be used instead (actually already appearing in equation (1-12)). Although they share the same physical unit, their difference in meaning is obvious, and such distinction made in nomenclature is indeed desirable.

3.1. *From OPW to pseudopotential*

The OPW method was proposed by Herring in 1940 [75], initially for the calculation of valence electron states in metals [89]. When a number of metal atoms meet, they tend to gather for the formation of a solid. Consider, for instance, the formation of hexagonal close-packed metal Mg from Mg atoms. The inner core electrons, such as those from 1s and 2s shells, hardly experience any change in their states during this procedure. Hence, the tight binding method is already adequate to describe the 1s band formation in solid Mg. To be specific, a Bloch wavefunction with crystal wavevector $\boldsymbol{k}$ is established as

$$\Psi_{1s,\boldsymbol{k}}(\boldsymbol{r}) \approx \frac{1}{\sqrt{N_{\mathrm{Mg}}}} \sum_{\boldsymbol{R}_{\mathrm{Mg}}} \mathrm{e}^{i\boldsymbol{k}\cdot\boldsymbol{R}_{\mathrm{Mg}}} \Phi_{1s}(\boldsymbol{r}-\boldsymbol{R}_{\mathrm{Mg}}) \tag{3-2}$$

where Φ_{1s} represents the 1s atomic wavefunction for an isolated Mg atom, N_{Mg} is the total number of Mg atoms in the solid, and the sum is over all the Mg atom locations $\boldsymbol{R}_{\mathrm{Mg}}$. The mathematical form of equation (3-2) is equivalent to expanding a Bloch function in terms of Wannier functions, but we have used the known atomic 1s functions to replace the unknown Wannier functions. Therefore, this relation must be treated as an approximation. In a crystal, one tends to consider a primitive cell, which generates the entire lattice through translation vectors $\boldsymbol{T}_n$. Hence, equation (3-2) may be rewritten as

$$\Psi_{1s,\boldsymbol{k}}(\boldsymbol{r}) \approx \frac{1}{\sqrt{N_{\mathrm{Mg}}}} \sum_{\boldsymbol{T}_n} \mathrm{e}^{i\boldsymbol{k}\cdot\boldsymbol{T}_n} \sum_{\boldsymbol{\tau}_\alpha} \mathrm{e}^{i\boldsymbol{k}\cdot\boldsymbol{\tau}_\alpha} \Phi_{1s}(\boldsymbol{r}-\boldsymbol{\tau}_\alpha-\boldsymbol{T}_n) \tag{3-3}$$

where $\boldsymbol{\tau}_\alpha$ stands for the coordinates of Mg atoms inside a primitive cell. There are two Mg atoms within the primitive cell, with $\boldsymbol{\tau}_1$ and $\boldsymbol{\tau}_2$, respectively. The relation between $\boldsymbol{R}_{\mathrm{Mg}}$ and $\boldsymbol{\tau}_\alpha$ is simply

$$\boldsymbol{R}_{\mathrm{Mg}} = \boldsymbol{T}_n + \boldsymbol{\tau}_\alpha \Rightarrow \mathrm{e}^{i\boldsymbol{k}\cdot\boldsymbol{R}_{\mathrm{Mg}}} = \mathrm{e}^{i\boldsymbol{k}\cdot\boldsymbol{T}_n}\mathrm{e}^{i\boldsymbol{k}\cdot\boldsymbol{\tau}_\alpha}. \tag{3-4}$$

The expression (3-3) is not apparently in a modulated plane wave form, but it is straightforward to show that

$$\begin{aligned}
&\Psi_{1s,\boldsymbol{k}}(\boldsymbol{r}+\boldsymbol{T}_m) \\
&= \frac{1}{\sqrt{N_{\mathrm{Mg}}}} \sum_{\boldsymbol{T}_n} \mathrm{e}^{i\boldsymbol{k}\cdot\boldsymbol{T}_n} \sum_{\boldsymbol{\tau}_\alpha} \mathrm{e}^{i\boldsymbol{k}\cdot\boldsymbol{\tau}_\alpha} \Phi_{1s}[\boldsymbol{r}-\boldsymbol{\tau}_\alpha-(\boldsymbol{T}_n-\boldsymbol{T}_m)] \\
&= \mathrm{e}^{i\boldsymbol{k}\cdot\boldsymbol{T}_m} \Bigg\{ \frac{1}{\sqrt{N_{\mathrm{Mg}}}} \sum_{\boldsymbol{T}_n} \mathrm{e}^{i\boldsymbol{k}\cdot(\boldsymbol{T}_n-\boldsymbol{T}_m)} \sum_{\boldsymbol{\tau}_\alpha} \mathrm{e}^{i\boldsymbol{k}\cdot\boldsymbol{\tau}_\alpha} \Phi_{1s}[\boldsymbol{r}-\boldsymbol{\tau}_\alpha \\
&\quad -(\boldsymbol{T}_n-\boldsymbol{T}_m)] \Bigg\} \\
&= \mathrm{e}^{i\boldsymbol{k}\cdot\boldsymbol{T}_m} \left[\frac{1}{\sqrt{N_{\mathrm{Mg}}}} \sum_{\boldsymbol{T}_j} \mathrm{e}^{i\boldsymbol{k}\cdot\boldsymbol{T}_j} \sum_{\boldsymbol{\tau}_\alpha} \mathrm{e}^{i\boldsymbol{k}\cdot\boldsymbol{\tau}_\alpha} \Phi_{1s}(\boldsymbol{r}-\boldsymbol{\tau}_\alpha-\boldsymbol{T}_j) \right] \\
&= \mathrm{e}^{i\boldsymbol{k}\cdot\boldsymbol{T}_m} \Psi_{1s,\boldsymbol{k}}(\boldsymbol{r})
\end{aligned} \tag{3-5}$$

where $\boldsymbol{T}_j \equiv \boldsymbol{T}_n - \boldsymbol{T}_m$. It turns out that $\Psi_{1s,\boldsymbol{k}}$ satisfies the Bloch theorem, as expected. Since two Mg atoms constitute a primitive cell,

$$\begin{aligned}
\sum_{\boldsymbol{\tau}_\alpha} \mathrm{e}^{i\boldsymbol{k}\cdot\boldsymbol{\tau}_\alpha} \Phi_{1s}(\boldsymbol{r}-\boldsymbol{\tau}_\alpha-\boldsymbol{T}_j) &= \mathrm{e}^{i\boldsymbol{k}\cdot\boldsymbol{\tau}_1} \Phi_{1s}(\boldsymbol{r}-\boldsymbol{\tau}_1-\boldsymbol{T}_j) \\
&\quad + \mathrm{e}^{i\boldsymbol{k}\cdot\boldsymbol{\tau}_2} \Phi_{1s}(\boldsymbol{r}-\boldsymbol{\tau}_2-\boldsymbol{T}_j)
\end{aligned} \tag{3-6}$$

but this is not like considering the neighboring interactions as in a typical tight binding approach. The sum over the two Mg atoms is merely a part of summation over all Mg atoms in the solid, but no overlapping between $\Phi_{1s}(\boldsymbol{r}-\boldsymbol{\tau}_1-\boldsymbol{T}_j)$ and $\Phi_{1s}(\boldsymbol{r}-\boldsymbol{\tau}_2-\boldsymbol{T}_j)$ has been taken into account at all. Such treatment is only reasonable for deep-lying core states. For valence electrons, at least the overlapping of atomic wavefunctions between nearest neighbors has to be considered. In this sense, an even simplified 'tight binding but no bonding' approach has been used in our construction of $\Psi_{1s,\boldsymbol{k}}$ above. By 'tight binding' we mean each 1s electron is approximately regarded as confined to a local region surrounding the central Mg nucleus. By 'no bonding' we mean any overlapping integral between $\Phi_{1s}(\boldsymbol{r}-\boldsymbol{R}_{\mathrm{Mg}})$ and $\Phi_{1s}\left(\boldsymbol{r}-\boldsymbol{R}'_{\mathrm{Mg}}\right)$ is treated as zero, given that $\boldsymbol{R}'_{\mathrm{Mg}} \neq \boldsymbol{R}_{\mathrm{Mg}}$. Indeed, chemical bonding is the task for 3s electrons, not 1s electrons. The procedure described above is nothing but a necessary step towards a Bloch wavefunction $\Psi_{1s,\boldsymbol{k}}$ that is an eigenstate of the effective one-electron Hamiltonian for the solid, rather than for an isolated atom.

After handling the deep core states, the focus is now placed on electronic states with higher energies. Provided that one would like to calculate the very high-lying band energies of solid Mg, which are higher than the Fermi level by at least 5 eV, then tight binding is obviously not a proper solution. Nevertheless, these electronic states are quite close to plane waves, and their computational cost would not be very high using the standard plane wave expansion method. The true difficulty lies in handling the electronic states of the valence electrons, *i.e.* 3s electrons in this example. These electrons are not like atomic states for the regions apart from the cores, but they also contain high frequency components in the reciprocal space and a great cost must be paid in plane wave expansion. The OPW was therefore designed for expanding the states of these valence electrons, favoring a smaller basis set at the cost of more complicated basis functions. It has to be emphasized that an OPW is derived by subtracting the projections on particular Bloch states ($\Psi_{j,\boldsymbol{k}}$) that consist of the core atomic orbitals (Φ_j). To better illustrate the difference, we write explicitly

$$\Psi_{j,\boldsymbol{k}}(\boldsymbol{r}) = \frac{1}{\sqrt{N}} \sum_{\boldsymbol{R}} \mathrm{e}^{i\boldsymbol{k}\cdot\boldsymbol{R}} \Phi_j(\boldsymbol{r}-\boldsymbol{R}). \tag{3-7}$$

After the projections onto these states are deducted, we obtain the resulting OPW function

$$\Lambda_{\boldsymbol{k}+\boldsymbol{G}}(\boldsymbol{r}) = \phi_{\boldsymbol{k}+\boldsymbol{G}}(\boldsymbol{r}) - \sum_j \langle \Psi_{j,\boldsymbol{k}} | \phi_{\boldsymbol{k}+\boldsymbol{G}} \rangle \Psi_{j,\boldsymbol{k}}(\boldsymbol{r}) \tag{3-8}$$

where j runs for all core orbitals of all the atoms in a primitive cell, and

$$\phi_{\boldsymbol{k}+\boldsymbol{G}}(\boldsymbol{r}) = \frac{1}{\sqrt{\Omega_{\mathrm{cell}}}} \mathrm{e}^{i(\boldsymbol{k}+\boldsymbol{G})\cdot\boldsymbol{r}} \tag{3-9}$$

is an ordinary plane wave, where Ω_{cell} is the volume of a primitive cell. Here $\boldsymbol{G}$ represents a reciprocal lattice vector

$$\boldsymbol{G} = \boldsymbol{G}_m. \tag{3-10}$$

When there is no summation operation over $\boldsymbol{G}_m$, we may also temporarily hide the subscript m for brevity and convenience. The following orthogonal condition is respected

$$\begin{aligned}
&\langle \Lambda_{\boldsymbol{k}+\boldsymbol{G}} | \Psi_{j',\boldsymbol{k}} \rangle \\
&\quad = \langle \phi_{\boldsymbol{k}+\boldsymbol{G}} | \Psi_{j',\boldsymbol{k}} \rangle - \sum_j \left(\langle \Psi_{j,\boldsymbol{k}} | \phi_{\boldsymbol{k}+\boldsymbol{G}} \rangle\right)^* \langle \Psi_{j,\boldsymbol{k}} | \Psi_{j',\boldsymbol{k}} \rangle \\
&\quad = \langle \phi_{\boldsymbol{k}+\boldsymbol{G}} | \Psi_{j',\boldsymbol{k}} \rangle - \sum_j \langle \phi_{\boldsymbol{k}+\boldsymbol{G}} | \Psi_{j,\boldsymbol{k}} \rangle \delta_{j,j'} \\
&\quad = \langle \phi_{\boldsymbol{k}+\boldsymbol{G}} | \Psi_{j',\boldsymbol{k}} \rangle - \langle \phi_{\boldsymbol{k}+\boldsymbol{G}} | \Psi_{j',\boldsymbol{k}} \rangle \\
&\quad = 0.
\end{aligned} \tag{3-11}$$

In equation (3-8), $\langle \Psi_{j,\boldsymbol{k}} | \phi_{\boldsymbol{k}+\boldsymbol{G}} \rangle$ is the inner product of $\phi_{\boldsymbol{k}+\boldsymbol{G}}$, the plane wave, with respect to the core-orbital-constructed Bloch wavefunction $\Psi_{j,\boldsymbol{k}}$. After timed by $\Psi_{j,\boldsymbol{k}}$, it becomes the projection of $\phi_{\boldsymbol{k}+\boldsymbol{G}}$ onto $\Psi_{j,\boldsymbol{k}}$. The as-obtained OPW $\Lambda_{\boldsymbol{k}+\boldsymbol{G}}(\boldsymbol{r})$ has the desired property since it oscillates greatly near the nuclei but behaves still like a plane wave apart from the cores. Nevertheless, it is straightforward to verify that

$$\begin{aligned}
&\langle \Lambda_{\boldsymbol{k}+\boldsymbol{G}} | \Lambda_{\boldsymbol{k}+\boldsymbol{G}} \rangle \\
&\quad = 1 - 2\sum_j |\langle \Psi_{j,\boldsymbol{k}} | \phi_{\boldsymbol{k}+\boldsymbol{G}} \rangle|^2 \\
&\qquad + \sum_{j,j'} \langle \Psi_{j,\boldsymbol{k}} | \phi_{\boldsymbol{k}+\boldsymbol{G}} \rangle^* \langle \Psi_{j',\boldsymbol{k}} | \phi_{\boldsymbol{k}+\boldsymbol{G}} \rangle \langle \Psi_{j,\boldsymbol{k}} | \Psi_{j',\boldsymbol{k}} \rangle \\
&\quad = 1 - \sum_j |\langle \Psi_{j,\boldsymbol{k}} | \phi_{\boldsymbol{k}+\boldsymbol{G}} \rangle|^2 < 1.
\end{aligned} \tag{3-12}$$

Hence, $\Lambda_{\boldsymbol{k}+\boldsymbol{G}}$ is not normalized, and one can show that $\Lambda_{\boldsymbol{k}+\boldsymbol{G}}$ and $\Lambda_{\boldsymbol{k}+\boldsymbol{G}'}$ are not orthogonal given that $\boldsymbol{G} \neq \boldsymbol{G}'$.

Many types of electronic wavefunctions are encountered in this work. To avoid any confusion, the meaning of each wavefunction symbol is documented in table 1. Particularly, ψ will be reserved for those valence electrons in a solid, while the symbol Ψ emphasizes a core state. While the OPW wavefunctions $\Lambda_{\boldsymbol{k}+\boldsymbol{G}_m}$ are not orthonormal, they remain linearly independent. Therefore, the valence state electronic wavefunction $\psi_{n,\boldsymbol{k}}$ may still be expanded as a linear combination of $\Lambda_{\boldsymbol{k}+\boldsymbol{G}_m}$

$$\begin{aligned}
\psi_{n,\boldsymbol{k}}(\boldsymbol{r}) &= \sum_{\boldsymbol{G}_m} c_{\boldsymbol{k}}(\boldsymbol{G}_m) \Lambda_{\boldsymbol{k}+\boldsymbol{G}_m}(\boldsymbol{r}) \\
&= \sum_{\boldsymbol{G}_m} c_{\boldsymbol{k}}(\boldsymbol{G}_m) \phi_{\boldsymbol{k}+\boldsymbol{G}_m}(\boldsymbol{r}) \\
&\quad - \sum_{\boldsymbol{G}_m} \sum_j c_{\boldsymbol{k}}(\boldsymbol{G}_m) \langle \Psi_{j,\boldsymbol{k}} | \phi_{\boldsymbol{k}+\boldsymbol{G}_m} \rangle \Psi_{j,\boldsymbol{k}}(\boldsymbol{r})
\end{aligned} \tag{3-13}$$

where equation (3-8) has been used to expand $\Lambda_{\boldsymbol{k}+\boldsymbol{G}}$. One may further introduce (the tilde symbol denotes a 'smooth' version)

$$\tilde{\psi}_{n,\boldsymbol{k}}(r) \equiv \sum_{\boldsymbol{G}_m} c_{\boldsymbol{k}}(\boldsymbol{G}_m) \phi_{\boldsymbol{k}+\boldsymbol{G}_m}(\boldsymbol{r}) \tag{3-14}$$

to simplify the expression, which yields

$$\psi_{n,\boldsymbol{k}}(\boldsymbol{r}) = \tilde{\psi}_{n,\boldsymbol{k}}(\boldsymbol{r}) - \sum_j C_{j,\boldsymbol{k}} \Psi_{j,\boldsymbol{k}}(\boldsymbol{r}) \tag{3-15}$$

Table 1. Nomenclature regarding electronic wavefunctions in this work. Three types of wavefunctions are unambiguously discriminated: an atomic one is expressed within a spherical coordinate system, a periodic one has the exact lattice periodicity, and a Bloch wavefunction is periodic only for the special case of Γ point.

Symbol	Variables	Type	Meaning	Expression
ϕ	$\boldsymbol{r}$	Periodic	Ordinary plane wave	$\phi_{\boldsymbol{k}}(\boldsymbol{r}) = \frac{1}{\sqrt{\Omega}}\mathrm{e}^{i\boldsymbol{k}\cdot\boldsymbol{r}}$
R	r	Atomic	Radial wavefunction for an isolated atom	
Y	$\theta,\ \varphi$	Atomic	Spherical harmonics	
Φ	r,θ,φ	Atomic	Energy eigenfunction for an isolated atom	$\Phi_{lm}(r,\theta,\varphi) = R_l(r)\,Y_{lm}(\theta,\varphi)$
Ψ	$\boldsymbol{r}$	Bloch	Energy eigenfunction for a core-electron state in a solid	$\Psi_{j,\boldsymbol{k}}(\boldsymbol{r}) = \frac{1}{\sqrt{N}}\sum_{\boldsymbol{R}}\mathrm{e}^{i\boldsymbol{k}\cdot\boldsymbol{R}}\Phi_j(\boldsymbol{r}-\boldsymbol{R})$
ψ	$\boldsymbol{r}$	Bloch	Energy eigenfunction for a valence-electron state in a solid	
$\tilde{\psi}$	$\boldsymbol{r}$	Bloch	Pseudo-wavefunction	
Λ	$\boldsymbol{r}$	Bloch	OPW basis wavefunction	$\Lambda_{\boldsymbol{k}+\boldsymbol{G}}(\boldsymbol{r})$ $= \phi_{\boldsymbol{k}+\boldsymbol{G}}(\boldsymbol{r})$ $-\sum_j \langle \Psi_{j,\boldsymbol{k}} \vert \phi_{\boldsymbol{k}+\boldsymbol{G}}\rangle\, \Psi_{j,\boldsymbol{k}}(\boldsymbol{r})$

where

$$C_{j,\boldsymbol{k}} \equiv \sum_{\boldsymbol{G}_m} c_{\boldsymbol{k}}(\boldsymbol{G}_m)\left\langle \Psi_{j,\boldsymbol{k}} \middle| \phi_{\boldsymbol{k}+\boldsymbol{G}_m}\right\rangle \tag{3-16}$$

is defined as a new coefficient covering all $\boldsymbol{G}_m$ values. One now requires that the wavefunction (3-15) should satisfy the one-electron eigenvalue equation (stationary Schrödinger equation) for the solid

$$\widehat{H}_{\text{eff}}\psi_{n,\boldsymbol{k}} = \varepsilon_{n,\boldsymbol{k}}\psi_{n,\boldsymbol{k}}. \tag{3-17}$$

Note that the Hamiltonian for the one-electronic state acts like

$$\widehat{H}_{\text{eff}}\psi_{n,\boldsymbol{k}} = \widehat{H}_{\text{eff}}\tilde{\psi}_{n,\boldsymbol{k}} - \sum_j C_{j,\boldsymbol{k}}\varepsilon_{j,\boldsymbol{k}}\Psi_{j,\boldsymbol{k}} \tag{3-18}$$

since $\Psi_{j,\boldsymbol{k}}$ is the known core-state Bloch wavefunction and $\varepsilon_{j,\boldsymbol{k}}$ is the corresponding energy eigenvalue. Hence, the sum over j is only carried out for those core Bloch states. Multiplying both sides of equation (3-15) by $\varepsilon_{n,\boldsymbol{k}}$ gives

$$\varepsilon_{n,\boldsymbol{k}}\psi_{n,\boldsymbol{k}} = \varepsilon_{n,\boldsymbol{k}}\tilde{\psi}_{n,\boldsymbol{k}} - \sum_j C_{j,\boldsymbol{k}}\varepsilon_{n,\boldsymbol{k}}\Psi_{j,\boldsymbol{k}} \tag{3-19}$$

which, when combined with equation (3-15) and the Schrödinger equation (3-17), leads to

$$\begin{aligned}\varepsilon_{n,\boldsymbol{k}}\psi_{n,\boldsymbol{k}} &= \widehat{H}_{\text{eff}}\psi_{n,\boldsymbol{k}} = \widehat{H}_{\text{eff}}\tilde{\psi}_{n,\boldsymbol{k}} - \sum_j \widehat{H}_{\text{eff}}\left(C_{j,\boldsymbol{k}}\Psi_{j,\boldsymbol{k}}\right)\\ &= \widehat{H}_{\text{eff}}\tilde{\psi}_{n,\boldsymbol{k}} - \sum_j \varepsilon_{j,\boldsymbol{k}}C_{j,\boldsymbol{k}}\Psi_{j,\boldsymbol{k}}.\end{aligned} \tag{3-20}$$

This relation may be utilized to substitute for the $\varepsilon_{n,\boldsymbol{k}}\psi_{n,\boldsymbol{k}}$ term in equation (3-19), yielding

$$\begin{aligned}&\varepsilon_{n,\boldsymbol{k}}\tilde{\psi}_{n,\boldsymbol{k}}\\ &\quad= \varepsilon_{n,\boldsymbol{k}}\psi_{n,\boldsymbol{k}} + \sum_j \varepsilon_{n,\boldsymbol{k}}C_{j,\boldsymbol{k}}\Psi_{j,\boldsymbol{k}}\\ &\quad= \widehat{H}_{\text{eff}}\tilde{\psi}_{n,\boldsymbol{k}} + \sum_j \left(\varepsilon_{n,\boldsymbol{k}} - \varepsilon_{j,\boldsymbol{k}}\right)C_{j,\boldsymbol{k}}\Psi_{j,\boldsymbol{k}}\\ &\quad= \widehat{H}_{\text{eff}}\tilde{\psi}_{n,\boldsymbol{k}} + \sum_j \left(\varepsilon_{n,\boldsymbol{k}} - \varepsilon_{j,\boldsymbol{k}}\right)\left|\Psi_{j,\boldsymbol{k}}\right\rangle\left\langle\Psi_{j,\boldsymbol{k}}\right|\sum_{\boldsymbol{G}_m} c_{\boldsymbol{k}}(\boldsymbol{G}_m)\,\phi_{\boldsymbol{k}+\boldsymbol{G}_m}\\ &\quad= \widehat{H}_{\text{eff}}\tilde{\psi}_{n,\boldsymbol{k}} + \sum_j \left(\varepsilon_{n,\boldsymbol{k}} - \varepsilon_{j,\boldsymbol{k}}\right)\left|\Psi_{j,\boldsymbol{k}}\right\rangle\left\langle\Psi_{j,\boldsymbol{k}}\middle|\tilde{\psi}_{n,\boldsymbol{k}}\right.\end{aligned} \tag{3-21}$$

where we have used the definition (3-16) to expand $C_{j,\boldsymbol{k}}$, and definition (3-14) to recover $\tilde{\psi}_{n,\boldsymbol{k}}$. Now $\widehat{H}_{\text{eff}}$ consists of a kinetic energy part and a potential energy part

$$\widehat{H}_{\text{eff}} = \widehat{T} + \widehat{V} \tag{3-22}$$

and the Schrödinger equation is rewritten as

$$\begin{aligned}\varepsilon_{n,\boldsymbol{k}}\tilde{\psi}_{n,\boldsymbol{k}} &= \widehat{T}\tilde{\psi}_{n,\boldsymbol{k}} + \widehat{V}\tilde{\psi}_{n,\boldsymbol{k}} + \sum_j \left(\varepsilon_{n,\boldsymbol{k}} - \varepsilon_{j,\boldsymbol{k}}\right)\left|\Psi_{j,\boldsymbol{k}}\right\rangle\left\langle\Psi_{j,\boldsymbol{k}}\middle|\tilde{\psi}_{n,\boldsymbol{k}}\right.\\ &= \widehat{T}\tilde{\psi}_{n,\boldsymbol{k}} + \widehat{V}_{\text{PKA}}\tilde{\psi}_{n,\boldsymbol{k}}\end{aligned} \tag{3-23}$$

where

$$\widehat{V}_{\text{PKA}} = \widehat{V} + \sum_j \left(\varepsilon_{n,\boldsymbol{k}} - \varepsilon_{j,\boldsymbol{k}}\right)\left|\Psi_{j,\boldsymbol{k}}\right\rangle\left\langle\Psi_{j,\boldsymbol{k}}\right| \tag{3-24}$$

is defined as the effective potential operator. Here PKA represents Phillips, Kleinman as well as Antončík who carried out the relevant pioneering works. The work of Phillips and Kleinman [73] was published in 1959, and that of Antončík [90] was published in the same year. Through solving equation (3-23) one obtains the energy eigenvalue $\varepsilon_{n,\boldsymbol{k}}$ as well as $\tilde{\psi}_{n,\boldsymbol{k}}$, but it has to be emphasized that the true electronic wavefunction is $\tilde{\psi}_{n,\boldsymbol{k}}$ subtracting $\sum_j C_{j,\boldsymbol{k}}\Psi_{j,\boldsymbol{k}}$. According to equation (3-24), the impact of core electrons is equivalent to a screening term. Consider

$$\begin{aligned}&\left\langle\tilde{\psi}_{n,\boldsymbol{k}}\middle|\widehat{V}_{\text{PKA}}\middle|\tilde{\psi}_{n,\boldsymbol{k}}\right\rangle\\ &\quad= \left\langle\tilde{\psi}_{n,\boldsymbol{k}}\middle|\widehat{V}\middle|\tilde{\psi}_{n,\boldsymbol{k}}\right\rangle + \sum_j \left(\varepsilon_{n,\boldsymbol{k}} - \varepsilon_{j,\boldsymbol{k}}\right)\left\langle\tilde{\psi}_{n,\boldsymbol{k}}\middle|\Psi_{j,\boldsymbol{k}}\right\rangle\left\langle\Psi_{j,\boldsymbol{k}}\middle|\tilde{\psi}_{n,\boldsymbol{k}}\right\rangle\\ &\quad= \left\langle\tilde{\psi}_{n,\boldsymbol{k}}\middle|\widehat{V}\middle|\tilde{\psi}_{n,\boldsymbol{k}}\right\rangle + \sum_j \left(\varepsilon_{n,\boldsymbol{k}} - \varepsilon_{j,\boldsymbol{k}}\right)\left|\left\langle\tilde{\psi}_{n,\boldsymbol{k}}\middle|\Psi_{j,\boldsymbol{k}}\right\rangle\right|^2.\end{aligned} \tag{3-25}$$

Since $\varepsilon_{n,\boldsymbol{k}} - \varepsilon_{j,\boldsymbol{k}}$ is positive (the core electrons must enjoy lower energies), the negative effective potential $\widehat{V}_{\text{PKA}}$ is weaker than that from bare nuclei, yielding more smooth wavefunctions $\tilde{\psi}_{n,\boldsymbol{k}}$. Of course, the effective potential is more complicated than the bare nucleus potential, but working with smooth wavefunctions could greatly reduce the computational cost.

The work of PKA indicates that the valence electrons actually experience much weaker effective potential than the bare nucleus potential, and a smooth pseudo-wavefunction $\tilde{\psi}_{n,\boldsymbol{k}}$ may be used instead of the true wavefunction that typically oscillates significantly. In this case, the effective potential becomes a pseudopotential, which also has spherical symmetry. Nevertheless, in separating the variables under a spherical coordinate system, the radial equation becomes l-dependent where l is the quantum number of orbital momentum in the angle-part spherical harmonics $Y_{lm}(\theta,\varphi)$. This implies that a single radial pseudopotential $V^{\mathrm{ps}}(r)$ cannot be arrived at for all angular momentum components. Instead, one should write the pseudopotential operator as

$$\widehat{V}^{\mathrm{ps}}(r)=\sum_{l,m}|Y_{lm}\rangle V_l^{\mathrm{ps}}(r)\langle Y_{lm}| \tag{3-26}$$

where $V_0^{\mathrm{ps}}(r)$, $V_1^{\mathrm{ps}}(r)$, $V_2^{\mathrm{ps}}(r)$ …are prepared for the s, p, d… components, respectively. And $|Y_{lm}\rangle\cdots\langle Y_{lm}|$ means a projection onto the spherical harmonics, which are written under position representation as

$$Y_{lm}(\theta,\varphi)=P_l^m(\cos(\theta))\,\mathrm{e}^{im\varphi} \tag{3-27}$$

where P_l^m is associated Legendre polynomial. Hence, for a specific l value, the radial part of the pseudopotential merely replies on r, while the angle part depends not only on (θ, φ), which come from $|Y_{lm}\rangle$, but also on (θ',φ') in $\langle Y_{lm}|$. In this sense, the pseudopotential operator (3-26) is called 'semi-local', for it is local in terms of the radial variable but non-local in terms of the angular variables. Its application upon an arbitrary wavefunction $\psi(r,\theta,\varphi)$ becomes

$$\widehat{V}^{\mathrm{ps}}\psi(r,\theta,\varphi)=\sum_{l,m}Y_{lm}(\theta',\varphi')V_l^{\mathrm{ps}}(r)\times\int\sin\theta\,\mathrm{d}\theta\int\mathrm{d}\varphi\,Y_{lm}^{*}(\theta,\varphi)\,\psi(r,\theta,\varphi). \tag{3-28}$$

Note that $\widehat{V}^{\mathrm{ps}}$ here is non-local in angular coordinates, thus θ and θ' both appear in the expression. Yet, it remains radially local, such that only one radial variable r appears in the expression.

3.2. NCPP

The pseudopotential method circumvents some difficulties that are specific to the OPW method. Note that the set of OPWs is not orthonormal, thus a generalized eigenvalue problem must be solved

$$\left(\widehat{H}^{\mathrm{OPW}}-\varepsilon_n\hat{S}\right)\psi_n^{\mathrm{OPW}}=0 \tag{3-29}$$

provided that the desired valence electron state is expanded in terms of OPWs. Here $\hat{S}$ is named the overlap operator (or overlap matrix $\boldsymbol{S}$ since a discrete basis set has been selected). In the NCPP method, however, the pseudo-wavefunction is sufficiently smooth to be expanded in terms of ordinary plane waves, which are orthonormal, rendering $\boldsymbol{S}=\boldsymbol{I}$ (identity matrix). Besides, the benefit of NCPP lies in that the pseudo-wavefunctions are norm-conserving (identical to the all-electron wavefunctions beyond a core radius R_{c}), better recovering the all-electron states with relatively good transferability among various chemical environments. Since $\boldsymbol{S}=\boldsymbol{I}$ in the NCPP method, one obtains a rather simple equation for eigenvalues and eigenstates

$$\left(\widehat{H}^{\mathrm{NCPP}}-\varepsilon_n\right)\psi_n^{\mathrm{NCPP}}=0. \tag{3-30}$$

Of course, to judge whether a pseudopotential is norm-conserving, one needs the all-electron wavefunctions for reference. The famous norm-conserving condition was proposed by Hamann, Schlüter and Chiang [78]. Provided that the core radius is R_{c}, then the following conditions should be respected to yield an NCPP, noting that l is the pre-specified angular quantum number.

(a) The energy eigenvalue of the pseudo-wavefunction ($\tilde{\varepsilon}_l$) equals that of the all-electron wavefunction, *i.e.* $\tilde{\varepsilon}_l=\varepsilon_l$;
(b) For the $r>R_{\mathrm{c}}$ region, the pseudo-wavefunction becomes identical to the all-electron wavefunction, *i.e.* $\Phi_l^{\mathrm{ps}}=\Phi_l^{\mathrm{ae}}$;
(c) At $r=R_{\mathrm{c}}$, the logarithmic derivatives of the pseudo-wavefunction and the all-electron wavefunction should match, $\frac{\mathrm{d}}{\mathrm{d}r}\ln\Phi_l^{\mathrm{ps}}|_{r=R_{\mathrm{c}}}=\frac{\mathrm{d}}{\mathrm{d}r}\ln\Phi_l^{\mathrm{ae}}|_{r=R_{\mathrm{c}}}$;
(d) For the core region ($r\leqslant R_{\mathrm{c}}$), the integrated charges of the pseudo-wavefunction and the all-electron wavefunction are identical, *i.e.* $Q_l=\int_0^{R_{\mathrm{c}}}r^2\left|R_l^{\mathrm{ps}}\right|^2\mathrm{d}r=\int_0^{R_{\mathrm{c}}}r^2\left|R_l^{\mathrm{ae}}\right|^2\mathrm{d}r$, which is sometimes named the (special) norm-conserving condition;
(e) Let $D_l(\varepsilon,r)=r\frac{\mathrm{d}}{\mathrm{d}r}\ln\Phi_l(\varepsilon,r)$, which depends on the energy eigenvalue ε. $D_l^{\mathrm{ps}}(\varepsilon,r)$ and $D_l^{\mathrm{ae}}(\varepsilon,r)$ characterize that of the pseudo-wavefunction and the all-electron wavefunction, respectively. It is required that at $r=R_{\mathrm{c}}$, $\frac{\partial D_l^{\mathrm{ps}}}{\partial\varepsilon}=\frac{\partial D_l^{\mathrm{ae}}}{\partial\varepsilon}$.

Norm-conservation thus maintains the total charge inside R_{c}, and the potential beyond R_{c} is consistent with the all-electron case for an NCPP, according to the Gauss's law. Moreover, the pseudo-wavefunction should be identical to the all-electron wavefunction for $r\geqslant R_{\mathrm{c}}$.

Our key concern is how to generate an NCPP. Since a pseudopotential is derived from an atom (or sometimes its ion) that shows spherical symmetry, a separation of variables method works for the pseudo-wavefunction $\Phi_{lm}^{\mathrm{ps}}(\boldsymbol{r})=R_l^{\mathrm{ps}}(r)\,Y_{lm}(\theta,\varphi)$. As usual, the radial equation now becomes l-dependent

$$\left[-\frac{1}{2}\frac{\mathrm{d}^2}{\mathrm{d}r^2}+\frac{l(l+1)}{2r^2}+V_l^{\mathrm{ps,scr}}(r)\right]rR_l^{\mathrm{ps}}(r)=\varepsilon_l rR_l^{\mathrm{ps}}(r) \tag{3-31}$$

where the superscript 'scr' means the potential V_l^{ps} here is a screened version by other electrons, thus it does not represent the bare ionic potential. In contrast to solving a usual radial equation as in the hydrogen atom case, here one cares about obtaining $V_l^{\mathrm{ps,scr}}$ based on a well-designed radial pseudowavefunction $R_l^{\mathrm{ps}}(r)$. Of course, $R_l^{\mathrm{ps}}(r)$ has to be chosen as smooth as possible, without any nodes along r. Given a definite $R_l^{\mathrm{ps}}(r)$ and the corresponding energy eigenvalue ε_l (readily available from a previous all-electron calculation), the radial equation can be inversely solved to yield

$$V_l^{\mathrm{ps,scr}}(r) = \varepsilon_l - \frac{l(l+1)}{2r^2} + \frac{1}{2rR_l^{\mathrm{ps}}(r)}\frac{\mathrm{d}^2}{\mathrm{d}r^2}\left[rR_l^{\mathrm{ps}}(r)\right]. \quad (3\text{-}32)$$

Hence, the steps to generate an NCPP involve: (i) carrying out an all-electron calculation; (ii) designing the pseudowavefunction based on the all-electron wavefunction; (iii) generating the pseudopotential upon inversely solving the radial equation. Yet, there is still a final unscreening step that is indispensable. Indeed, in obtaining $V_l^{\mathrm{ps,scr}}$ one has to work in a multi-electron environment, thus $V_l^{\mathrm{ps,scr}}$ inevitably includes the Hartree potential as well as the exchange-correlation potential. These potentials highly depend on the chemical environment, and cannot be transferred to other problems. The aim of the unscreening step is to obtain the bare ionic potential that is much more transferrable. To this end one has to calculate the valence charge density n_v, which satisfies

$$\begin{aligned} n_v(r)\,\mathrm{d}r &= \sum_{l,m}\int_{\theta=0}^{\pi}\int_{\varphi=0}^{2\pi}\left|\Phi_{lm}^{\mathrm{ps}}\right|^2 r^2\sin\theta\mathrm{d}r\mathrm{d}\theta\mathrm{d}\varphi \\ &= \sum_{l,m}\left|R_l^{\mathrm{ps}}(r)\right|^2 r^2\int_{\theta=0}^{\pi}\int_{\varphi=0}^{2\pi}\left|Y_{lm}(\theta,\varphi)\right|^2\sin\theta\mathrm{d}r\mathrm{d}\theta\mathrm{d}\varphi \\ &= \sum_{l,m}\left|rR_l^{\mathrm{ps}}(r)\right|^2\mathrm{d}r \end{aligned} \quad (3\text{-}33)$$

and further yields the Hartree potential V_{Hartree} as well as the exchange-correlation potential V_{XC}. Typically, one uses DFT for the treatment of V_{XC}, and the exact functional used ought to be consistent with the future pseudopotential calculations for solids or molecules. The final pseudopotential V_l^{ps} is derived as

$$V_l^{\mathrm{ps}}(r) = V_l^{\mathrm{ps,scr}}(r) - V_{\mathrm{Hartree}}[n_v(r)] - V_{\mathrm{XC}}[n_v(r)] \quad (3\text{-}34)$$

where the brackets imply that V_{Hartree} and V_{XC} are in principle functionals of $n_v(r)$. Under LDA and GGA, typical V_{XC} potentials (and also ϵ_{XC}) are highly nonlinear with respect to the electron density n, which brings additional issues in the unscreening step above. This is because the core electrons and valence electrons are treated separately in an ordinary pseudopotential approach, with the core charge density hidden behind the pseudopotential. Nevertheless, a local contribution $\epsilon_{\mathrm{XC}}(n_{\mathrm{all}}(\boldsymbol{r}))$ due to the total electron density there is not the sum of $\epsilon_{\mathrm{XC}}(n_{\mathrm{core}}(\boldsymbol{r}))$ and $\epsilon_{\mathrm{XC}}(n_{\mathrm{valence}}(\boldsymbol{r}))$, where n_{core}, n_{valence} and n_{all} denote the local core electron density, valence electron density and total electron density, respectively. Such nonlinearity inevitably leads to errors during unscreening. Hence, for the sake of accuracy, the pseudopotential files usually contain the fixed core charge densities as well, which should be considered together with the calculated valence electron charge densities to evaluate $\epsilon_{\mathrm{XC}}(\boldsymbol{r})$. The resulting technique, named nonlinear core correction, may however add to the numerical instability if not handled properly. The reason lies in that, the core charge densities are usually high and vary significantly over the space. Louie, Froyen and Cohen [91] proposed that within a certain radius R_0, it is feasible to use a simple spherical Bessel function to model the core charge distribution. The benefits are two-folds. On the one hand, the spherical Bessel function approach avoids any drastic change of charge density over the space. On the other hand, the fast Fourier transform (FFT) of such a density profile becomes rather easy. A guide for the choice of R_0 is that, at that radius the core charge density is around 1–2 times that of the valence charge density. Beyond R_0, however, the true core charge densities have to be stored faithfully. The core correction scheme by Louie, Froyen and Cohen has been widely implemented in modern pseudopotential-based codes.

The pseudopotential operator is directly linked to $V_l^{\mathrm{ps}}(r)$ according to equation (3-26), $\widehat{V}^{\mathrm{ps}}(r) = \sum_{l,m}|Y_{lm}\rangle V_l^{\mathrm{ps}}(r)\langle Y_{lm}|$. The practical calculation is, however, not as straightforward as the formula seems to be. Given any combination of l, m, one has to carry out an integral of r from 0 to ∞. This can be directly simplified if one notes that $V_l^{\mathrm{ps}}(r)$ of various l values only differ for the region of $r < R_{\mathrm{c}}$. Hence, one defines an l-independent local part of pseudopotential $V_{\mathrm{loc}}^{\mathrm{ps}}(r)$, which must be identical to $V_l^{\mathrm{ps}}(r)$ for $r > R_{\mathrm{c}}$. After separating out $V_{\mathrm{loc}}^{\mathrm{ps}}(r)$, the remaining part of $V_l^{\mathrm{ps}}(r)$ is written as $\delta V_l^{\mathrm{ps}}(r) = V_l^{\mathrm{ps}}(r) - V_{\mathrm{loc}}^{\mathrm{ps}}(r)$, which is nonzero only for $r < R_{\mathrm{c}}$. Therefore, the pseudopotential operator becomes

$$\widehat{V}^{\mathrm{ps}}(r) = V_{\mathrm{loc}}^{\mathrm{ps}}(r) + \sum_{l,m}|Y_{lm}\rangle\,\delta V_l^{\mathrm{ps}}(r)\,\langle Y_{lm}| \quad (3\text{-}35)$$

where $V_{\mathrm{loc}}^{\mathrm{ps}}(r)$ is independent of l, while $\sum_{l,m}|Y_{lm}\rangle\,\delta V_l^{\mathrm{ps}}(r)\,\langle Y_{lm}|$ is still semi-local.

In practice, the pseudopotential operator has to act on quantum states, especially those chosen as basis vectors. Provided that an orthonormal basis set $\{\phi_i\}$ is selected, such as the plane wave set, the local part of the pseudopotential matrix element reads

$$\langle\phi_i|\,V_{\mathrm{loc}}^{\mathrm{ps}}(r)\,|\phi_j\rangle = \int \mathbf{d}\boldsymbol{r}\phi_i^*(r,\theta,\varphi)\,V_{\mathrm{loc}}^{\mathrm{ps}}(r)\,\phi_j(r,\theta,\varphi). \quad (3\text{-}36)$$

Note that only one set of (r, θ, φ) variables should appear inside the integral. Within the position representation framework, evaluation of this matrix element is achieved through pointwise multiplication of the basis functions with $V_{\mathrm{loc}}^{\mathrm{ps}}$ at each spatial location, followed by integration over the entire domain. This exactly reflects the meaning of 'local'.

The semi-local part is written as

$$
\begin{aligned}
&\delta V_l^{\mathrm{ps}}\left(i,j\right)\\
&\quad = \langle \phi_i | \sum_{l,m} |Y_{lm}\rangle \, \delta V_l^{\mathrm{ps}}\left(r\right) \langle Y_{lm} | \phi_j \rangle \\
&\quad = \sum_{l,m} \int r^2 \mathrm{d}r \iint \sin\theta \, \mathrm{d}\theta \mathrm{d}\varphi \, \phi_i^*\left(r,\theta,\varphi\right) Y_{lm}\left(\theta,\varphi\right) \delta V_l^{\mathrm{ps}}\left(r\right) \\
&\qquad \times \iint \sin\theta' \mathrm{d}\theta' \mathrm{d}\varphi' \, Y_{lm}^*\left(\theta',\varphi'\right) \phi_j\left(r,\theta',\varphi'\right). \qquad (3\text{-}37)
\end{aligned}
$$

A plane wave can be expanded in terms of spherical waves, following the well-known Rayleigh formula [92]

$$
\begin{aligned}
\langle \boldsymbol{r} | \phi_j \rangle &= \frac{1}{\sqrt{\Omega}} \mathrm{e}^{i\boldsymbol{k}_j \cdot \boldsymbol{r}} = \frac{1}{\sqrt{\Omega}} \mathrm{e}^{i k_j r \cos\theta} \\
&= \frac{1}{\sqrt{\Omega}} \sum_{l=0}^{\infty} i^l \left(2l+1\right) j_l\left(k_j r\right) P_l\left(\cos\theta\right) \qquad (3\text{-}38)
\end{aligned}
$$

where the radial part in each term is the spherical Bessel function $j_l\left(k_j r\right)$, and P_l is Legendre polynomial. This is the most conventional presentation of the Rayleigh formula in quantum mechanics textbooks, but it obviously treats $\boldsymbol{k}_j$ and $\boldsymbol{r}$ on an unequal footing, because $\boldsymbol{k}_j$ is merely a parameter and only $\boldsymbol{r}$ is the variable. Nevertheless, from a pure mathematical standpoint, $\boldsymbol{k}_j$ and $\boldsymbol{r}$ are on equal footing in the term $\mathrm{e}^{i\boldsymbol{k}_j \cdot \boldsymbol{r}}$, thus a more general Rayleigh formula should write

$$
\mathrm{e}^{i\boldsymbol{k}_j \cdot \boldsymbol{r}} = 4\pi \sum_{l=0}^{\infty} \sum_{m=-l}^{l} i^l j_l\left(k_j r\right) Y_{lm}^*\left(\theta_{k_j}, \varphi_{k_j}\right) Y_{lm}\left(\theta_r, \varphi_r\right) \quad (3\text{-}39)
$$

where $\boldsymbol{r}$ explicitly represents a set of variables (r, θ_r, φ_r), but $\boldsymbol{k}$ is also expressed in spherical coordinates as (k, θ_k, φ_k). The above two equations are equivalent due to a relation between spherical Harmonics and the Legendre polynomial

$$
P_l\left(\cos\theta\right) = \frac{4\pi}{2l+1} \sum_{m=-l}^{l} Y_{lm}^*\left(\theta_{k_j}, \varphi_{k_j}\right) Y_{lm}\left(\theta_r, \varphi_r\right). \quad (3\text{-}40)
$$

Hence, $\delta V_l^{\mathrm{ps}}\left(i,j\right)$ may be expressed in a form with the radial variable separated from the angular variables, which facilitates the evaluation of equation (3-37).

An estimation of the computational complexity is necessary. Suppose there are N_{PW} plane waves in the basis set. For each angular momentum component l, it takes $N_{\mathrm{PW}}\left(N_{\mathrm{PW}}+1\right)/2$ integral operations to obtain all the semi-local parts of the Hamiltonian matrix elements. Note that there is no need to carry out N_{PW}^2 integral operations, thanks to the Hermicity of the Hamiltonian matrix. Given that the number of k points to sample the Brillouin zone is $N_k > 1$, then the number of integral operations becomes $N_k N_{\mathrm{PW}}\left(N_{\mathrm{PW}}+1\right)/2$.

Some well-known NCPPs include that developed by Bachelet, Hamann and Schlüter (BHS) [93], Kerker [94], as well as Troullier and Martins (TM) [95]. The work of BHS included pseudopotentials from H to Pu of the periodic table. They used tabulated parameters fitted in terms of analytic functions. The BHS pseudopotentials have been widely applied, but they are in general hard pseudopotentials that require more plane waves for expansion. Kerker designed an l-dependent mathematical form for the pseudo-wavefunctions, where the central part is a polynomial $p(r)$ with adjustable coefficients. To avoid any nodes of the pseudo-wavefunctions, it is $\exp\left[p\left(r\right)\right]$ instead of $p(r)$ that is used, such that $R_l\left(r\right) = r^l \exp\left[p\left(r\right)\right]$ for $r < R_{\mathrm{c}}$, where $R_l(r)$ is the radial part of the pseudo-wavefunction. One could obtain non-singular atomic pseudopotentials in this way, and in the original work of Kerker, $p(r)$ contains terms up to r^4. In 1991, TM extended the scheme of Kerker, allowing terms up to r^{12} in $p(r)$. This affords more flexibility to achieve smoother pseudopotentials. Furthermore, they require the matching of more derivatives at R_c for the pseudo-wavefunctions. The TM-type NCPPs have been extremely useful in practical calculations.

3.3. Fully separable Kleinman–Bylander type pseudopotential

Kleinman and Bylander (KB) made a great contribution in 1982 [79], that for computational efficiency the semi-local pseudopotentials may be re-written as non-local projectors, which are fully separable. The basic idea is to write the non-local part of the pseudopotential operator into two groups, which depend on $\boldsymbol{r}$ and $\boldsymbol{r}'$ respectively.

$$
\delta v_{lm}\left(\boldsymbol{r}, \boldsymbol{r}'\right) = \sum_i F_i\left(\boldsymbol{r}\right) G_i\left(\boldsymbol{r}'\right). \qquad (3\text{-}41)
$$

The original pseudopotential operator is semi-local in that it is non-local for angular variables, but local in radius. In the KB format, however, δv_{lm} is not specified for a given radius value r, but it depends on a pair of $\boldsymbol{r}$ and $\boldsymbol{r}'$, and it is assumed to be separable into $F_i\left(\boldsymbol{r}\right)$ and $G_i\left(\boldsymbol{r}'\right)$ parts. In this sense, the KB pseudopotential is regarded as fully non-local. However, equation (3-41) is initially proposed by assumption, thus one should require that the effect of $\delta v_{lm}\left(\boldsymbol{r}, \boldsymbol{r}'\right)$ is the same as $\delta V_l^{\mathrm{ps}}\left(r\right)$ when acting on a pseudo-wavefunction Φ_{lm}^{ps}. The non-local operator built by KB has the following form

$$
\delta \widehat{V}_{\mathrm{NL}} = \sum_{l,m} \delta v_{lm} = \sum_{l,m} \frac{\left|\Phi_{lm}^{\mathrm{ps}} \delta V_l^{\mathrm{ps}}\right\rangle \left\langle \delta V_l^{\mathrm{ps}} \Phi_{lm}^{\mathrm{ps}}\right|}{\left\langle \Phi_{lm}^{\mathrm{ps}} \middle| \delta V_l^{\mathrm{ps}} \middle| \Phi_{lm}^{\mathrm{ps}} \right\rangle} \qquad (3\text{-}42)
$$

where

$$
\delta v_{lm} = \frac{\left|\Phi_{lm}^{\mathrm{ps}} \delta V_l^{\mathrm{ps}}\right\rangle \left\langle \delta V_l^{\mathrm{ps}} \Phi_{lm}^{\mathrm{ps}}\right|}{\left\langle \Phi_{lm}^{\mathrm{ps}} \middle| \delta V_l^{\mathrm{ps}} \middle| \Phi_{lm}^{\mathrm{ps}} \right\rangle}. \qquad (3\text{-}43)
$$

The $\delta \widehat{V}_{\mathrm{NL}}$ operator satisfies

$$
\delta \widehat{V}_{\mathrm{NL}} \left|\Phi_{l'm'}^{\mathrm{ps}}\right\rangle = \delta V_{l'}^{\mathrm{ps}} \left|\Phi_{l'm'}^{\mathrm{ps}}\right\rangle. \qquad (3\text{-}44)
$$

Note that $\left\langle \delta V_l^{\mathrm{ps}} \Phi_{lm}^{\mathrm{ps}}\right|$ is the bra that first acts on the state ket, and it is different from $\left\langle \Phi_{lm}^{\mathrm{ps}}\right|$ because at each radial location it should be multiplied by $\delta V_l^{\mathrm{ps}}\left(r\right)$. While $\delta V_l^{\mathrm{ps}}\left(r\right)$ is semi-local, $\delta v_{lm}\left(\boldsymbol{r}, \boldsymbol{r}'\right)$ is non-local and may only be expressed in terms of projectors. Furthermore, the matrix element of $\delta \widehat{V}_{\mathrm{NL}}$ is written as

$$\begin{aligned}&\left\langle \phi_i \middle| \delta\widehat{V}_{\rm NL} \middle| \phi_j \right\rangle \\ &\quad = \sum_{l,m} \langle \phi_i | \Phi^{\rm ps}_{lm} \delta V^{\rm ps}_l \rangle \frac{1}{\langle \psi^{\rm ps}_{lm} \left| \delta V^{\rm ps}_l \right| \psi^{\rm ps}_{lm} \rangle} \langle \delta V^{\rm ps}_l \Phi^{\rm ps}_{lm} | \phi_j \rangle.\end{aligned} \tag{3-45}$$

This expression looks complicated, but in fact

$$\left\langle \phi_i \middle| \Phi^{\rm ps}_{lm} \delta V^{\rm ps}_l \right\rangle = \left(\left\langle \delta V^{\rm ps}_l \Phi^{\rm ps}_{lm} \middle| \phi_i \right\rangle \right)^* \tag{3-46}$$

therefore one does not need to calculate the integrals for pairs of i,j. Rather, one only needs to evaluate $\left\langle \delta V^{\rm ps}_l \Phi^{\rm ps}_{lm} \middle| \phi_i \right\rangle$ with i running over all plane waves. Hence, the number of integral operations is merely $N_{\rm PW}$, though an additional matrix multiplication operation is required. If the number of k points is N_k, $N_k N_{\rm PW}$ integral operations have to be carried out instead of $N_k N_{\rm PW}\left(N_{\rm PW}+1\right)/2$. To guarantee computational accuracy, $N_{\rm PW}$ is usually very large, thus the KB pseudopotential renders a considerable saving of computational time. Figure 5 demonstrates a typical example for the KB projectors for the 3s and 3p states of aluminum.

What is the trick of KB pseudopotential in terms of computational load reduction? It is actually not due to the non-local form: a non-local pseudopotential operator is mathematically more complicated than a semi-local pseudopotential operator. Rather, it is only the separable form that greatly reduces the number of integral operations. The non-local pseudopotential operator is efficient because it may be written as a fully separable form. However, in the conceptual sense, a non-local pseudopotential appears as projectors, which has a much more profound impact. This further stimulated Vanderbilt's USPP, the PAW method as well as Hamann's ONCV pseudopotential.

To understand how the concept of KB projectors can be extended, we consider the energy eigenvalue ε_l of a state with angular quantum number l. Given a particular choice of $V^{\rm ps}_{\rm loc}$, since the reference energy eigenvalue ε_l is also known for a specific l value, it follows that

$$\delta V^{\rm ps}_l(r) = \varepsilon_l - \widehat{T} - V^{\rm ps}_{\rm loc}(r). \tag{3-47}$$

Define

$$\chi_{lm} = \delta V^{\rm ps}_l \Phi^{\rm ps}_{lm} \tag{3-48}$$

which is named 'projector function', thus

$$\chi_{lm}(\boldsymbol{r}) = \left[\varepsilon_l - \widehat{T} - V^{\rm ps}_{\rm loc}(r)\right] \Phi^{\rm ps}_{lm}(\boldsymbol{r}) \tag{3-49}$$

and the final non-local pseudopotential operator is introduced as

$$\delta\widehat{V}_{\rm NL} = \sum_{l,m} \frac{|\chi_{lm}\rangle\langle\chi_{lm}|}{\langle \Phi^{\rm ps}_{lm} | \delta V^{\rm ps}_l | \Phi^{\rm ps}_{lm} \rangle}. \tag{3-50}$$

This does not look pretty due to the complicated term in the denominator. Provided that the denominator becomes unity, then it is clear that $\delta\widehat{V}_{\rm NL}$ is a sum of projectors. For the original KB-type NCPPs, each pair of l, m only corresponds to one projection operation. Nevertheless, for USPP, PAW and some improved NCPPs, there may exist multiple projection operations. The reason lies in that the atomic/ionic configuration in pseudopotential generation may not be similar to the chemical environments in application, such as in molecules and solids. A better pseudopotential should well describe the atom/ion under various valency configurations with a wide energy range. Suppose for each pair of l, m values, there are s reference energy eigenvalues $\varepsilon_{lm,1}, \varepsilon_{lm,2}, \varepsilon_{lm,3}, \cdots, \varepsilon_{lm,s}$, and accordingly s projector functions $\chi_{lm,1}, \chi_{lm,2}, \chi_{lm,3}, \cdots, \chi_{lm,s}$. As more reference energies are concerned, it is necessary to construct a matrix $\boldsymbol{B}_{lm}$ in order to account for the crossing terms between different reference energies. Define its matrix element as

$$\begin{aligned}\boldsymbol{B}_{lm,ij} &= \left\langle \Phi^{\rm ps}_{lm,i} \middle| \chi_{lm,j} \right\rangle = \left\langle \Phi^{\rm ps}_{lm,i} \middle| \delta V^{\rm ps}_l \Phi^{\rm ps}_{lm,j} \right\rangle \\ &= \left\langle \Phi^{\rm ps}_{lm,i} \middle| \delta V^{\rm ps}_l \middle| \Phi^{\rm ps}_{lm,j} \right\rangle\end{aligned} \tag{3-51}$$

where i and j stand for the row and column indices of the matrix $\boldsymbol{B}_{lm}$, respectively. For some reason that will become clear soon, a new set of basis can be established as

$$|\beta_{lm,i}\rangle = \sum_j \left(\boldsymbol{B}^{-1}_{lm}\right)_{ji} |\chi_{lm,j}\rangle \tag{3-52}$$

where $\boldsymbol{B}^{-1}_{lm}$ is nothing but the inverse matrix of $\boldsymbol{B}_{lm}$, which is also an $s \times s$ matrix that carries out the linear transformation of basis set χ into basis set β. The resulting basis functions (β functions) are the actual non-local parts of the pseudopotential files that are stored in various codes. The form of these basis functions after the above transformation can be proved to satisfy the following conditions

$$\begin{aligned}\left\langle \Phi^{\rm ps}_{lm,i} \middle| \beta_{lm,j} \right\rangle &= \left\langle \Phi^{\rm ps}_{lm,i} \middle| \sum_{j'} \left(\boldsymbol{B}^{-1}_{lm}\right)_{j'j} \middle| \chi_{lm,j'} \right\rangle \\ &= \sum_{j'} \left(\boldsymbol{B}^{-1}_{lm}\right)_{j'j} \left\langle \Phi^{\rm ps}_{lm,i} \middle| \chi_{lm,j'} \right\rangle \\ &= \sum_{j'} \left(\boldsymbol{B}^{-1}_{lm}\right)_{j'j} \left(\boldsymbol{B}_{lm}\right)_{ij'} = \delta_{ij}.\end{aligned} \tag{3-53}$$

The last equality is true because $\boldsymbol{B}^{-1}_{lm}$ multiplied by $\boldsymbol{B}_{lm}$ yields the identity matrix. Through the above transformation, the complex coupling relationship between $\left|\Phi^{\rm ps}_{lm,i}\right\rangle$ and $|\chi_{lm,i}\rangle$ is simplified. To understanding the meaning of equations (3-52) and (3-53), let us turn to a pure mathematical perspective. Suppose ξ_i and η_i are basis functions belonging to two different basis sets, and the condition $\langle \xi_i | \eta_j \rangle = \delta_{ij}$ is also called satisfying the biorthogonalization relation. Hence, one observes that though Φ and χ are not biorthogonal, since $\boldsymbol{B}_{lm}$ in general has non-zero off-diagonal elements, Φ and β satisfy the biorthogonalization relation. Moreover, the denominator term also disappears, and a KB-type NCPP has its non-local part expressed as

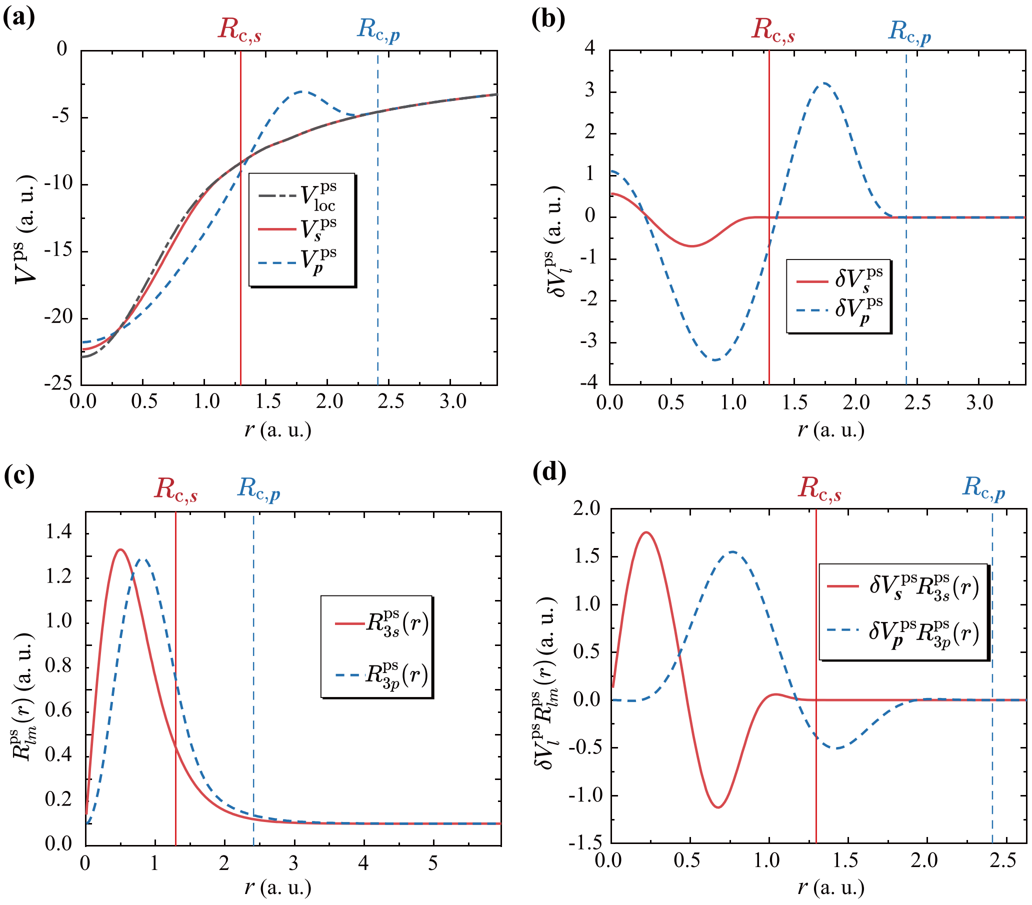

Figure 5. Comparison of the semi-local pseudopotentials and non-local pseudopotential projectors for Al. (a) Pseudopotentials V_l^{ps} for s and p electrons, along with the local pseudopotential part $V_{\mathrm{loc}}^{\mathrm{ps}}$. (b) Non-local part δV_l^{ps} as a difference obtained by subtracting $V_{\mathrm{loc}}^{\mathrm{ps}}$ from the s and p electron pseudopotentials. (c) Pseudo-wavefunctions R_{lm}^{ps} for 3s and 3p states. (d) Projector functions $\delta V_l^{\mathrm{ps}} R_{lm}^{\mathrm{ps}}$ in the non-local pseudopotential. The data were derived using the ONCV package [83].

$$\delta\widehat{V}_{\mathrm{NL}} = \sum_{l,m}\sum_{i,j} \boldsymbol{B}_{lm,ij} \left|\beta_{lm,i}\right\rangle \left\langle\beta_{lm,j}\right| \tag{3-54}$$

which is a simpler expression as proposed by Vanderbilt [80].

In case there is only one reference energy, then $\boldsymbol{B}_{lm}$ is reduced to a single value B_{lm}, expressed as

$$B_{lm} = \langle \Phi_{lm}^{\mathrm{ps}} | \chi_{lm} \rangle. \tag{3-55}$$

Therefore, one simply has

$$|\beta_{lm}\rangle = B_{lm}^{-1} |\chi_{lm}\rangle = \frac{|\chi_{lm}\rangle}{B_{lm}} \tag{3-56}$$

which verifies that

$$\delta\widehat{V}_{\mathrm{NL}} = \sum_{l,m} B_{lm} |\beta_{lm}\rangle\langle\beta_{lm}| = \sum_{l,m} B_{lm} \frac{|\chi_{lm}\rangle}{B_{lm}} \frac{\langle\chi_{lm}|}{B_{lm}}$$
$$= \sum_{l,m} \frac{|\chi_{lm}\rangle\langle\chi_{lm}|}{B_{lm}}. \tag{3-57}$$

This expression can be directly compared with equation (3-42).

3.4. USPP

In the last section we have discussed the Vanderbilt form of KB projectors. The USPP concept was also proposed by Vanderbilt [80], but it further sacrifices the norm-conserving condition for smoother pseudo-wavefunctions and smaller kinetic energy cutoff for the plane wave basis. This could be particularly useful for 2p, 3d and 4f electrons, whose original wavefunction is node-less and the norm-conserving condition forbids a substantially smoother pseudo-wavefunction than the original one. Figure 6 compares the degrees of 'pseudization' for Al 3s and C 2p wavefunctions using an NCPP scheme of Kerker [94], where it is clear that the pseudo-wavefunction is hardly any better than the all-electron version for a node-less 2p state. Yet, to allow for violating the norm-conserving condition, a smoother pseudo-wavefunction may become possible, with a certain procedure as explained below.

In generating a USPP as introduced by Vanderbilt, for each pair of l, m values, several reference energy eigenvalues $\varepsilon_{lm,1}, \varepsilon_{lm,2}, \cdots, \varepsilon_{lm,s}$ are pre-selected, while other processes are similar to that of NCPP, but an additional compensation charge must be introduced

$$Q_{lm,ij} = \left\langle \Phi_{lm,i}^{\mathrm{ae}} \middle| \Phi_{lm,j}^{\mathrm{ae}} \right\rangle_{R_c} - \left\langle \Phi_{lm,i}^{\mathrm{ps}} \middle| \Phi_{lm,j}^{\mathrm{ps}} \right\rangle_{R_c} \tag{3-58}$$

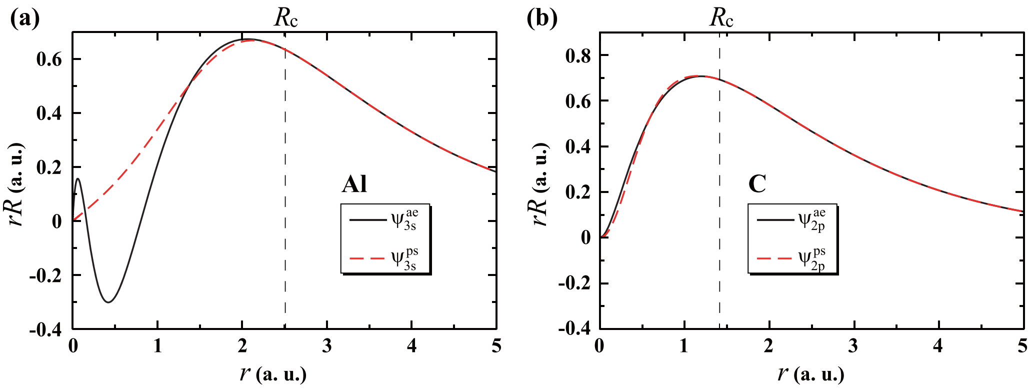

Figure 6. Comparison of the all-electron wavefunctions and typical Kerker-type pseudo-wavefunctions. (a) The 3s wavefunctions for Al, where the all-electron version contains two nodes; (b) the node-less 2p wavefunctions for C. The pseudo-wavefunctions were derived using the Opium package [96].

where $\Phi^{\text{ae}}_{lm,i}$ is the all-electron wavefunction for reference, and $\Phi^{\text{ps}}_{lm,i}$ is the corresponding pseudo-wavefunction. The subscript means that in evaluating the inner product in position representation, only the spherical region with $r \leqslant R_\text{c}$ is to be considered. For instance,

$$\langle \Phi^{\text{ae}}_{lm,i} | \Phi^{\text{ae}}_{lm,j} \rangle_{R_c} = \int_0^{R_c} \left[R^{\text{ae}}_{lm,i}(r)\right]^* R^{\text{ae}}_{lm,i}(r)\, r^2 \mathrm{d}r. \tag{3-59}$$

Practically, only the radial part $R^{\text{ae}}_{lm,i}(r)$ within $\Phi^{\text{ae}}_{lm,i}(\boldsymbol{r})$ is important. Because $R^{\text{ae}}_{lm,i}(r)$ can always be selected as real functions, there is no need to emphasize the complex conjugate operation. To sum up, $Q_{lm,ij} = 0$ equals the norm-conserving condition. In the USPP theory, $Q_{lm,ij} \neq 0$ is permitted to yield a possibly smoother pseudo-wavefunction.

Vanderbilt proved that [80]

$$\boldsymbol{B}_{lm,ij} - \boldsymbol{B}^*_{lm,ji} = (\varepsilon_i - \varepsilon_j)\, Q_{lm,ij} \tag{3-60}$$

thus the matrix $\boldsymbol{B}_{lm}$ is not Hermitian unless $Q_{lm,ij}$ are zero. He further defined an overlap operator as

$$\hat{S} = \hat{I} + \sum_{l,m} \sum_{i,j} Q_{lm,ij} \left|\beta_{lm,i}\right\rangle \left\langle \beta_{lm,j}\right| \tag{3-61}$$

which satisfies the following condition

$$\langle \Phi^{\text{ps}}_{lm,i} | \hat{S} | \Phi^{\text{ps}}_{lm,j} \rangle_{R_c} = \langle \Phi^{\text{ae}}_{lm,i} | \Phi^{\text{ae}}_{lm,j} \rangle_{R_c}. \tag{3-62}$$

And the $\boldsymbol{B}_{lm,ij}$ term in NCPP has to be replaced by

$$\boldsymbol{D}_{lm,ij} = \boldsymbol{B}_{lm,ij} + \varepsilon_{lm,j} Q_{lm,ij}. \tag{3-63}$$

Therefore, the final non-local pseudopotential operator for USPP reads

$$\delta \hat{V}^{\text{US}}_{\text{NL}} = \sum_{l,m} \sum_{i,j} \boldsymbol{D}_{lm,ij} \left|\beta_{lm,i}\right\rangle \left\langle \beta_{lm,j}\right|. \tag{3-64}$$

The reasoning of using matrix $\boldsymbol{D}$ instead of $\boldsymbol{B}$ is first related to the requirement of Hermicity. It follows that

$$\begin{aligned} \boldsymbol{D}_{lm,ij} - \boldsymbol{D}^*_{lm,ji} &= \boldsymbol{B}_{lm,ij} - \boldsymbol{B}^*_{lm,ji} + \varepsilon_j Q_{lm,ij} - \varepsilon_i Q^*_{lm,ji} \\ &= \boldsymbol{B}_{lm,ij} - \boldsymbol{B}^*_{lm,ji} - (\varepsilon_i - \varepsilon_j)\, Q_{lm,ij} = 0 \end{aligned} \tag{3-65}$$

where

$$Q^*_{lm,ji} = \left\langle \Phi^{\text{ae}}_{lm,j} \middle| \Phi^{\text{ae}}_{lm,i} \right\rangle^*_{R_c} - \left\langle \Phi^{\text{ps}}_{lm,j} \middle| \Phi^{\text{ps}}_{lm,i} \right\rangle^*_{R_c} = Q_{lm,ij}. \tag{3-66}$$

Hence, the matrix $\boldsymbol{D}$ is guaranteed to be Hermitian. The pseudo-wavefunction is the solution to the following generalized eigenvalue problem (t represents an index for energy)

$$\left(\hat{T} + V^{\text{ps}}_{\text{loc}} + \delta \hat{V}^{\text{US}}_{\text{NL}}\right) \Phi^{\text{ps}}_{lm,t} = \varepsilon_{lm,t} \hat{S} \Phi^{\text{ps}}_{lm,t}. \tag{3-67}$$

The left hand side is expressed as

$$\begin{aligned} &\left(\hat{T} + V^{\text{ps}}_{\text{loc}} + \delta \hat{V}^{\text{US}}_{\text{NL}}\right) \Phi^{\text{ps}}_{lm,t} \\ &= \left(\hat{T} + V^{\text{ps}}_{\text{loc}} + \sum_{l',m'} \sum_{i,j} B_{l'm',ij} \left|\beta_{l'm',i}\right\rangle \left\langle \beta_{l'm',j}\right|\right) \Phi^{\text{ps}}_{lm,t} \\ &\quad + \sum_{l',m'} \sum_{i,j} \varepsilon_{l'm',j} Q_{l'm',ij} \left|\beta_{l'm',i}\right\rangle \left\langle \beta_{l'm',j}\right| \Phi^{\text{ps}}_{lm,t} \\ &= \left(\hat{T} + V^{\text{ps}}_{\text{loc}} + \sum_{l',m'} \sum_{i,j} B_{l'm',ij} \left|\beta_{l'm',i}\right\rangle \left\langle \beta_{l'm',j}\right|\right) \Phi^{\text{ps}}_{lm,t} \\ &\quad + \sum_{i} \varepsilon_{lm,t} Q_{lm,it} \left|\beta_{lm,i}\right\rangle \end{aligned} \tag{3-68}$$

where the right hand side is

$$\begin{aligned} &\varepsilon_{lm,t} \hat{S} \Phi^{\text{ps}}_{lm,t} \\ &= \varepsilon_{lm,t} \Phi^{\text{ps}}_{lm,t} + \varepsilon_{lm,t} \sum_{l',m'} \sum_{i,j} Q_{l'm',ij} \left|\beta_{l'm',i}\right\rangle \left\langle \beta_{l'm',j}\right| \Phi^{\text{ps}}_{lm,t} \\ &= \varepsilon_{lm,t} \Phi^{\text{ps}}_{lm,t} + \sum_{i} \varepsilon_{lm,t} Q_{lm,it} \left|\beta_{lm,i}\right\rangle. \end{aligned} \tag{3-69}$$

In comparing the two, their last terms are exactly equal. Meanwhile, the rest terms are consistent with the case of

NCPPs. Hence, through solving this generalized eigenvalue problem, one recovers the stationary Schrödinger equation.

In calculating a solid with USPP, the pseudo-wavefunction $\tilde{\psi}_n$ is not norm-conserving, thus the electron density cannot simply be obtained through the modulus square of $\tilde{\psi}_n$. The compensation charge $Q_{lm,ij}$ has to be involved in the density calculation

$$n_v(\boldsymbol{r}) = \sum_n^{\text{occ}} \tilde{\psi}_n^*(\boldsymbol{r})\,\tilde{\psi}_n(\boldsymbol{r}) + \sum_{l,m}\sum_{i,j} \rho_{lm,ij} Q_{lm,ij}(\boldsymbol{r}) \tag{3-70}$$

where 'occ' stands for occupied states, $\rho_{lm,ij} = \sum_n^{\text{occ}} \langle\tilde{\psi}_n|\beta_{lm,i}\rangle\langle\beta_{lm,j}|\tilde{\psi}_n\rangle$ and the pseudo-wavefunctions ought to meet the generalized orthogonal condition $\left\langle\tilde{\psi}_n\middle|\hat{S}\middle|\tilde{\psi}_{n'}\right\rangle = \delta_{nn'}$.

3.5. Projector augmented-wave method

PAW is a widely used technique that was proposed by Blöchl in 1994 [81]. To understand its formulation, one may first review the key process in the OPW method (or the APW method, but here we select OPW for example). In the OPW formulation, the valence electron wavefunction $\psi_{n,\boldsymbol{k}}$ is a linear combination of many OPWs

$$\begin{aligned}
\psi_{n,\boldsymbol{k}}(\boldsymbol{r}) &= \sum_{\boldsymbol{G}_m} c_{\boldsymbol{k}}(\boldsymbol{G}_m)\,\phi_{\boldsymbol{k}+\boldsymbol{G}_m}(\boldsymbol{r}) \\
&\quad - \sum_{\boldsymbol{G}_m}\sum_j c_{\boldsymbol{k}}(\boldsymbol{G}_m)\,\langle\Psi_{j,\boldsymbol{k}}|\phi_{\boldsymbol{k}+\boldsymbol{G}_m}\rangle\,\Psi_{j,\boldsymbol{k}}(\boldsymbol{r}) \\
&= \sum_{\boldsymbol{G}_m} c_{\boldsymbol{k}}(\boldsymbol{G}_m)\,\phi_{\boldsymbol{k}+\boldsymbol{G}_m}(\boldsymbol{r}) \\
&\quad - \sum_j |\Psi_{j,\boldsymbol{k}}\rangle\langle\Psi_{j,\boldsymbol{k}}| \sum_{\boldsymbol{G}_m} c_{\boldsymbol{k}}(\boldsymbol{G}_m)\,\phi_{\boldsymbol{k}+\boldsymbol{G}_m}(\boldsymbol{r}) \\
&= \tilde{\psi}_{n,\boldsymbol{k}}(\boldsymbol{r}) - \sum_j |\Psi_{j,\boldsymbol{k}}\rangle\langle\Psi_{j,\boldsymbol{k}}|\tilde{\psi}_{n,\boldsymbol{k}}(\boldsymbol{r}) \\
&= \left(\hat{I} - \sum_j |\Psi_{j,\boldsymbol{k}}\rangle\langle\Psi_{j,\boldsymbol{k}}|\right)\tilde{\psi}_{n,\boldsymbol{k}}(\boldsymbol{r})
\end{aligned} \tag{3-71}$$

where $\phi_{\boldsymbol{k}+\boldsymbol{G}_m}$ is a plane wave with wavevector $\boldsymbol{k}+\boldsymbol{G}_m$, and $c_{\boldsymbol{k}}(\boldsymbol{G}_m)$ is the corresponding expansion coefficient. Note that $\tilde{\psi}_{n,\boldsymbol{k}}(\boldsymbol{r})$ is simply a combination of plane waves. And $\Psi_{j,\boldsymbol{k}}$ represents core orbital Bloch functions, since the contribution of atomic orbitals has to be considered in an OPW. The APW method is similar in this respect, but it explicitly involves a critical radius to cut the space into augmentation regions and the interstitial region, *i.e.* the muffin-tin potential [97]. In OPW, the space is not manually divided into augmentation regions and the interstitial region, nevertheless.

The significance of equation (3-71) lies in that, it is possible to construct a linear transformation that links $\psi_{n,\boldsymbol{k}}$ and $\tilde{\psi}_{n,\boldsymbol{k}}$

$$|\psi_{n,\boldsymbol{k}}\rangle = \hat{\mathfrak{T}}_{\text{OPW}}\left|\tilde{\psi}_{n,\boldsymbol{k}}\right\rangle \tag{3-72}$$

where the transformation operator is simply

$$\hat{\mathfrak{T}}_{\text{OPW}} = \hat{I} - \sum_j |\Psi_{j,\boldsymbol{k}}\rangle\langle\Psi_{j,\boldsymbol{k}}|. \tag{3-73}$$

In principle, one may merely obtain the smooth functions $\tilde{\psi}_{n,\boldsymbol{k}}$, while a later linear transformation yields the full wavefunction $\psi_{n,\boldsymbol{k}}$. This could be particularly useful if, say, a later *GW* calculation [98] is to be carried out.

It follows that the mathematical form of $\hat{\mathfrak{T}}$ is of significance to convert $\tilde{\psi}_n$ into ψ_n, where the index n actually represents a combination of wavevector $\boldsymbol{k}$, band index as well as the spin index. Similar to OPW, in the PAW method one also has

$$\begin{aligned}
\psi_n(\boldsymbol{r}) &= \hat{\mathfrak{T}}\tilde{\psi}_n(\boldsymbol{r}) \\
\tilde{\psi}_n(\boldsymbol{r}) &= \hat{\mathfrak{U}}\psi_n(\boldsymbol{r}) \\
\hat{\mathfrak{T}} &= \hat{\mathfrak{U}}^{-1}
\end{aligned} \tag{3-74}$$

where $\hat{\mathfrak{U}}$ is the inverse transformation of $\hat{\mathfrak{T}}$. A reasonable guess is to use a similar form as in OPW, *i.e.*

$$\hat{\mathfrak{T}} = \hat{I} + \sum_{\boldsymbol{R}} \hat{S}_{\boldsymbol{R}} \tag{3-75}$$

where the sum runs for all atoms. Therefore, an $\hat{S}_{\boldsymbol{R}}$ operator should be established for each atom. $\hat{S}_{\boldsymbol{R}}$ should represent the difference between ψ_n and $\tilde{\psi}_n$ at atomic position $\boldsymbol{R}$, which is related to the difference between the all-electron partial waves $\Phi_i(\boldsymbol{r})$ and pseudo-partial waves $\tilde{\Phi}_i(\boldsymbol{r})$ of the atom at $\boldsymbol{R}$. The subscript i represents the abbreviation of atomic position $\boldsymbol{R}$, angular momentum quantum numbers l, m, and possibly discriminating between s reference eigenvalues $\varepsilon_{lm,1}$—$\varepsilon_{lm,s}$. The all-electron partial waves $\Phi_i(\boldsymbol{r})$ are obtained through an all-electron calculation, and the pseudo-partial waves $\tilde{\Phi}_i(\boldsymbol{r})$ are the same as $\Phi_i(\boldsymbol{r})$ outside the core radius $R_{c,l}$. The effect of $\hat{S}_{\boldsymbol{R}}$ ought to be

$$\hat{S}_{\boldsymbol{R}}\left|\tilde{\Phi}_i\right\rangle = |\Phi_i\rangle - \left|\tilde{\Phi}_i\right\rangle. \tag{3-76}$$

Within the augmentation area, the smooth function $\tilde{\psi}_n(\boldsymbol{r})$ may be expanded in terms of the basis set $\{\tilde{\Phi}_i\}$

$$\tilde{\psi}_n(\boldsymbol{r}) = \sum_i c_{n,i}\tilde{\Phi}_i(\boldsymbol{r}) \tag{3-77}$$

and the coefficient $c_{n,i}$ is given through a bra $\langle\tilde{p}_i|$ (i covers all atoms), whose principal role is to project $\left|\tilde{\psi}_n\right\rangle$ onto $\left|\tilde{\Phi}_i\right\rangle$ at the atomic position $\boldsymbol{R}$

$$c_{n,i} = \left\langle\tilde{p}_i\middle|\tilde{\psi}_n\right\rangle. \tag{3-78}$$

Hence, the expansion of the pseudo-wavefunction is written in terms of the Dirac notation as

$$\left|\tilde{\psi}_n\right\rangle = \sum_i \left|\tilde{\Phi}_i\right\rangle\left\langle\tilde{p}_i\middle|\tilde{\psi}_n\right\rangle. \tag{3-79}$$

And the following orthonormal relation is respected

$$\left\langle\tilde{p}_i\middle|\tilde{\Phi}_j\right\rangle = \delta_{ij} \tag{3-80}$$

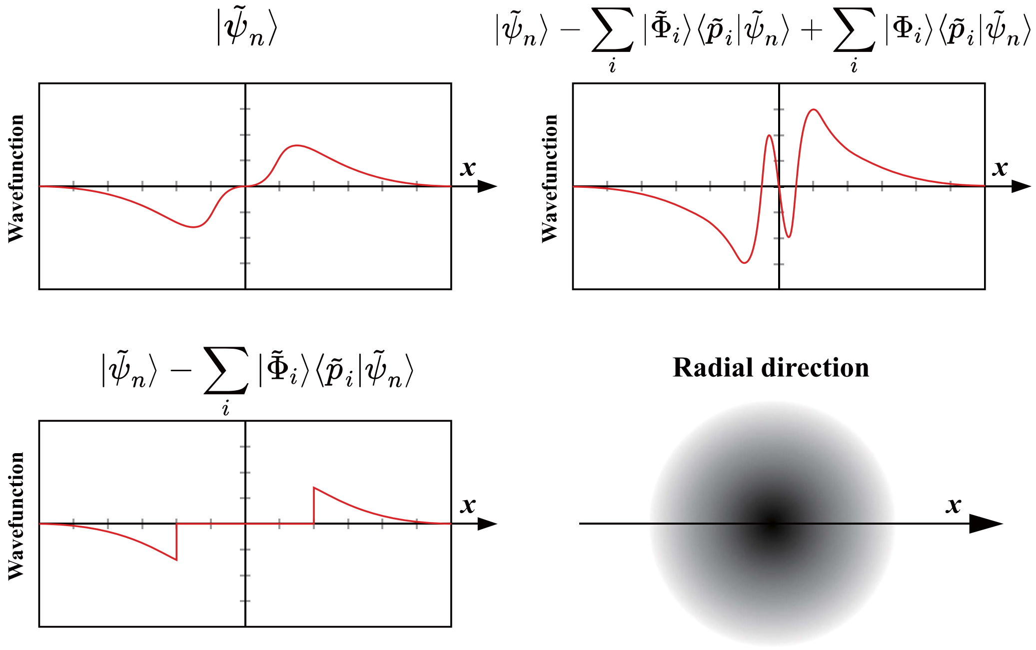

Figure 7. The procedure to recover the full wavefunction ψ_n from the pseudo-wavefunction $\tilde{\psi}_n$ in the PAW method, where representative wavefunctions are demonstrated.

to guarantee that the transformation is linear. The actual form of $\langle\tilde{p}_i|$ is relatively complicated, and a comprehensive derivation is provided in Blöchl's original work [81]. It turns out that

$$\begin{aligned}\hat{S}_{\boldsymbol{R}}\left|\tilde{\psi}_n\right\rangle &= \hat{S}_{\boldsymbol{R}}\sum_i\left|\tilde{\Phi}_i\right\rangle\left\langle\tilde{p}_i|\tilde{\psi}_n\right\rangle \\ &= \sum_i\left(|\Phi_i\rangle - \left|\tilde{\Phi}_i\right\rangle\right)\left\langle\tilde{p}_i\middle|\tilde{\psi}_n\right\rangle \end{aligned} \tag{3-81}$$

which yields the expression for the linear transformation operator

$$\hat{\mathcal{T}} = \hat{I} + \sum_i\left(|\Phi_i\rangle - \left|\tilde{\Phi}_i\right\rangle\right)\langle\tilde{p}_i|. \tag{3-82}$$

To construct ψ_n from $\tilde{\psi}_n$, one finds

$$\begin{aligned}\psi_n(\boldsymbol{r}) = \hat{\mathcal{T}}\tilde{\psi}_n(\boldsymbol{r}) = \tilde{\psi}_n(\boldsymbol{r}) &- \sum_i\left|\tilde{\Phi}_i\right\rangle\left\langle\tilde{p}_i\middle|\tilde{\psi}_n\right\rangle \\ &+ \sum_i|\Phi_i\rangle\left\langle\tilde{p}_i\middle|\tilde{\psi}_n\right\rangle. \end{aligned} \tag{3-83}$$

A typical such procedure is illustrated in figure 7.

Suppose one is concerned with a specific operator $\hat{A}$ in the all-electron calculation. In the PAW formulation there is a corresponding operator, obtained through a unitary transformation that is common in quantum mechanics

$$\tilde{A} = \mathcal{T}^{\dagger}\hat{A}\mathcal{T} = \hat{A} + \sum_{i,j}|\tilde{p}_i\rangle\left(\left\langle\Phi_i\middle|\hat{A}\middle|\Phi_j\right\rangle - \left\langle\tilde{\Phi}_i\middle|\hat{A}\middle|\tilde{\Phi}_j\right\rangle\right)\langle\tilde{p}_j|. \tag{3-84}$$

The expectation value of $\hat{A}$ is consistent with that of $\tilde{A}$ in the PAW formulation

$$\left\langle\hat{A}\right\rangle = \left\langle\psi_n\middle|\hat{A}\middle|\psi_n\right\rangle = \left\langle\tilde{\psi}_n\middle|\tilde{A}\middle|\tilde{\psi}_n\right\rangle. \tag{3-85}$$

Hence, provided that one would like to work within the PAW framework, the standard Hermitian operators (representing observables in reality) must be modified. The most significant observable in DFT is the electron density. Its corresponding operator is revised as

$$\begin{aligned} n(\boldsymbol{r}) &= \tilde{n}(\boldsymbol{r}) + n^1(\boldsymbol{r}) - \tilde{n}^1(\boldsymbol{r}) \\ &= \sum_n f_n\left\langle\tilde{\psi}_n\middle|\boldsymbol{r}\right\rangle\left\langle\boldsymbol{r}\middle|\tilde{\psi}_n\right\rangle + \sum_{i,j}\rho_{ij}\langle\Phi_i|\boldsymbol{r}\rangle\langle\boldsymbol{r}|\Phi_j\rangle \\ &\quad - \sum_{i,j}\rho_{ij}\left\langle\tilde{\Phi}_i\middle|\boldsymbol{r}\right\rangle\left\langle\boldsymbol{r}\middle|\tilde{\Phi}_j\right\rangle \end{aligned} \tag{3-86}$$

where f_n is the occupation number of electronic state n, and $\rho_{ij} = \sum_n f_n\langle\tilde{\psi}_n|\tilde{p}_i\rangle\langle\tilde{p}_j|\tilde{\psi}_n\rangle$ is regarded as the occupation of the augmentation channel (i,j). Note that n^1 and $\tilde{n}^1$ have to be evaluated on spherical auxiliary grids on individual atoms, while $\tilde{n}$ is still evaluated on a regular grid of the solid. A graphic demonstration of such procedure is given in figure 8.

The disadvantage of the PAW method is clearly the increased complexity, especially regarding two types of grids: radial grids and the regular grid. For instance, to calculated the Hartree energy $\int\int \mathrm{d}\boldsymbol{r}\mathrm{d}\boldsymbol{r}' n_1(\boldsymbol{r})\, n_2(\boldsymbol{r}')/|\boldsymbol{r}-\boldsymbol{r}'|$, both grids have to be implemented, which requires certain transformations for $\tilde{n}$, n^1, and $\tilde{n}^1$. Fortunately, there are certain tricks that may circumvent this complicated problem, and the reader is encouraged to refer to the original work of Blöchl [81], or that of Kresse and Joubert [99].

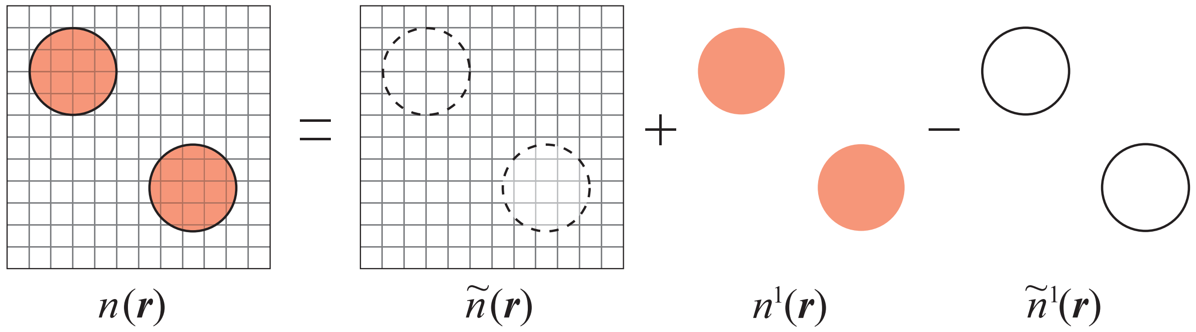

Figure 8. Evaluation of $n(r)$ based on two types of grids.

3.6. ONCV pseudopotential

In general, USPP and PAW enable using a smaller kinetic energy cutoff compared with NCPPs. The PAW method further allows for extracting the full electron wavefunctions, at the cost of a more complicated theoretical form. Notwithstanding their advantages in terms of the pseudopotential softness, they become too complicated for certain applications such as DFPT. Indeed, NCPP is still the most natural and straightforward concept in the area of pseudopotential, thus it is being continuously studied and improved. Keeping the norm-conservation condition could bring about certain conveniences in many applications. The ONCV pseudopotential is a recent innovation in this direction.

In the theory of ONCV pseudopotential, a generalized RRKJ method is utilized for pseudization, *i.e.* 'optimized'. RRKJ refers to a classic work by Rappe, Rabe, Kaxiras and Joannopoulos [100]. Compared with RRKJ, the main difference lies in that for each angular quantum number l, several projectors are used in the ONCV method, like Vanderbilt's USPP. To optimize a pseudopotential, the key is to allow for a smaller kinetic energy cutoff while not sacrificing the accuracy. A natural strategy for accuracy/efficiency evaluation is to calculate the residual kinetic energy, given that a certain cutoff energy

$$E_{\text{cut}} = \frac{q_{\text{c}}^2}{2} \tag{3-87}$$

is adopted. Following the convention of RRKJ [100] as well as Hamann [83], here we let $q = |\boldsymbol{k}|$, therefore q_{c} with a wavevector unit is a more convenient parameter that reflects the cutoff energy. The residual kinetic energy is the key quantity that estimates how much is discarded in truncating the plane wave basis. Since the optimization process in RRKJ pseudopotentials serves as the foundation for ONCV, the methodology of RRKJ will first be reviewed.

As usual, a pseudopotential is derived by inverting the Schrödinger equation, based upon a previously well-designed pseudo-wavefunction. The famous Kerker-type and TM-type NCPPs use the design $R_l(r) = r^l \exp[p(r)]$ for the core region, but this is not the sole choice. Actually, the radial wavefunction can naturally be expanded in terms of spherical Bessel functions (the spherical Bessel function has also been used for imitating the core charge distribution in nonlinear core correction, cf section 3.2). This is because under the spherical coordinates, one obtains the radial Schrödinger equation after separation of variables as (note that $q^2 = k^2$)

$$\frac{1}{r^2}\frac{\mathrm{d}}{\mathrm{d}r}\left(r^2\frac{\mathrm{d}R}{\mathrm{d}r}\right) + \left[q^2 - \frac{l(l+1)}{r^2}\right]R = 0. \tag{3-88}$$

If one simply lets

$$\begin{cases} x = qr \\ y(x) = R(r) \end{cases} \tag{3-89}$$

then equation (3-89) takes the form of the well-known spherical Bessel equation

$$\frac{\mathrm{d}^2 y}{\mathrm{d}x^2} = \left[\frac{l(l+1)}{x^2} - 1\right]y - \left(\frac{2}{x}\right)\frac{\mathrm{d}y}{\mathrm{d}x} \tag{3-90}$$

whose general solution is the superposition of spherical Bessel functions and spherical Neumann functions. However, the latter are divergent at the origin, thus the radial function $R(r)$ in an atomic problem can be written as the superposition of spherical Bessel functions $j_l(qr)$. Note that the expansion in terms of spherical Bessel functions here is not like in treating the stationary scattering problems. In partial wave analysis, one needs the spherical functions of various l values. In the pseudopotential problem, l is nevertheless given in advance, as a fixed quantum number. The various spherical Bessel functions are merely different in their wavevector q values, but they all share the same l value. The RRKJ scheme is to first expand the pseudo-wavefunction, denoted as $F(r)$ following the convention of that paper, in terms of the spherical Bessel functions. Of course this is limited to the region $r \leqslant R_{\text{c}}$, and for $r > R_{\text{c}}$ the pseudo-wavefunction ought to be identical to the all-electron wavefunction. $F(r)$ is not the optimized pseudo-wavefunction, but an additional $C(r)$ correction function should be added to $F(r)$ to yield the optimized pseudo-wavefunction $\tilde{R}(r) = F(r) + C(r)$. Hence, in the RRKJ scheme, $F(r)$ and $C(r)$ ought to be discussed separately.

The first question regarding $F(r)$ is, how many constraints it has to satisfy. The other question is related to the number of spherical Bessel functions to expand $F(r)$. It is most straightforward to require that $F(r = R_c)$ should equal the all-electron wavefunction there, rendering constraint $\mathcal{C}_1$, but this is not enough. When inverting the Schrödinger equation, as shown in equation (3-32), one should take the second derivative of the pseudo-wavefunction so as to obtain the pseudopotential. To guarantee that the pseudopotential is continuous, the first and second derivatives of the pseudo-wavefunction must be continuous. This brings about two addition constraints $\mathcal{C}_2$ (continuity of the first derivative) and $\mathcal{C}_3$ (continuity of the second derivative). Suppose $F(r)$ is expressed in terms of three spherical Bessel functions

$$F(r) = \alpha_1 j_l(\acute{q}_1 r) + \alpha_2 j_l(\acute{q}_2 r) + \alpha_3 j_l(\acute{q}_3 r). \qquad (3\text{-}91)$$

Here we use the symbol $\acute{q}$ to emphasize that it is for the expansion of $F(r)$. The wavevectors $\acute{q}_1$, $\acute{q}_2$ and $\acute{q}_3$ can be chosen to let the logarithmic derivative of the spherical Bessel function equal that of the all-electron wavefunction at $r = R_c$, *i.e.*

$$\left.\frac{\mathrm{d}\ln j_l(\acute{q}_i r)}{\mathrm{d}r}\right|_{r=R_\mathrm{c}} = \left.\frac{\mathrm{d}\ln R_l^{\mathrm{ae}}(r)}{\mathrm{d}r}\right|_{r=R_\mathrm{c}}. \qquad (3\text{-}92)$$

for $i = 1, 2, 3$. In other words, the values of $\acute{q}_1$, $\acute{q}_2$ and $\acute{q}_3$ are not set for the three constraints. Rather, the expansion coefficients α_1, α_2 and α_3 should be calculated according to the three constraints. However, the logarithmic derivative relation for each component of $F(r)$, *i.e.* $j_l(\acute{q}_i r)$, renders an automatic validity of $\mathcal{C}_2$, given that $\mathcal{C}_1$ is satisfied. This is exactly the benefit of using the logarithmic derivative concept for wavefunctions. Hence, the following two constraints have to be respected

$$\begin{array}{l} \mathcal{C}_1(\alpha_1, \alpha_2, \alpha_3) = 0 \\ \mathcal{C}_3(\alpha_1, \alpha_2, \alpha_3) = 0 \end{array}. \qquad (3\text{-}93)$$

On the other hand, the normalization condition for $F(r)$ proposes another constraint for the three coefficients

$$\mathcal{C}_4(\alpha_1, \alpha_2, \alpha_3) = 0. \qquad (3\text{-}94)$$

It seems as if the three coefficients can readily be fixed by the three constraints, but one of the constraints, $\mathcal{C}_4$, is not linear (but quadratic) with respect to the coefficients. Consequently, the problem is not as simple as a system of linear equations in three variables, and adjusting the three coefficients cannot always meet the three constraints. A simple illustration of this problem is given in figure 9. To solve a system of three linear algebraic equations

$$f(x, y, z) = 0;\ g(x, y, z) = 0;\ h(x, y, z) = 0 \qquad (3\text{-}95)$$

is equivalent to determining the coordinates of the intersection point regarding three planes

$$z = z_f(x, y);\ z = z_g(x, y);\ z = z_h(x, y). \qquad (3\text{-}96)$$

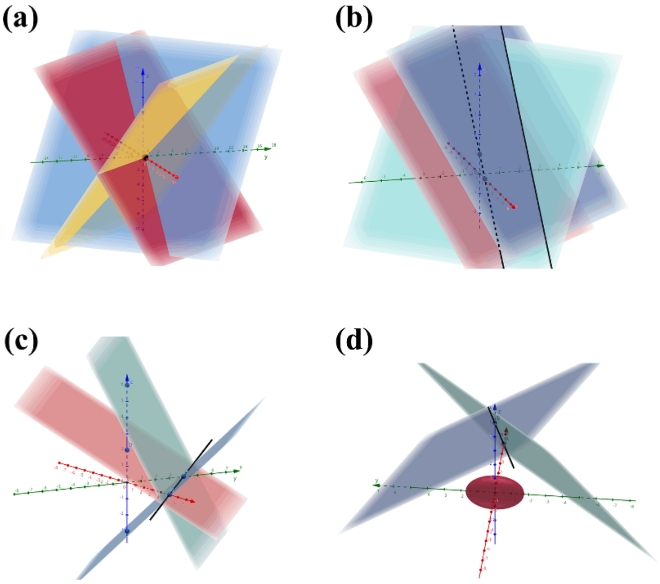

Figure 9. Solution to a system of three equations with three variables via a graphic method. (a) All three equations are linear, and only one solution exists; (b) all three equations are linear, and no solution exists because two planes are in parallel; (c) all three equations are linear, and infinitely many solutions exist; (d) a nonlinear (quadratic) equation introduces the possibility of no real solution, depending on the specific geometric configuration.

And in normal cases there is one and only one intersection point, as exemplified by figure 9(a). Indeed, there are cases where no solution exists at all (figure 9(b)), or there can be infinitely many solutions (figure 9(c)), but these are merely special cases. If one of the equations is, however, quadratic, then the problem is equivalent to the case of figure 9(d). Here, the ellipsoid stemming from the quadratic constraint is set as a 'small' one, such that is has no intersection point with the other two planes. This cannot be regarded as a special case, and that is why some additional flexibility has to be provided for $F(r)$ in order to guarantee a solution.

Hence, in the RRKJ scheme, it requires

$$F(r) = \alpha_1 j_l(\acute{q}_1 r) + \alpha_2 j_l(\acute{q}_2 r) + \alpha_3 j_l(\acute{q}_3 r) + \alpha_4 j_l(\acute{q}_4 r) \qquad (3\text{-}97)$$

where $j_l(\acute{q}_4 r)$ should also meet the logarithmic derivative relation, and α_4 could be arbitrarily selected as long as a definite solution could be found for α_1—α_3. Although $F(r)$ meets the required constraints, it is still an unoptimized pseudo-wavefunction.

To obtain an optimized pseudopotential, one needs to figure out a proper correction function $C(r)$, which must be zero at $r = R_\mathrm{c}$ (so as not to destroy the good constraints obeyed by $F(r)$) and also for $r > R_\mathrm{c}$. Again, $C(r)$ is expanded in terms of spherical Bessel functions

$$C(r) = \sum_{i=1}^{N_C} \beta_i j_l(q_i r) \qquad (3\text{-}98)$$

and there is no need to require exactly $N_C = 4$ because the expansion of $C(r)$ is independent to that of $F(r)$. And here we use q_i instead of $\acute{q}_i$, to emphasize the difference with respect to the $F(r)$ expansion. The choice of q_i must satisfy the following requirement

$$j_l(q_i R_c) = 0, \qquad i = 1, 2, \cdots, N_C \qquad (3\text{-}99)$$

otherwise the resulting pseudo-wavefunction $\tilde{R}(r) = F(r) + C(r)$ cannot be made continuous at R_c. Moreover, the choice of β_i should let the final pseudo-wavefunction $\tilde{R}_l(r)$ continuous up to its second derivative, and $\tilde{R}_l(r)$ should be normalized at the selected β_i values. Under these constraints, the coefficients β_i should be optimized to reach a minimal residual kinetic energy E_l^r, which is the difference between the expectation of the kinetic energy operator under the state $\tilde{R}_l(r)$, and that of the kinetic energy components for $q \leqslant q_\mathrm{c}$

$$E_l^r = \int_{r=0}^{\infty} r^2 \mathrm{d}r \tilde{R}_l^*(r) \left(-\frac{1}{2}\nabla^2\right) \tilde{R}_l(r) - \int_0^{q_\mathrm{c}} \mathrm{d}q \left|\tilde{R}_l(q)\right|^2 \frac{q^2}{2}. \tag{3-100}$$

To guarantee that E_l^r could be minimized, it is natural to use $N_C > 4$ for more optimization scope. The Lagrange multiplier method is a natural approach to transform such a constrained optimization problem into a simpler unconstrained optimization problem, and is therefore used to optimize β_i. Besides the optimizable coefficients β_i, the RRKJ method involves two global parameters q_c and R_c, both are up to the user to adjust. Without the optimization procedure, the user may only select a small R_c to ensure the transferability of the pseudopotential, which inevitably leads to a large q_c, *i.e.* a hard pseudopotential. Using the RRKJ scheme, however, one may still use the same R_c, but q_c can be made smaller upon carrying out the optimization. In addition, one could also consider setting a larger R_c value, while the quality of the RRKJ-optimized pseudopotential is still adequate for the applications, using the optimal q_c.

In the RRKJ scheme, though the pseudopotential is continuous at $r = R_\mathrm{c}$ (because the pseudo-wavefunction is continuous up to the 2nd derivative), there is no guarantee for the derivative of the pseudopotential. For applications like DFPT (which is also the major objective of ONCV), one needs to take the second derivative of the pseudopotential, which requires that the pseudo-wavefunction is continuous up to its 4th derivative. Hence, Hamann considered a more general case where the pseudo-wavefunction should be continuous up to its (M–1)th derivative. On account of the fixed nature of angular quantum number l, we shall denote the all-electron wavefunction and pseudo-wavefunction as Φ and $\tilde{\Phi}$, respectively, without bothering stating the l value. In addition, within the ONCV framework, transformations between various basis sets are frequently required. To clarify these operations, we introduce the following convention, exactly following Hamann.

- The symbol $\{\xi_i\}$ denotes a generic basis set.
- Specific basis sets are distinguished through superscript labels. And four basis sets, $\{\xi_i^B\}$, $\{\xi_i^O\}$, $\{\xi_i^N\}$ and $\{\xi_i^R\}$, will be encountered below.

The ONCV methodology still initiates with the construction of a basis set, through which the target pseudo-wavefunction is systematically expanded. The expansion coefficients are subsequently subjected to variational optimization to yield softer pseudopotentials. Let us constitute a first basis set $\{\xi_i^B\}$ from spherical Bessel functions, which involves N different q_i values

$$\xi_i^B = \begin{cases} j_l(q_i r), & r \leqslant R_\mathrm{c} \\ 0, & r > R_\mathrm{c} \end{cases}. \tag{3-101}$$

The selection criteria for the parameters q_i remain an open question in the current framework, which we defer to subsequent discussions. Fundamentally, one is permitted to select those q_i values such that $\{\xi_i^B\}$ is not an orthogonal basis set. To address this inherent non-orthogonality, a preliminary orthogonalization procedure is first required. The Löwdin symmetric orthogonalization method [101] could be used to yield an orthogonal basis set $\{\xi_i^O\}$ from $\{\xi_i^B\}$

$$\xi_i^O = \sum_{j=1}^{N} \left(\boldsymbol{S}^{-1/2}\right)_{ij} \xi_j^B, \quad \boldsymbol{S}_{ij} = \langle \xi_i^B | \xi_j^B \rangle. \tag{3-102}$$

The process of Löwdin orthogonalization, to transform a non-orthogonal basis set $\boldsymbol{X}$ to another orthogonal basis set $\boldsymbol{Y}$, employs a symmetric transformation defined by a Hermitian matrix $\boldsymbol{T}$

$$\boldsymbol{Y} = \boldsymbol{X}\boldsymbol{T}. \tag{3-103}$$

And an overlap matrix $\boldsymbol{S}$ has to be defined

$$\boldsymbol{S} = \boldsymbol{X}^\dagger \boldsymbol{X}. \tag{3-104}$$

The target basis set $\boldsymbol{Y}$ is orthogonal, thus

$$\boldsymbol{Y}^\dagger \boldsymbol{Y} = (\boldsymbol{X}\boldsymbol{T})^\dagger \boldsymbol{X}\boldsymbol{T} = \boldsymbol{I} \Rightarrow \boldsymbol{T}^\dagger \boldsymbol{X}^\dagger \boldsymbol{X}\boldsymbol{T} = \boldsymbol{T}^\dagger \boldsymbol{S}\boldsymbol{T} = \boldsymbol{I}. \tag{3-105}$$

Therefore, one obtains

$$\boldsymbol{T} = \boldsymbol{S}^{-1/2} \tag{3-106}$$

because $\boldsymbol{T} = \boldsymbol{T}^\dagger$. The inverse square root of matrix $\boldsymbol{S}$ can be obtained through the standard spectral decomposition method. This explains the mathematical form of equation (3-102).

Now that one has the orthogonal basis set $\{\xi_i^O\}$, the pseudo-wavefunction $\tilde{R}$ can be expanded as

$$\tilde{R}(r) = \begin{cases} \sum_{j=1}^{N} z_j \xi_j^O(r), r \leqslant R_c \\ R^{\mathrm{ae}}(r), \ r > R_c \end{cases} \tag{3-107}$$

where $R^{\mathrm{ae}}(r)$ is the 'hard' all-electron wavefunction. At $r = R_\mathrm{c}$, assuming the zeroth to the (M–1)th derivatives should match between $R^{\mathrm{ae}}(r)$ and $\tilde{R}(r)$, the following M linear equations are introduced as the constraints.

$$\sum_{j=1}^{N} \left(\left. \frac{\mathrm{d}^{i-1} R^{\mathrm{ae}}}{\mathrm{d}r^{i-1}} \right|_{R_c} \right) z_j = \left. \frac{\mathrm{d}^{i-1} R^{\mathrm{ae}}}{\mathrm{d}r^{i-1}} \right|_{R_c} ; i = 1, \cdots, M \tag{3-108}$$

where the jth basis function has its (i–1)th derivative at R_c denoted by

$$\boldsymbol{C}_{ij} = \left. \frac{\mathrm{d}^{i-1} \xi_j^O}{\mathrm{d}r^{i-1}} \right|_{R_\mathrm{c}}. \tag{3-109}$$

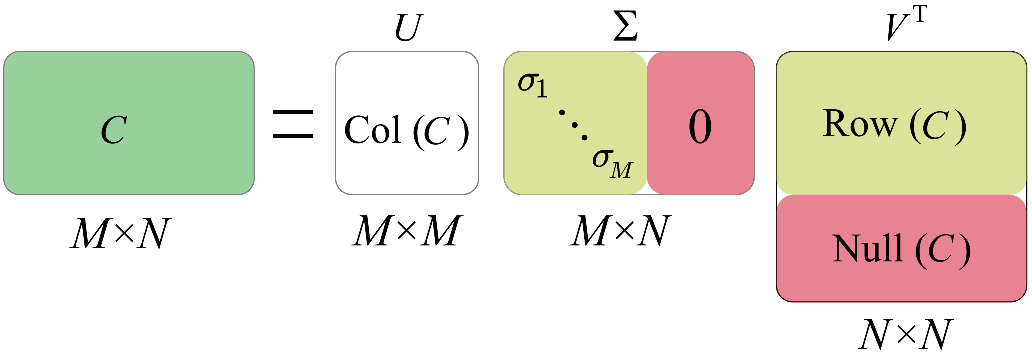

Figure 10. Singular value decomposition regarding the underdetermined matrix $\boldsymbol{C}$ encountered in the ONCV pseudopotential method.

And all $\boldsymbol{C}_{ij}$ values constitute a matrix $\boldsymbol{C}$. In the mean time, the (i–1)th derivative of the all-electron wavefunction at R_c is represented by

$$\boldsymbol{d}_i = \left.\frac{\mathrm{d}^{i-1}R^{\text{ae}}}{\mathrm{d}r^{i-1}}\right|_{R_c} \tag{3-110}$$

which yields a vector $\boldsymbol{d}$. Hence, to derive the coefficients z_j, the governing equations are

$$\begin{array}{c} \boldsymbol{C}_{11}z_1 + \boldsymbol{C}_{12}z_2 + \cdots + \boldsymbol{C}_{1N}z_N = \boldsymbol{d}_1 \\ \boldsymbol{C}_{21}z_1 + \boldsymbol{C}_{22}z_2 + \cdots + \boldsymbol{C}_{2N}z_N = \boldsymbol{d}_2 \\ \cdots \\ \boldsymbol{C}_{M1}z_1 + \boldsymbol{C}_{M2}z_2 + \cdots + \boldsymbol{C}_{MN}z_N = \boldsymbol{d}_M \end{array}. \tag{3-111}$$

The above set of equations is nothing but a compact matrix equation

$$\boldsymbol{C}\boldsymbol{z} = \boldsymbol{d} \tag{3-112}$$

but the dimension of matrix $\boldsymbol{C}$ is $M \times N\,(M < N)$, which is an underdetermined matrix. To obtain the vector $\boldsymbol{z}$, a method named 'singular value decomposition' could be utilized, *i.e.*

$$\boldsymbol{C} = \boldsymbol{U}\boldsymbol{\Sigma}\boldsymbol{V}^\text{T}. \tag{3-113}$$

Here the matrix $\boldsymbol{U}$ is an $M \times M$ orthogonal matrix, the matrix $\boldsymbol{V}$ is an $N \times N$ orthogonal matrix, and $\boldsymbol{\Sigma}$ is an $M \times N$ diagonal matrix (see figure 10). Because the way of singular value decomposition is unique for an underdetermined matrix, a solution can immediately be derived as (note that $\boldsymbol{V}^{-1} = \boldsymbol{V}^\text{T}$ and $\boldsymbol{U}^{-1} = \boldsymbol{U}^\text{T}$ since they are orthogonal matrices)

$$z_0 = \boldsymbol{C}^{-1}\boldsymbol{d} = \boldsymbol{V}\boldsymbol{\Sigma}^{-1}\boldsymbol{U}^\text{T}\boldsymbol{d} \tag{3-114}$$

In this procedure, actually only the first M columns of $\boldsymbol{V}$ (*i.e.* the first M rows of $\boldsymbol{V}^\text{T}$, marked in yellow color in figure 10) matter, because the last N–M columns of $\boldsymbol{\Sigma}$ are zero vectors. The detailed elements of z_0 are

$$(z_0)_i = \sum_{j,k=1}^{M} \boldsymbol{V}_{ij}\left(\boldsymbol{\Sigma}^{-1}\right)_{jj}\left(\boldsymbol{U}^T\right)_{jk}\boldsymbol{d}_k,\ i = 1,\cdots,N. \tag{3-115}$$

We could construct a preliminary pseudo-wavefunction based on this z_0 vector as

$$\tilde{R}_0 = \sum_{i=1}^{N} z_{0i}\xi_i^O \tag{3-116}$$

but it generally fails to satisfy the norm-conserving criterion. To explicitly reflect this distinction, we designate the unmodified variant as $\tilde{R}_0$, reserving the notation $\tilde{R}$ for the fully optimized pseudo-wavefunction that only appears later. The transition from $\tilde{R}_0$ to $\tilde{R}$ necessitates a refinement procedure that not only enforces the norm conservation condition, but concurrently achieves the ancillary benefit of residual kinetic energy minimization.

The last N–M columns of matrix $\boldsymbol{V}$ consists of vectors z_j^Null (corresponding to the last N–M rows of $\boldsymbol{V}^\text{T}$, the red part of figure 10) that satisfy $\boldsymbol{C}z_j^\text{Null} = \boldsymbol{0}$. This implies that if z_0 is converted to another vector $z_0 + z_j^\text{Null}$, it still satisfies the equation $\boldsymbol{C}\left(z_0 + z_j^\text{Null}\right) = \boldsymbol{d}$. Specifically, adding any z_j^Null to the solution z_0 does not alter the zeroth to $(M{-}1)^\text{th}$ order derivative matching conditions. The set of vectors z_j^Null is named the null space of matrix $\boldsymbol{C}$, denoted by $\text{Null}\,(\boldsymbol{C})$. A linear combination of z_j^Null could yield an optimal result z_y such that the final solution $z_0 + z_y$ enables the norm conservation condition and minimizes the residual kinetic energy.

It is high time to formally bridge the ONCV and RRKJ frameworks. The wavefunction $\tilde{R}_0$ as determined by the unique solution z_0 in the ONCV method, corresponds to $F(r)$ in the RRKJ method. Moreover, $\text{Null}\,(\boldsymbol{C})$ is like a basis set for $C(r)$, both of which are utilized to minimize the residual kinetic energy. Hamann has combined the $F(r)$ and $C(r)$ parts of RRKJ into a compact matrix form. Furthermore, the ONCV method allows for derivative matching up to a desired order. The choice of M is typically greater than 3 in the ONCV method, with the reason explained as follows. When a pseudo-wavefunction is designed, the Schrödinger equation has to be inversely solved to yield the pseudopotential for angular quantum number l. In equation (3-32), one should take the second derivative of the pseudo-wavefunction, which corresponds to $M = 2 + 1 = 3$. This is merely the minimal value of M. For applications like DFPT, one needs to take the second derivative of the pseudopotential, thus M should be set to an even larger value.

The RRKJ method adjusts the coefficients β_i of $C(r)$, to minimize the residual kinetic energy with the constraints of continuous derivatives up to the second order, in addition to the norm conservation condition. On the contrary, Hamann utilizes $\mathrm{Null}(\boldsymbol{C})$ to minimize the residual kinetic energy, which has the benefit that only the norm-conserving constraint matters. This is because vectors from $\mathrm{Null}(\boldsymbol{C})$ all satisfy the criterion $\boldsymbol{C}z_j^{\mathrm{Null}}=0$. Hence, using z_j^{Null} to construct the '$C(r)$' part, automatically conserves the zeroth to (N–1)th derivative matching between the final $\tilde{\Phi}$ and the all-electron wavefunction Φ. Removing certain constraints in the searching could render a more optimized pseudo-wavefunction product.

Therefore, the exact process of optimizing the residual kinetic energy using $\mathrm{Null}(\boldsymbol{C})$ has to be elaborated in detail. Apparently, all vectors in $\mathrm{Null}(\boldsymbol{C})$ are annihilated during the matrix operation $\boldsymbol{\Sigma}\boldsymbol{V}^{\mathrm{T}}$, thus $\mathrm{Null}(\boldsymbol{C})$ has no impact upon $\boldsymbol{C}$ at all. And the matrix $\boldsymbol{C}$ in the ONCV method is not only the '$F(r)$' part, but it has a full column dimension of N. It seems as if $\mathrm{Null}(\boldsymbol{C})$ cannot exert a direct influence in our optimization, but in fact $\mathrm{Null}(\boldsymbol{C})$ inspires us how to optimize the residual kinetic energy in an indirect manner, as formalized below. Any vector z_j^{Null} in $\mathrm{Null}(\boldsymbol{C})$ contains a series of coefficients, which act on the basis set ξ_i^O to generate a wavefunction. A definite linear combination of many z_j^{Null} also corresponds to a wavefunction. This wavefunction, when added to $\tilde{R}_0$, does not alter its well-established conditions of derivative matching. Hence, the best wavefunction corresponds to the $C(r)$ part in the RRKJ method. Through singular value decomposition, one has directly obtained a basis set for $\mathrm{Null}(\boldsymbol{C})$, named $\left\{\xi_i^N\right\}$, which consists of the (M+1)th to the Nth columns of $\boldsymbol{V}$. In other words, $C(r)$ is a linear combination of $\left\{\xi_i^N\right\}$, and it is only the expansion coefficients before ξ_i^N that are subject to optimization, for the sake of residual kinetic energy minimization.

To illustrate the basic mathematics of this procedure, an intentionally simplified example can be very useful. Suppose one has a 2×3 underdetermined matrix

$$\boldsymbol{C}=\frac{1}{14}\begin{bmatrix}4 & -15 & -2\\ -4 & 15 & 2\end{bmatrix}. \tag{3-117}$$

And the vector

$$\boldsymbol{d}=\begin{bmatrix}0.5\\ 1\end{bmatrix}. \tag{3-118}$$

The singular value decomposition $\boldsymbol{C}=\boldsymbol{U}\boldsymbol{\Sigma}\boldsymbol{V}^{\mathrm{T}}$ yields

$$\boldsymbol{U}=\frac{1}{2}\begin{bmatrix}-1 & 1\\ 1 & -1\end{bmatrix};\boldsymbol{\Sigma}=\begin{bmatrix}1 & 0 & 0\\ 0 & 2 & 0\end{bmatrix};$$
$$\boldsymbol{V}^{\mathrm{T}}=\frac{1}{7}\begin{bmatrix}2 & 3 & 6\\ 3 & -6 & 2\\ 6 & 2 & -3\end{bmatrix}. \tag{3-119}$$

The unique solution for $\boldsymbol{C}\boldsymbol{z}=\boldsymbol{d}$ is

$$z_0=\boldsymbol{V}\boldsymbol{\Sigma}^{-1}\boldsymbol{U}^T\boldsymbol{d}=\begin{bmatrix}\frac{1}{56} & \frac{3}{14} & \frac{5}{28}\end{bmatrix}^T \tag{3-120}$$

which sets up a wavefunction

$$\tilde{R}_0(r)=\frac{1}{56}\xi_1^O(r)+\frac{3}{14}\xi_2^O(r)+\frac{5}{28}\xi_3^O(r). \tag{3-121}$$

There is no guarantee that $\tilde{R}_0$ should be norm-conserving, because such constraint has never been imposed yet. It turns out that the third column of matrix $\boldsymbol{\Sigma}$ is a zero vector, thus the third row of $\boldsymbol{V}^{\mathrm{T}}$ exerts no influence on the solution space of the linear system $\boldsymbol{C}\boldsymbol{z}=\boldsymbol{d}$. Hence, there is one vector in $\mathrm{Null}(\boldsymbol{C})$ identified as

$$\xi_1^N(r)=\frac{6}{7}\xi_1^O(r)+\frac{2}{7}\xi_2^O(r)-\frac{3}{7}\xi_3^O(r). \tag{3-122}$$

Since the initial matrix is too small in dimension, one only obtains a single ξ_i^N, meaning that $\mathrm{Null}(\boldsymbol{C})$ is one dimensional. The sole functionality of this $\xi_1^N(r)$ is thus, it should be multiplied by a proper factor y_1, such that the resulting pseudo-wavefunction

$$\tilde{R}(r)=\tilde{R}_0(r)+y_1\xi_1^N(r) \tag{3-123}$$

is overall norm-conserving. There is no scope to reduce the residual kinetic energy. However, one may choose an even larger initial matrix $\boldsymbol{C}$, e.g. 2×4 or 2×5. Then $\mathrm{Null}(\boldsymbol{C})$ will involve several bases, and besides the norm conserving constraint, there is some scope to optimize the expansion coefficients y_j, in order to minimize the residual kinetic energy.

The default example in the RRKJ paper [100] could be translated into the ONCV language as follows. It involves nine spherical Bessel functions in total, corresponding to nine basis functions of the ONCV method. Four out of the nine basis functions constitute a unique solution ($\tilde{R}_0$), and the other five basis functions span $\mathrm{Null}(\boldsymbol{C})$. The optimization process is searching for a vector in this five-dimensional space, with which one can construct $C(r)$, minimizing the residual kinetic energy while keeping the norm-conserving condition for $\tilde{R}(r)$. On the other hand, one could directly use nine basis functions following the ONCV approach. To consistently ensure the derivative matching from zeroth order to second order, as in the RRKJ method, the ONCV method first consumes a 3D subspace, out of the overall 9D solution space. The singular value decomposition yields a unique solution z_0 within this 3D subspace, which is used to construct $\tilde{R}_0$. The meaning of $\tilde{R}_0$ is similar to $F(r)$ in the RRKJ approach, but there are differences. The $F(r)$ wavefunction in RRKJ has to satisfy the norm-conserving condition, which is in fact unnecessary. This is because only the final optimized pseudo-wavefunction matters, when it comes to the norm-conserving criterion. The ONCV method no longer has such restriction, thus it permits more scope for optimization. In this example, the ONCV method involves six ξ_i^N functions for residual kinetic energy minimization. In contrast, the RRKJ method only has five spherical Bessel functions to yield the optimized $C(r)$.

The trick of the ONCV method, in gaining more scope of kinetic energy minimization, lies in an optimization within a subspace $\mathrm{Null}(\boldsymbol{C})$. Although the basis functions of $\mathrm{Null}(\boldsymbol{C})$, $\left\{\xi_i^N\right\}$, are already available after singular value decomposition, it deserves to establish their relation to $\left\{\xi_i^O\right\}$. Note that

Null$(\boldsymbol{C})$ is only a subspace of the entire solution space, thus ξ_i^O in general cannot be expressed in terms of ξ_i^N, but the converse expansion is mathematically admissible. Specifically, any subspace vector has a representation through the complete basis set of the entire space, via a linear transformation as follows

$$\xi_i^N = \sum_{j=1}^{N} \boldsymbol{V}_{j,M+i} \xi_j^O,\ i = 1,\ 2,\ \cdots,\ N-M. \tag{3-124}$$

Here $\boldsymbol{V}$ is nothing but the familiar matrix in figure 10 (the figure in fact shows its transpose $\boldsymbol{V}^{\mathrm{T}}$). With the basis set $\left\{\xi_i^N\right\}$ at hand, one constructs

$$\tilde{R}_N(r) = \sum_{j=1}^{N-M} y_j \xi_j^N(r) \tag{3-125}$$

which is the '$C(r)$' part, consisting of a linear combination of *N–M* basis functions within Null$(\boldsymbol{C})$. The *N–M* expansion coefficients (y_j) are subject to optimization, which is ready to be solved using the Lagrange multiplier technique.

Now we digress into a remaining question, regarding the choice of q_i values in the ONCV method. It should be emphasized that each basis function ξ_i^B is uniquely characterized by its corresponding q_i value, given the angular momentum quantum number l and the corresponding cutoff radius R_{c}. Provided that one requires all ξ_i^B to satisfy the logarithmic derivative matching condition at $r = R_{\mathrm{c}}$, and selects the first N values in such a set of q_i, would the resulting spherical Bessel functions $j_l(q_i r)$ directly give the orthogonal basis set $\left\{\xi_i^O\right\}$? Unfortunately, the situation is not as simple. As-constructed $j_l(q_i r)$ functions are part of the solutions to the spherical equation under the homogeneous Robin boundary condition at $r = R_{\mathrm{c}}$, because the logarithmic derivative matching condition imposes a numerical constraint between the wavefunction and its first derivative at the boundary, with reference to the all-electron wavefunction. If all basis functions are such chosen, their linear combination as $\tilde{R}_0$ must also obey the same logarithmic derivative matching condition. This renders identical meaning in the two constraints $\mathcal{C}_1$ and $\mathcal{C}_2$. In the ONCV language, the rank of matrix $\boldsymbol{C}$ will consequently be reduced from *M* to *M–1*. The solution out of such dilemma is to introduce other q values, whose corresponding wavefunctions $j_l(qr)$ do not satisfy the same Robin boundary condition at $r = R_{\mathrm{c}}$. The scheme prescribed by Hamann involves partitioning the q values into complementary subsets. The even-indexed subset $\{q_2, q_4, q_6, \cdots\}$ strictly satisfies the prescribed boundary condition, while the odd-indexed subset $\{q_1, q_3, q_5, \cdots\}$ is algorithmically generated through linear interpolation, *i.e.* $q_1 = q_2/2$, $q_3 = (q_2 + q_4)/2$, and so forth. This resolves the matrix rank degradation problem, at the cost of sacrificing orthogonality in the resultant basis set $\left\{\xi_i^B\right\}$. An additional orthogonalization process is therefore mandatory to convert $\left\{\xi_i^B\right\}$ into $\left\{\xi_i^O\right\}$.

The story of ONCV method is not yet over, because (i) one is inclined to using multiple reference energy values for the transferability of the pseudopotential; (ii) Hamann proposed a more robust approach to minimize the residual kinetic energy, other than the conventional Lagrange multiplier method. The latter point will be reviewed first. To begin with, we finish the formal expression for the optimized (single) pseudo-wavefunction

$$\tilde{R}(r) = \tilde{R}_0(r) + \tilde{R}_N(r) = \tilde{R}_0(r) + \sum_{j=1}^{N-M} y_j \xi_j^N(r),\ r \leqslant R_{\mathrm{c}} \tag{3-126}$$

then the residual kinetic energy is, written in terms of the operator $\hat{E}^r$ and Dirac notation,

$$E^r = \left\langle \tilde{R}_0 \middle| \hat{E}_r \middle| \tilde{R}_0 \right\rangle + 2\sum_{j=1}^{N-M} y_j \left\langle \xi_j^N \middle| \hat{E}^r \middle| \tilde{R}_0 \right\rangle + \sum_{j,k=1}^{N-M} y_j y_k \left\langle \xi_j^N \middle| \hat{E}^r \middle| \xi_k^N \right\rangle. \tag{3-127}$$

The operator $\hat{E}^r$ is explained as follows. For any spherical function $R_{l,i}(r)$, its radial Fourier transform yields

$$R_{l,i}(q) = 4\pi \int_0^{\infty} \mathrm{d}r\, r^2 j_l(qr) R_{l,i}(r) \tag{3-128}$$

where j_l is spherical Bessel function of the lth order. This expression may be understood according to the Rayleigh formula equation (3-39). Given a function $g_{lm}(\boldsymbol{r})$ that can be written in a variable-separated form $g_{lm}(\boldsymbol{r}) = R_l(r) Y_{lm}(\theta_r, \varphi_r)$, its full Fourier transform is

$$\begin{aligned}
\mathcal{F}\{g_{lm}(\boldsymbol{r})\} &= \int \mathrm{d}\boldsymbol{r}\, g_{lm}(\boldsymbol{r}) \mathrm{e}^{-i\boldsymbol{k}\cdot\boldsymbol{r}} \\
&= \int_0^{\infty} r^2 \mathrm{d}r \int_0^{\pi} \sin\theta_r \mathrm{d}\theta_r \int_0^{2\pi} \mathrm{d}\varphi_r\, R_l(r) Y_{lm}(\theta_r, \varphi_r) \\
&\quad \times 4\pi \sum_{l',m'} (-i)^{l'} j_{l'}(kr) Y_{l'm'}^*(\theta_k, \varphi_k) Y_{l'm'}(\theta_r, \varphi_r) \\
&= 4\pi \sum_{l',m'} (-i)^{l'} Y_{l'm'}^*(\theta_k, \varphi_k) \left[\int_0^{\infty} R_l(r) j_{l'}(kr) r^2 \mathrm{d}r\right] \\
&\quad \times \left[\int_{\theta_r=0}^{\pi} \int_{\varphi_r=0}^{2\pi} Y_{lm}(\theta_r, \varphi_r) Y_{l'm'}(\theta_r, \varphi_r) \sin\theta_r \mathrm{d}\theta_r \mathrm{d}\varphi_r\right].
\end{aligned} \tag{3-129}$$

For the angular part, using a property of spherical harmonics $Y_{lm}(\theta, \varphi) = (-1)^m Y_{l,-m}^*(\theta, \varphi)$, one has

$$\begin{aligned}
&Y_{l'm'}^*(\theta_k, \varphi_k) \int_0^{\pi} \int_0^{2\pi} Y_{lm}(\theta_r, \varphi_r) Y_{l'm'}(\theta_r, \varphi_r) \sin\theta_r \mathrm{d}\theta_r \mathrm{d}\varphi_r \\
&\quad = (-1)^{m'} Y_{l'm'}^*(\theta_k, \varphi_k) \delta_{ll'} \delta_{m,-m'} = Y_{l',-m'}(\theta_k, \varphi_k) \delta_{ll'} \delta_{m,-m'}.
\end{aligned} \tag{3-130}$$

With this relation, the Fourier transform of $g_{lm}(\boldsymbol{r})$ becomes

$$\mathcal{F}\{g_{lm}(\boldsymbol{r})\} = \left[4\pi \int_0^{\infty} R_l(r) j_l(kr) r^2 \mathrm{d}r\right] (-i)^l Y_{lm}(\theta_k, \varphi_k) \tag{3-131}$$

among which the part enclosed in square brackets is the radial Fourier transform, and the rest is the angular part.

The residual kinetic energy operator is such defined that

$$\langle R_{l,i}\left|\hat{E^r}(q_c)\right|R_{l,j}\rangle = \int_{q_c}^{\infty} R_{l,i}(q)\,R_{l,j}(q)\,\frac{q^4}{4}\mathrm{d}q \tag{3-132}$$

and it depends on the choice of q_c.

The operator $\hat{E^r}$ appears in all three terms of the expression equation (3-127). The second term comes from the crossing between $\tilde{R}_0$ and $\tilde{R}_N$. On the other hand, since $\tilde{R}_0$ can be expanded in terms of ξ_i^O such that

$$\tilde{R}(r) = \sum_{i=1}^{N}(z_0)_i\xi_i^O(r) + \sum_{j=1}^{N-M} y_j\xi_j^N(r),\; r \leqslant R_\mathrm{c} \tag{3-133}$$

and both ξ_i^O and ξ_j^N are normalized bases, the norm-conserving condition requires that

$$\sum_{i=1}^{N}\left[(z_0)_i\right]^2 + \sum_{j=1}^{N-M} y_j^2 = \langle R^{\mathrm{ae}}|R^{\mathrm{ae}}\rangle_{R_c}. \tag{3-134}$$

Note that the values of $(z_0)_i$ are fixed because the singular value decomposition is unique. Only the y_j coefficients are subject to adjustment to ensure the norm conservation. Working within Null$(\boldsymbol{C})$, the key criterion for norm conservation is no longer $\langle R^{\mathrm{ae}}|R^{\mathrm{ae}}\rangle_{R_c}$, but a 'norm deficit' term D_{norm}, defined as

$$D_{\mathrm{norm}} = \sum_{j=1}^{N-M} y_j^2 = \langle R^{\mathrm{ae}}|R^{\mathrm{ae}}\rangle_{R_c} - \sum_{i=1}^{N}\left[(z_0)_i\right]^2. \tag{3-135}$$

Hamann adopts a more robust approach to solve this constrained optimization problem [83]. The matrix element of $\hat{E^r}$ is

$$\boldsymbol{E}_{ij}^r = \left\langle \xi_i^N\middle|\hat{E^r}\middle|\xi_j^N\right\rangle. \tag{3-136}$$

Through diagonalizing the $\boldsymbol{E}^r$ matrix, one obtains the eigenvectors of $\boldsymbol{E}^r$. Each eigenvector of $\boldsymbol{E}^r$ within the $(N–M) \times (N–M)$ subspace Null$(\boldsymbol{C})$ has $N–M$ elements, which are the expansion coefficients ahead of ξ_j^N for $j = 1, 2, \ldots, N-M$. Let the $N–M$ elements of the first eigenvector be $a_1, a_2, \cdots, a_{N-M}$, then one constructs a new basis function

$$\xi_1^R(r) = a_1\xi_1^N(r) + a_2\xi_2^N(r) + \cdots + a_{N-M}\xi_{N-M}^N(r). \tag{3-137}$$

List the $N–M$ elements of the second eigenvector as $b_1, b_2, \cdots, b_{N-M}$, then in the same way one arrives at

$$\xi_2^R(r) = b_1\xi_1^N(r) + b_2\xi_2^N(r) + \cdots + b_{N-M}\xi_{N-M}^N(r). \tag{3-138}$$

In total, $N–M$ basis functions could be constructed, to yield the fourth basis set $\left\{\xi_i^R\right\}$, named the residual basis functions. This process is nothing but a representation transformation within an $(N–M) \times (N–M)$ Hilbert space. The vector $[a_1,\, a_2, \ldots,\, a_{N-M}]^{\mathrm{T}}$ is in fact the explicit form of ξ_1^R, under a working representation (which must be known in advance!) that utilizes $\left\{\xi_i^R\right\}$ as its basis set. The distinction between $\left\{\xi_i^N\right\}$ and $\left\{\xi_i^R\right\}$ lies in that, the operator $\hat{E^r}$ is represented as a diagonal matrix in the representation of the latter, but not in the representation of the former. Hence, the representation transformation towards $\left\{\xi_i^R\right\}$ aims at finding the own representation of $\hat{E^r}$, facilitating the expression of the last term of the residual kinetic energy, *i.e.*

$$\left\langle \xi_i^R\middle|\hat{E^r}\middle|\xi_j^R\right\rangle = e_j\langle\xi_i^R|\xi_j^R\rangle = e_j\delta_{ij} \tag{3-139}$$

where e_j is the jth eigenvalue of $\hat{E^r}$. Now there are as many as four basis sets $\left\{\xi_i^B\right\}$, $\left\{\xi_i^O\right\}$, $\left\{\xi_i^N\right\}$ and $\left\{\xi_i^R\right\}$ in the ONCV method, but they demonstrate distinct functional hierarchies. $\left\{\xi_i^N\right\}$ and $\left\{\xi_i^R\right\}$ are merely the basis sets for Null$(\boldsymbol{C})$, whereas $\left\{\xi_i^B\right\}$, $\left\{\xi_i^O\right\}$ are for the entire solution space, and $\left\{\xi_i^B\right\}$ is in fact not orthogonal.

Using the new basis set $\left\{\xi_i^R\right\}$, the pseudo-wavefunction is rephrased as

$$\tilde{R} = \tilde{R}_0 + \sum_{i=1}^{N-M} x_i\xi_i^R. \tag{3-140}$$

with x_i being the coefficients subject to optimization. And the residual kinetic energy has a simpler expression

$$\begin{aligned} E^r &= \langle\tilde{R}_0|\hat{E^r}|\tilde{R}_0\rangle + 2\sum_{i=1}^{N-M} x_i\left\langle\xi_i^R|\hat{E^r}|\tilde{R}_0\right\rangle + \sum_{i,j=1}^{N-M} x_ix_j\left\langle\xi_i^R|\hat{E^r}|\xi_j^R\right\rangle \\ &= \langle\tilde{R}_0|\hat{E^r}|\tilde{R}_0\rangle + 2\sum_{i=1}^{N-M} e_i\left\langle\xi_i^R\middle|\tilde{R}_0\right\rangle x_i + \sum_{i,j=1}^{N-M} x_ix_je_j\delta_{ij} \\ &= \langle\tilde{R}_0|\hat{E^r}|\tilde{R}_0\rangle + \sum_{i=1}^{N-M}\left(2f_ix_i + e_ix_i^2\right) \end{aligned} \tag{3-141}$$

where e_i is the eigenvalue of $\hat{E^r}$ and a shorthand symbol f_i has been introduced

$$f_i = \left\langle\xi_i^R\middle|\hat{E^r}\middle|\tilde{R}_0\right\rangle = e_i\langle\xi_i^R|\tilde{R}_0\rangle. \tag{3-142}$$

The final form of E^r is both concise and clear. The term $\left\langle\tilde{R}_0\middle|\hat{E^r}\middle|\tilde{R}_0\right\rangle$ should be treated as a constant since it cannot be updated by any optimization operation within Null$(\boldsymbol{C})$. Hence, only the sum $2f_ix_i + e_ix_i^2$ is subject to minimization, and the coefficients x_i are exactly the quantities to be optimized.

To proceed, Hamann introduced an iterative method instead of using Lagrange multipliers. The x_i coefficients could be fixed through iteration until convergence. Using the new $\left\{\xi_i^R\right\}$ basis set, the norm-conserving condition for $\tilde{R}$ is, as modified from (3-135),

$$x_1^2 = D_{\mathrm{norm}} - \sum_{i=2}^{N-M} x_i^2 \tag{3-143}$$

where we have intentionally separated out x_1^2. Supposing $x_2, \cdots, x_{N-M}$ are already known or have been randomly initialized, a formula is prescribed for x_1 as, straightforwardly from equation (3-143),

$$x_1 = s\sqrt{D_{\text{norm}} - \sum_{i=2}^{N-M} x_i^2} \tag{3-144}$$

where

$$s = \pm 1. \tag{3-145}$$

After obtaining x_1, it is possible to differentiate the residual kinetic energy with respect to other x_i, and the stationary point condition yields the values of x_i. Take x_2 as an example, noting that

$$\begin{aligned} E^r = {} & \left\langle \tilde{R}_0 \middle| \hat{E}^r \middle| \tilde{R}_0 \right\rangle + 2f_1x_1 + e_1x_1^2 \\ & + 2f_2x_2 + e_2x_2^2 + \sum_{i=3}^{N-M} \left(2f_ix_i + e_ix_i^2\right). \end{aligned} \tag{3-146}$$

One of the necessary conditions for reaching a minimal E^r value is

$$\frac{\partial E^r}{\partial x_2} = 0. \tag{3-147}$$

Because x_1 is regarded as 'yet to be determined' through the iterative formula (3-144), x_1 depends on x_2 in this scheme. Other coefficients $x_3, x_4, \cdots$ are however independent with respect to x_2. Hence,

$$\frac{\partial E^r}{\partial x_2} = 2f_1\left(\frac{\partial x_1}{\partial x_2}\right) + 2e_1x_1\left(\frac{\partial x_1}{\partial x_2}\right) + 2f_2 + 2e_2x_2. \tag{3-148}$$

Note that

$$\begin{aligned} \frac{\partial x_1}{\partial x_2} &= \frac{\partial}{\partial x_2}\left(s\sqrt{D_{\text{norm}} - \sum_{i=2}^{N-M} x_i^2}\right) \\ &= \frac{s}{2}\left(D_{\text{norm}} - \sum_{i=2}^{N-M} x_i^2\right)^{-\frac{1}{2}} (-2x_2) = -s^2\frac{x_2}{x_1} = -\frac{x_2}{x_1} \end{aligned} \tag{3-149}$$

therefore

$$\frac{\partial E^r}{\partial x_2} = 2\left(f_1 + e_1x_1\right)\left(-\frac{x_2}{x_1}\right) + 2\left(f_2 + e_2x_2\right) = 0 \tag{3-150}$$

which yields

$$x_2 = \frac{f_2x_1}{e_1x_1 - e_2x_1 + f_1}. \tag{3-151}$$

A generalization to $x_3, x_4, \cdots$ gives

$$x_i = -\frac{f_i}{e_i - e_1 - f_1/x_1}, i > 1. \tag{3-152}$$

Hence, equation (3-152) could be used to calculate all other coefficients x_i. This terminates an iterative cycle. During the next cycle, these x_i $(i > 1)$ values are used to update x_1 through equation (3-144), and such cycles continue until all coefficients are self-consistent, ultimately completing the optimization process.

The last remaining issue is regarding the value of s in the expression for x_1. It was pointed out by Hamann, in a later erratum paper [102], that the sign of s should be opposite to that of f_1. A simple explanation is given as follows. The part of E^r that could be minimized is

$$\begin{aligned} & \left(e_1x_1^2 + 2f_1x_1\right) + \left(e_2x_2^2 + 2f_2x_2\right) \\ & \quad + \cdots + \left(e_{N-M}x_{N-M}^2 + 2f_{N-M}x_{N-M}\right) \end{aligned} \tag{3-153}$$

as divided into *N*–*M* segments. A viable strategy involves systematically minimizing each segment containing coefficient x_i within the expression. The eigenvalues of the residual kinetic energy operator $\hat{E}^r$ must be positive, *i.e.* $e_i > 0$. Now that the quadratic function $e_ix_i^2 + 2f_ix_i$ has a minimal value at

$$x_i^m = -\frac{2f_i}{2e_i} = -\frac{f_i}{e_i} \tag{3-154}$$

the optimal x_i must share the same sign as x_i^m. Hence, x_i and f_i possess opposite signs, valid for all $i \in [1, N-M]$. A self-consistency validation is conveniently given as follows. Note that for $i > 1$,

$$\operatorname{sgn}\left(x_i\right) = \operatorname{sgn}\left[-\frac{f_i}{\left(e_i - e_1\right) - \frac{f_1}{x_1}}\right] = -\operatorname{sgn}\left(f_i\right). \tag{3-155}$$

The reasons lies in that e_i $(i > 1)$ is a greater eigenvalue compared with e_1, and f_1/x_1 is negative as a provided condition. To sum up, s takes the value of -1 when f_1 is positive, and $s = 1$ should be used given that f_1 is negative. The value of $f_1 = e_1\left\langle \xi_1^R \middle| \tilde{R}_0 \right\rangle$ is a known constant prior to the optimization process, thus the value of s is also pre-determined before the iteration starts.

The above algorithm can be implemented to generate one optimized pseudo-wavefunction. Nevertheless, as mentioned earlier, the ONCV method simultaneously incorporates multiple reference energies, and therefore the pseudopotential is generated from several pseudo-wavefunctions. In particular, Hamann selects two reference energies, thus only two projectors are used for each *l* value in the default ONCV method, with reference eigenfunctions R_1^{ae} and R_2^{ae}. Within the cutoff radius, R_2^{ae} should possess one more node than R_1^{ae}, as pointed out by Hamann. Suppose the basis set $\left\{\xi_i^O\right\}$ has been used to generate $\tilde{R}_1$, then $\left\{\xi_i^O\right\}$ can still be suitable for $\tilde{R}_2$, provided that an additional generalized norm-conserving condition is respected. This new condition is expressed as follows.

$$\begin{aligned} \left\langle \tilde{R}_1 \middle| \tilde{R}_2 \right\rangle_{R_c} &= z_{1,1}z_{2,1}\left\langle \xi_1^O \middle| \xi_1^O \right\rangle + z_{1,2}z_{2,2}\left\langle \xi_2^O \middle| \xi_2^O \right\rangle \\ & \quad + \cdots + z_{1,N}z_{2,N}\left\langle \xi_1^O \middle| \xi_1^O \right\rangle \\ &= \sum_{i=1}^{N} z_{1,i}z_{2,i} = \langle R_1^{\text{ae}} | R_2^{\text{ae}} \rangle_{R_c} \end{aligned} \tag{3-156}$$

where $z_{1,i}$ are the expansion coefficients when $\tilde{R}_1$ is expressed in terms of the basis set $\left\{\xi_i^O\right\}$, and $z_{2,i}$ are the desired

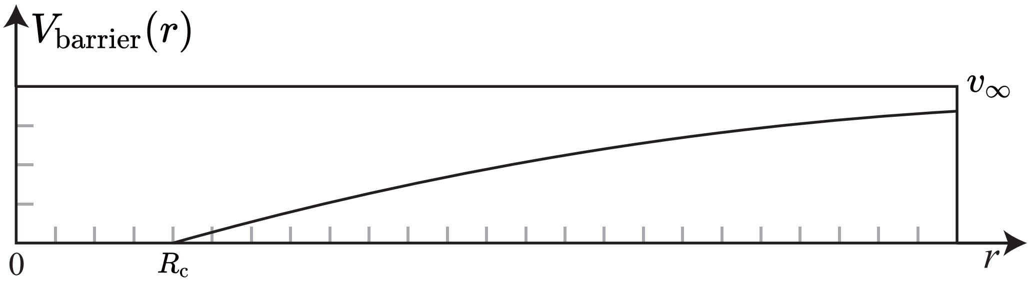

Figure 11. An illustration of a typical barrier potential $V_{\mathrm{barrier}}(r)$.

expansion coefficients of $\tilde{R}_2$. The quantity $\langle R_1^{\mathrm{ae}} | R_2^{\mathrm{ae}} \rangle_{R_\mathrm{c}}$ is available through previous all-electron calculations. The necessity of such generalized norm-conserving condition has been established by Vanderbilt (cf section 3.4).

The matrix $\boldsymbol{B}$, introduced by Vanderbilt with elements $\boldsymbol{B}_{ij} = \left\langle \tilde{\Phi}_i \middle| \chi_{lm,j} \right\rangle$ (cf section 3.3), has been further simplified in the ONCV work. The matrix is diagonalized to obtain its eigenvalues and eigenvectors. Under the default ONCV settings, $\boldsymbol{B}$ is a 2×2 matrix because each l value only corresponds to two reference energies. Now a new projector function $|\tilde{\chi}_{lm,i}\rangle$ is introduced, through a proper linear combination from the eigenvectors of $\boldsymbol{B}$ and $|\chi_{lm,i}\rangle$, in order that $\left\langle \tilde{\Phi}_i \middle| \tilde{\chi}_{lm,j} \right\rangle$ is non-zero only when $i = j$. Let $\tilde{b}_{l,i}$ denote the reciprocals of $\left\langle \tilde{\Phi}_i \middle| \tilde{\chi}_{lm,i} \right\rangle$, then

$$\left\langle \tilde{\Phi}_i \middle| \tilde{\chi}_{lm,j} \right\rangle = \frac{1}{\tilde{b}_{l,i}} \delta_{ij}. \tag{3-157}$$

The non-local part pseudopotential operator is accordingly simplified as

$$\widehat{V}_{\mathrm{NL}} = \sum_{l,m} \sum_{i} |\tilde{\chi}_{lm,i}\rangle \frac{1}{\tilde{b}_{l,i}} \langle \tilde{\chi}_{lm,i}| . \tag{3-158}$$

The δ_{ij} factor has reduced the double sum over i, j in equation (3-54) to a single sum over i, greatly facilitating the practical implementation.

Another advancement in the ONCV method lies in its ability to handle anion states during reference energy selection. Indeed, for a cation, all electrons are still in bound states, but in an anion this leads to positive eigenvalues and scattering states. Hence, Hamann introduces a barrier potential (a typical example is given in figure 11) that is supplemented to the all-electron potential, yielding

$$V_{\mathrm{AEB}}(r) = V_{\mathrm{AE}}(r) + V_{\mathrm{barrier}}(r), \text{ where} \begin{cases} V_{\mathrm{barrier}}(r) = v_\infty \Theta(x) \frac{x^3}{1+x^3} \\ x = (r - R_\mathrm{c})/R_\mathrm{b} \end{cases} \tag{3-159}$$

In equation (3-159), $\Theta(x)$ is the unit step function, v_∞ is the barrier height, and R_b stands for the increasing rate of the barrier. The barrier potential is zero at R_c, and its first and second derivatives are also zero there. With the assistance of the barrier potential, the scattering states could be suppressed. Such strategy is particular useful for, say, generating the $l = 2$ pseudopotential for those elements without d electrons in their atoms.

4. Solving the Hamiltonian

According to the famous Hohenberg–Kohn theorems [32], the ground state electron density has a one-to-one correspondence to the external potential (except for a trivial additive constant), thus the iterative process to solve the Hamiltonian can be established as follows. An initial guess for the ground state electron density should be carried out first. The electron density corresponds to an external potential and thus the one-electron Hamiltonian can be fixed. The diagonalization of the Hamiltonian yields the one-electron eigenstates and energy eigenvalues, which cover a certain energy range. The occupied electron eigenstates are further used to generate the ground state electron density, which typically differs from the one just used. Therefore, a new iterative process begins, which proceeds over and over again, until the electron densities before and after this process agree well within a stringent error range.

Under DFT and the Kohn–Sham framework, the total energy functional is written as

$$E_{\mathrm{total}}[n] = T_s[n] + E_{\mathrm{Hartree}}[n] + E_{\mathrm{XC}}[n] + E_{\mathrm{Ie}}[n] + E_{\mathrm{II}} \tag{4-1}$$

where T_s is the kinetic energy functional for the Kohn-Sham auxiliary system, E_{Hartree} is the classical Coulomb interaction energy between electrons, E_{XC} is the exchange-correlation functional, and E_{Ie} is the interaction energy between electrons and ions, where only those valence electrons and ion cores are considered as far as a pseudopotential calculation is concerned. The last term E_{II} characterizes the Coulomb interaction energy between ions, which is independent of the electron density and should be a constant provided that the ionic positions are fixed.

The total energy functional leads to the one-electron Kohn–Sham equation

$$\widehat{H}_{\mathrm{KS}} \psi_{n,\boldsymbol{k}}(\boldsymbol{r}) = \left[\widehat{T}_s + \widehat{V}_{\mathrm{Hartree}} + \widehat{V}_{\mathrm{XC}} + \widehat{V}^{\mathrm{ps}}\right] \psi_{n,\boldsymbol{k}}(\boldsymbol{r}) = \varepsilon_{n,\boldsymbol{k}} \psi_{n,\boldsymbol{k}}(\boldsymbol{r}). \tag{4-2}$$

Within the Hamiltonian, the first term is the kinetic energy operator; the second term is the Hartree potential that describes

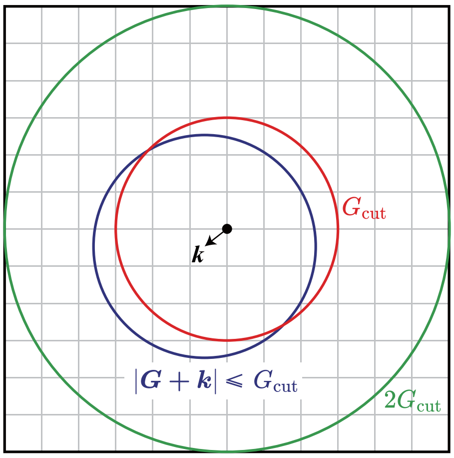

Figure 12. A schematic illustration for the plane waves enclosed by $|\boldsymbol{k}+\boldsymbol{G}| \leqslant G_{\rm cut}$ in the reciprocal space, with the $\boldsymbol{k}$ point not lying at the zone center. The plane waves enclosed by $|\boldsymbol{G}| \leqslant 2G_{\rm cut}$ are employed for the Fourier transforms of quantities such as the electron density.

the Coulomb interaction between electrons as pure charge carriers; the following term is the exchange-correlation potential; the last term is the ion-electron interaction term. Solving the Kohn-Sham equation requires the choice of a proper basis set to expand the electronic wavefunctions.

4.1. Plane-wave basis

Although a mathematically complete plane wave basis set involves an infinite number of plane waves, those components with extremely high kinetic energies typically have little contribution in the expansion. The most common approach is to set a cutoff energy $E_{\rm cut}$ for the kinetic energy, and only those plane waves (wavevector denoted as $\boldsymbol{k}+\boldsymbol{G}$) satisfying $|\boldsymbol{k}+\boldsymbol{G}|^2/2 \leqslant E_{\rm cut}$ are retained. Indeed, there is a certain degree of inaccuracy by replacing the infinite basis set by a finite one, but the precision is very conveniently controlled through the magnitude of $E_{\rm cut}$. An important point has to be noted, that for distinct $\boldsymbol{k}$ points, the maximum magnitude of $\boldsymbol{G}$ may also differ. This is possible because it is $|\boldsymbol{k}+\boldsymbol{G}|$ instead of $|\boldsymbol{G}|$ that is used to calculate the kinetic energy. As illustrated by the red and blue circles in figure 12, when the $\boldsymbol{k}$ point changes, it is equivalent to a shift in the center of the circle, where $G_{\rm cut} = \sqrt{2E_{\rm cut}}$. Consequently, the reciprocal lattice points enclosed within the two circles are not entirely identical.

For a specified $\boldsymbol{k}$ point, the Bloch state of the $n^{\rm th}$ band $\psi_{n,\boldsymbol{k}}(\boldsymbol{r})$ can be expanded in terms of the plane wave bases. The normal expression for a plane wave is $\phi_{\boldsymbol{G}+\boldsymbol{k}}(\boldsymbol{r}) = \mathrm{e}^{i(\boldsymbol{G}+\boldsymbol{k})\cdot\boldsymbol{r}}/\sqrt{\Omega}$, and its forward and inverse Fourier transform formulae both involve the factor $1/\sqrt{\Omega}$. For notational simplicity and the convenience in computational implementation, we shall take

$$\phi_{\boldsymbol{G}+\boldsymbol{k}}(\boldsymbol{r}) = \mathrm{e}^{i(\boldsymbol{G}+\boldsymbol{k})\cdot\boldsymbol{r}} \tag{4-3}$$

instead, thus

$$\psi_{n,\boldsymbol{k}}(\boldsymbol{r}) = \sum_{\boldsymbol{G}_m} c_{n,\boldsymbol{k}}(\boldsymbol{G}_m)\,\phi_{\boldsymbol{G}_m+\boldsymbol{k}}(\boldsymbol{r}) = \sum_{\boldsymbol{G}_m} c_{n,\boldsymbol{k}}(\boldsymbol{G}_m)\,\mathrm{e}^{i(\boldsymbol{G}_m+\boldsymbol{k})\cdot\boldsymbol{r}} \tag{4-4}$$

where the coefficient $c_{n,\boldsymbol{k}}(\boldsymbol{G}_m)$ is nothing but the Fourier transform of $\psi_{n,\boldsymbol{k}}(\boldsymbol{r})$

$$c_{n,\boldsymbol{k}}(\boldsymbol{G}) = \frac{1}{\Omega}\int_{\Omega} \mathrm{d}\boldsymbol{r}\;\psi_{n,\boldsymbol{k}}(\boldsymbol{r})\,e^{-i(\boldsymbol{G}+\boldsymbol{k})\cdot\boldsymbol{r}}. \tag{4-5}$$

Although we have revised the definition of $\phi_{\boldsymbol{G}+\boldsymbol{k}}(\boldsymbol{r})$, through removing its normalization factor, the forward/inverse Fourier transform pair has been adjusted accordingly. Henceforth, we employ the simplified definition (4-3) for plane waves, instead of (3-9). In addition, only the forward Fourier transform contains the factor $1/\Omega$, while the inverse Fourier transform has no additional factor.

The electron density comes from the modulus square of the wavefunction, where in real space one writes

$$n(\boldsymbol{r}) = \frac{1}{N_k}\sum_{\boldsymbol{k}}\sum_{n} f_{n,\boldsymbol{k}}\left|\psi_{n,\boldsymbol{k}}(\boldsymbol{r})\right|^2 \tag{4-6}$$

$$\left|\psi_{n,\boldsymbol{k}}(\boldsymbol{r})\right|^2 = \psi^*_{n,\boldsymbol{k}}(\boldsymbol{r})\,\psi_{n,\boldsymbol{k}}(\boldsymbol{r}) = \sum_{\boldsymbol{G},\boldsymbol{G}'} c^*_{n,\boldsymbol{k}}(\boldsymbol{G})\,c_{n,\boldsymbol{k}}(\boldsymbol{G}')\,\mathrm{e}^{i(\boldsymbol{G}'-\boldsymbol{G})\cdot\boldsymbol{r}}. \tag{4-7}$$

Here N_k is the number of k points to sample the Brillouin zone, and $f_{n,\boldsymbol{k}} \in [0,\ 1]$ stands for the occupation number of the nth band for wavevector $\boldsymbol{k}$. When one expands the electron density in terms of plane waves, its Fourier components cover those with $|\boldsymbol{G}| \leqslant 2G_{\rm cut}$, as indicated by the green circle in figure 12, because of the $\boldsymbol{G}'-\boldsymbol{G}$ operation. Provided that one carries out the calculation in the reciprocal space, it is equivalent to a convolution operation. If the grid is such chosen that $|\boldsymbol{G}+\boldsymbol{k}| \leqslant G_{\rm cut}$, this will inevitably lead to the so-called 'wrap-around error', which is intrinsically due to the down sampling. Note that, when representing the electron density in the reciprocal space, the phase factor $\mathrm{e}^{i\boldsymbol{k}\cdot\boldsymbol{r}}$ cancels out during the calculation, and all Fourier components with $|\boldsymbol{G}| \leqslant 2G_{\rm cut}$ ought to be considered, instead of $|\boldsymbol{G}+\boldsymbol{k}| \leqslant 2G_{\rm cut}$.

In using the plane-wave bases, a kinetic energy cutoff of $E_{\rm cut}$ thus requires an initial grid with $|\boldsymbol{G}| \leqslant 2G_{\rm cut}$ in order to avoid any wrap-around error. Provided that one is calculating the electronic energy eigenvalues at $\boldsymbol{k}$, then only those $\boldsymbol{G}$ (reciprocal lattice vectors) satisfying $|\boldsymbol{G}+\boldsymbol{k}| \leqslant G_{\rm cut}$ are needed. During inverse FFT (FFT^{-1}), the wavefunction in reciprocal space is transformed into real space, with all Fourier components beyond this range set to zero. Let the lattice vectors of the unit cell be $\boldsymbol{a}_x, \boldsymbol{a}_y, \boldsymbol{a}_z$, and the corresponding reciprocal space basis vectors are $\boldsymbol{b}_x, \boldsymbol{b}_y, \boldsymbol{b}_z$. The minimum grid size required to satisfy $|\boldsymbol{G}| \leqslant 2G_{\rm cut}$ is $2\times(2G_{\rm cut}/|\boldsymbol{b}_i|)+1$, for $i = x, y, z$, resulting in an odd number. The earliest FFT mesh size was restricted to powers in the form of 2^n, asking to pad with a significant number of zeros if the grid size deviates substantially from the next value of 2^n. The development of the FFT algorithm allows the FFT grid size to be composed of small prime factors, denoted as $N = 2^a \times 3^b \times 5^c$. Compared with using 2^n, there is a certain loss of efficiency accordingly. Nevertheless, the amount of stored data gets reduced, though one should avoid using big prime numbers for the sake of computational speed.

A wavefunction may be stored in real space, or in reciprocal space, with distinct amounts of data. Given a G_{cut} value, in reciprocal space one needs the coefficients for $N_{\text{PW}} \propto 4\pi\left(G_{\text{cut}}\right)^3/3$ plane waves. After FFT, however, the real space wavefunction corresponds to a data amount of $16\,N_{\text{PW}} \propto (\pi/3)\left(4G_{\text{cut}}\right)^3$. Therefore, working in the reciprocal space could effectively reduce the size of the Hamiltonian matrix. However, to obtain the electron density, one needs a convolution operation in the reciprocal space, with a computational load of $O\left(N_{\text{PW}}^2\right)$. If calculated in real space, the electron density only requires modulus square operations for the wavefunction on each grid point, with a computational load of $O\left(16N_{\text{PW}}\right)$, which is much lighter. It is for this reason that one still needs to utilize the real space, making FFT^{-1} to enable electron density calculation in real space. The computational load of this inverse FFT is $O\left(16N_{\text{PW}}\log\left(16N_{\text{PW}}\right)\right)$. Notwithstanding the FFT^{-1} and the subsequent FFT procedures, it is still much faster to calculate the electron density in real space rather than in reciprocal space.

In the plane-wave formalism, the potential function also needs to be transformed into reciprocal space. For this purpose, the specific form for the matrix elements of the local potential function in reciprocal space is introduced below. A local potential function $V_{\text{eff}}(\boldsymbol{r})$ may be re-written in reciprocal space as

$$V_{\text{eff}}(\boldsymbol{G}) = \frac{1}{\Omega_{\text{cell}}}\int_{\Omega_{\text{cell}}} \mathrm{d}\boldsymbol{r} V_{\text{eff}}(\boldsymbol{r})\,\mathrm{e}^{-i\boldsymbol{G}\cdot\boldsymbol{r}}. \tag{4-8}$$

Or inversely one has

$$V_{\text{eff}}(\boldsymbol{r}) = \sum_{\boldsymbol{G}_m} V_{\text{eff}}(\boldsymbol{G}_m)\,\mathrm{e}^{i\boldsymbol{G}_m\cdot\boldsymbol{r}}. \tag{4-9}$$

Hence,

$$\begin{aligned}\langle\phi_{\boldsymbol{G}+\boldsymbol{k}}|V_{\text{eff}}|\phi_{\boldsymbol{G}'+\boldsymbol{k}}\rangle &= \frac{1}{\Omega_{\text{cell}}}\int_{\Omega_{\text{cell}}} \mathrm{d}\boldsymbol{r}\sum_{\boldsymbol{G}_m} V_{\text{eff}}(\boldsymbol{G}_m)\,\mathrm{e}^{i\boldsymbol{G}_m\cdot\boldsymbol{r}}\;\mathrm{e}^{i(\boldsymbol{G}'-\boldsymbol{G})\cdot\boldsymbol{r}}\\ &= \sum_{\boldsymbol{G}_m} V_{\text{eff}}(\boldsymbol{G}_m)\,\delta_{\boldsymbol{G}-\boldsymbol{G}',\boldsymbol{G}_m}.\end{aligned} \tag{4-10}$$

Now it is clear that representing the Kohn–Sham equation in the reciprocal space brings about great savings in computational time, though for electron density calculation it is necessary to switch to the real space. Nevertheless, one question remains as that at an arbitrary $\boldsymbol{k}$ point, the basis function ought to be $\mathrm{e}^{i(\boldsymbol{G}+\boldsymbol{k})\cdot\boldsymbol{r}}$ during inverse FFT, which contains an additional phase factor $\mathrm{e}^{i\boldsymbol{k}\cdot\boldsymbol{r}}$. In reality, the FFT^{-1} program only uses $\mathrm{e}^{i\boldsymbol{G}\cdot\boldsymbol{r}}$. This is however not a big deal for electron density calculation, because $\left|\mathrm{e}^{i\boldsymbol{k}\cdot\boldsymbol{r}}\right|^2 \equiv 1$ and its impact after FFT^{-1} and FFT disappears. In particular, the FFT process should involve $\mathrm{e}^{-i(\boldsymbol{G}+\boldsymbol{k})\cdot\boldsymbol{r}}$, thus the factor $\mathrm{e}^{-i\boldsymbol{k}\cdot\boldsymbol{r}}$ exactly cancels the problematic $\mathrm{e}^{i\boldsymbol{k}\cdot\boldsymbol{r}}$ factor. Provided that one needs to output the exact wavefunction in real space, each wavefunction at $\boldsymbol{r}$ ought to be multiplied by a factor $\mathrm{e}^{i\boldsymbol{k}\cdot\boldsymbol{r}}$.

4.2. Hamiltonian construction and total energy expression

With a proper basis set at hand, the next tasks are to construct the Kohn-Sham equations (Task-I), and to derive the total energy of the solid per unit cell (Task-II). From now on we shall simply refer to ‘total energy’, without emphasizing that it is for one unit cell. Task-I and Task-II are distinct but with certain relations. The key to the solution of a Kohn–Sham equation is to construct the Hamiltonian under the representation of the basis set (plane waves). Diagonalization of this Hamiltonian yields the electronic energy eigenvalues $\varepsilon_{n,\boldsymbol{k}}$, as well as the corresponding Bloch states. At zero absolute temperature, these states are either occupied or unoccupied, even for the metal case. The reason lies in that, an energy band may be partially occupied, but this statement is done for a global set of states belonging to that particular band. Partial occupation means a portion of the states at some $\boldsymbol{k}$ points are occupied, while others are unoccupied, as long as the calculation is done at zero temperature. Hence, so far as a single specified $\boldsymbol{k}$ point is concerned, whether a derived electronic state is occupied can be determined according to the total electron number in a unit cell. This is feasible whenever the $\boldsymbol{k}$ point sampling is sufficiently fine within the first Brillouin zone. After the Kohn–Sham equations are solved for all the $\boldsymbol{k}$ points, the definite number of electrons per unit cell start to fill these states from the lowest possible energy level. If spin polarization is not allowed in the calculation, each low-lying band accommodates two electrons per unit cell; otherwise each low-lying band has a one-to-one correspondence to the related electron in a unit cell. Near the Fermi level, band crossing could occur, leading to more complicated distributions. Even so, the Fermi level (or the top of valence band for an insulator/semiconductor) is readily obtained considering the electron filling situation. Subsequently, whether a particular electronic state at $\boldsymbol{k}$ is occupied depends on its energy eigenvalue with comparison to the Fermi level. The statement above aims at providing a general physical picture for the derivation of $n(r)$ from the electronic energy eigenstates at zero absolute temperature. It does not forbid any smearing techniques for the sake of acceleration during the calculation, such as Fermi smearing, Gaussian smearing and Methfessel–Paxton smearing [103].

The total energy is merely the sum of energy eigenvalues for all electrons, plus the ion-ion interaction (Madelung) energy. One cannot exhaustively compute all occupied electronic states, because an ideal crystal is extended such that there are infinitely many states within an energy band. The Brillouin zone sampling method addresses this by selecting a finite set of $\boldsymbol{k}$ points to approximate the integration over the entire first Brillouin zone. The equal-spacing Monkhorst–Pack scheme [104] is most widely used nowadays. Suppose one employs a $4 \times 4 \times 4$ $\boldsymbol{k}$ mesh to sample the Brillouin zone, which contains 64 $\boldsymbol{k}$ points in total. Yet, a certain group of $\boldsymbol{k}$ points may be equivalent, due to the crystal symmetry. Hence, in reality one only carries out calculations for those ‘irreducible’ $\boldsymbol{k}$ points. This means that one does not handle all the 64 $\boldsymbol{k}$ points with a weight factor of 1/64 for each. Rather, the number of $\boldsymbol{k}$ points under calculation is typically much less, and their weights can differ. Consider, for example, cubic $\mathrm{SrTiO_3}$ with space group $Pm\bar{3}m$. There are merely 4 irreducible $\boldsymbol{k}$ points for its $4\times4\times4$ Monkhorst–Pack mesh, *i.e.* $\boldsymbol{k}_1 = (1/8,\ 1/8,\ 1/8)$, $\boldsymbol{k}_2 = (3/8,\ 1/8,\ 1/8)$, $\boldsymbol{k}_3 = (3/8,\ 3/8,\ 1/8)$, and $\boldsymbol{k}_4 = (3/8,\ 3/8,\ 3/8)$. The units are in reciprocal lattice constants. However, $\boldsymbol{k}_1$ actually represents 8 equivalent $\boldsymbol{k}$ points in the mesh, and $\boldsymbol{k}_2$ represents as many as 24 equivalent $\boldsymbol{k}$ points. And $\boldsymbol{k}_3$ is 24-fold while $\boldsymbol{k}_4$ is 8-fold. The weights of $\boldsymbol{k}_1$ and $\boldsymbol{k}_4$ are both $8/64 = 1/8$, while the weights of $\boldsymbol{k}_2$ and $\boldsymbol{k}_3$ are both $24/64 = 3/8$. We shall use the symbol $w_{\boldsymbol{k}}$ to denote the weight of a selected wavevector $\boldsymbol{k}$. Accordingly, in the $\mathrm{SrTiO_3}$ example, $w_{\boldsymbol{k}_1} = w_{\boldsymbol{k}_4} = 1/8$ and $w_{\boldsymbol{k}_2} = w_{\boldsymbol{k}_3} = 3/8$. The total energy can be expressed in terms of these weights as

$$E_{\mathrm{total}} = N_\sigma \sum_{\boldsymbol{k},n} f_{n,\boldsymbol{k}} w_{\boldsymbol{k}} \varepsilon_{n,\boldsymbol{k}} + E_{\mathrm{II}}. \tag{4-11}$$

Here N_σ is a spin degeneracy factor, which equals 2 if spin polarization is forbidden; otherwise it is unity. The occupation number $f_{n,\boldsymbol{k}}$ has been introduced in section 4.1. It then follows that Task-II relies on Task-I, because it is Task-I that generates the desired $\varepsilon_{n,\boldsymbol{k}}$ values. In Task-I, each one-electron Hamiltonian may be separated into several parts, including one-electron kinetic energy and various potential energies. Each part is handled individually, but there are some additional difficulties in this scheme. First of all, there is a divergent problem when working in the reciprocal space, since some potentials such as V_{Hartree} and $V_{\mathrm{ps,local}}$ are divergent at $|\boldsymbol{G}| = 0$. Secondly, there are more than one grids that have to be used. For instance, the plane wave grid satisfies $|\boldsymbol{G}+\boldsymbol{k}| \leqslant G_{\mathrm{cut}}$, but in calculating the electron density, one needs an expanded grid of $|\boldsymbol{G}| \leqslant 2G_{\mathrm{cut}}$. These issues will be attacked in the following sections.

Before discussing the numerically efficient algorithms to diagonalize the Hamiltonian, it is essential to emphasize the labeling scheme when band crossing occurs. A simple example with band crossing is illustrated in figure 13, where metal beryllium in the hexagonal $P6_3/mmc$ structure is calculated without spin polarization. In the context of solid-state physics, the identification of Band-2 or Band-3 is like that in figure 13(a), where a crossing point is present along the Γ–M line. However, a practical calculation processes individual $\boldsymbol{k}$ points separately, resulting in Band-2/Band-3 assignments as in figure 13(b). In other words, one cannot foresee the band crossing events that would invert the energy ordering (*e.g.* assigning index 2 to a higher energy eigenvalue, while assigning band index 3 to a lower energy eigenvalue, given a specific $\boldsymbol{k}$ point). Consequently, if one needs to recover the conventional band index identification as in solid-state physics, re-indexing of the raw eigenvalues is required after constructing the band diagram.

We now analyze the computational efficiency of obtaining energy eigenvalues at a given $\boldsymbol{k}$ point. To gain a clearer insight, one may consider a scenario where the basis set comprises 1000 plane waves ($N_{\mathrm{PW}} = 1000$), and 10 target energy bands are to be calculated ($N_{\mathrm{bands}} = 10$). Both N_{PW} and N_{bands} are of comparable magnitude in typical energy band calculations (*e.g.* silicon). Notably, not all bands under investigation are occupied by electrons—for semiconductors, the conduction band and even higher-lying unoccupied bands require explicit treatment. At each $\boldsymbol{k}$ point, the Hamiltonian is represented by an $N_{\mathrm{PW}} \times N_{\mathrm{PW}}$ matrix, while wavefunctions are in $N_{\mathrm{PW}} \times 1$ vectors. Each physical term within the Hamiltonian (kinetic energy, Hartree potential energy, *etc.*) is also an $N_{\mathrm{PW}} \times N_{\mathrm{PW}}$ matrix. All these matrices sum up to yield the complete Hamiltonian, which consists of ∼1 million ($N_{\mathrm{PW}} \times N_{\mathrm{PW}}$) matrix elements. Direct diagonalization of this Hamiltonian only yields N_{PW} energy eigenstates. This is not a serious limitation, since it is natural to have $N_{\mathrm{bands}} \ll N_{\mathrm{PW}}$. Hence, this direct diagonalization scheme provides sufficient results, but it incurs significant computational overhead by processing numerous unoccupied bands.

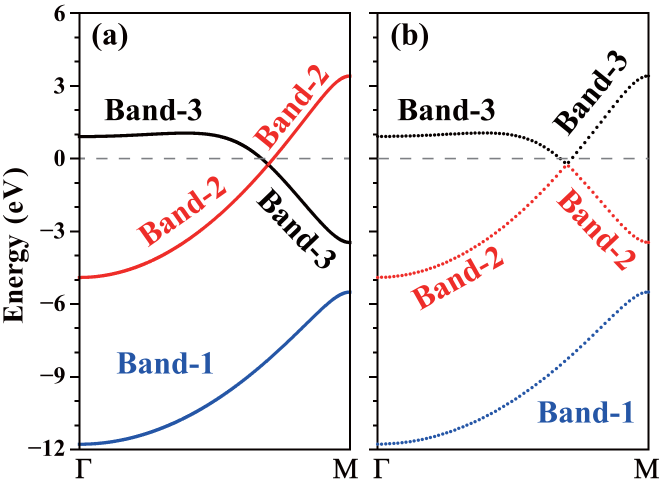

Figure 13. Band diagram of metal Be along the Γ–M line. (a) Assignment of band indices according to the convention in solid-state physics; (b) band index assignment scheme according to direct calculation results.

Fortunately, as a cornerstone of numerical linear algebra, matrix diagonalization algorithms have undergone transformative advancements in the past century. A pivotal breakthrough lies in eliminating the need for explicit storage of the full Hamiltonian matrix. This progress is fundamentally enabled by the Rayleigh quotient—a mathematical formalism central to modern iterative eigenvalue solvers. Hence, fundamentals of the Rayleigh quotient will be reviewed here. For any Hermitian matrix $\boldsymbol{A}$ and a non-zero vector $\mathbf{x}$, their Rayleigh quotient is defined as

$$Rq(\boldsymbol{A},\mathbf{x}) = \frac{\mathbf{x}^\dagger \boldsymbol{A}\mathbf{x}}{\mathbf{x}^\dagger \mathbf{x}}. \tag{4-12}$$

Suppose the situation is extended to a generalized eigenvalue problem, *i.e.* $\boldsymbol{A}\mathbf{x} = \lambda \boldsymbol{S}\mathbf{x}$ with $\boldsymbol{S}$ not equal to the identity matrix, the Rayleigh quotient becomes

$$Rq(\boldsymbol{A},\mathbf{x}) = \frac{\mathbf{x}^\dagger \boldsymbol{A}\mathbf{x}}{\mathbf{x}^\dagger \boldsymbol{S}\mathbf{x}}. \tag{4-13}$$

Several important properties of $Rq(\boldsymbol{A},\mathbf{x})$ are summarized as follows.

(i) In case $\mathbf{x}$ is an eigenvector of matrix $\boldsymbol{A}$ with eigenvalue λ, then

$$Rq(\boldsymbol{A},\mathbf{x}) = \frac{\mathbf{x}^{\dagger}\boldsymbol{A}\mathbf{x}}{\mathbf{x}^{\dagger}\mathbf{x}} = \frac{\mathbf{x}^{\dagger}(\lambda\mathbf{x})}{\|\mathbf{x}\|^{2}} = \lambda \tag{4-14}$$

which means that the Rayleigh quotient is exactly the eigenvalue.

(ii) For any $\mathbf{x}$ vector satisfying $\|\mathbf{x}\| = 1$, its Rayleigh quotient satisfies

$$\lambda_{\min} \leqslant Rq(\boldsymbol{A},\mathbf{x}) \leqslant \lambda_{\max} \tag{4-15}$$

where $\lambda_{\min}$ and $\lambda_{\max}$ are the minimum and the maximum eigenvalues of matrix $\boldsymbol{A}$, respectively. Given the Hermicity of $\boldsymbol{A}$, all eigenvalues are real. Hence, it is feasible to write $\lambda_{\min} = \lambda_1 \leqslant \lambda_2 \leqslant \ldots \leqslant \lambda_N = \lambda_{\max}$, where the corresponding eigenvectors (assuming no degeneracy) are $\mathbf{v}_1, \mathbf{v}_2, \ldots, \mathbf{v}_N$. The vector $\mathbf{x}$ is expressed as

$$\mathbf{x} = c_1\mathbf{v}_1 + c_2\mathbf{v}_2 + \ldots + c_N\mathbf{v}_N. \tag{4-16}$$

Now that the norm of $\mathbf{x}$ is unity, one has $\sum_{i=1}^{N} |c_i|^2 = 1$, thus

$$Rq(\boldsymbol{A},\mathbf{x}) = \mathbf{x}^{\dagger}\boldsymbol{A}\mathbf{x} = \sum_{i=1}^{N} |c_i|^2 \lambda_i. \tag{4-17}$$

Due to

$$\lambda_1 \sum_{i=1}^{N} |c_i|^2 \leqslant \sum_{i=1}^{N} |c_i|^2 \lambda_i \leqslant \lambda_N \sum_{i=1}^{N} |c_i|^2 \tag{4-18}$$

it follows that $\lambda_{\min} \leqslant Rq(\boldsymbol{A},\mathbf{x}) \leqslant \lambda_{\max}$. This implies that, through minimizing the Rayleigh quotient, one could find the lowest eigenvalue and the corresponding eigenvector for $\boldsymbol{A}$.

(iii) The gradient of the Rayleigh quotient is

$$\boldsymbol{\nabla} Rq(\boldsymbol{A},\mathbf{x}) = \frac{2}{\|\mathbf{x}\|^{2}} \left(\boldsymbol{A}\mathbf{x} - Rq(\boldsymbol{A},\mathbf{x})\,\mathbf{x}\right). \tag{4-19}$$

Whenever the gradient is zero, $\boldsymbol{A}\mathbf{x} = Rq(\boldsymbol{A},\mathbf{x})\,\mathbf{x}$ becomes valid. In case this condition is reached, $\mathbf{x}$ is the desired eigenvector and $Rq(\boldsymbol{A},\mathbf{x})$ is the eigenvalue.

The above properties of Rayleigh quotient inform us that, it is not necessary to diagonalize the complete Hamiltonian matrix, but one can turn to obtaining the eigenvalues and eigenfunctions of the lowest few bands, with band index ranging from 1 to N_{bands}. This is achieved through a minimization procedure towards the lower bound of the Rayleigh quotients. Up to now, the theoretical framework is equivalent to the well-known variational principle in quantum mechanics, though the Rayleigh quotient formalism is a discrete version. Nevertheless, a further scrutiny reveals that, one could always treat $\boldsymbol{A}\mathbf{x}$ together, as a vector. As long as all $\mathbf{x}$ and $\boldsymbol{A}\mathbf{x}$ are stored, there is no need to store the matrix $\boldsymbol{A}$ for optimization. In the case of solid calculations using the plane wave basis, only the two sets of vectors $|\psi_{n,\boldsymbol{k}}\rangle$ and $\widehat{H}|\psi_{n,\boldsymbol{k}}\rangle$ have to be stored. This could reduce the amount of data storage to the level of $KN_{\text{PW}}N_{\text{bands}}$, where K is a scaling factor with its value estimated to be 2–3. The reason for $K > 1$ is that, some extra room in the number of bands may be required during the optimization procedure (cf section 4.3.2).

In the following subsections, each physical part of the one-electron Hamiltonian, such as kinetic energy and Hartree potential, will be regarded as the $\hat{A}$ operator in the Rayleigh quotient formalism. We shall review the matrix elements of $\boldsymbol{A}$ in the reciprocal space, *i.e.* $\langle\phi_{\boldsymbol{G}+\boldsymbol{k}}|\hat{A}\,|\phi_{\boldsymbol{G}'+\boldsymbol{k}}\rangle$, the vector form $\hat{A}\,|\psi_{n,\boldsymbol{k}}\rangle$ for the sake of matrix diagonalization, and the contribution from operator $\hat{A}$ in the total energy.

4.2.1. Kinetic energy.

Now that it is preferred to write the Kohn-Sham equation in reciprocal space, one must be able to express the Hamiltonian matrix in reciprocal space. The kinetic energy operator $\widehat{T} = -\nabla^2/2$ is simple to handle, since it has a definite analytical form for a single plane wave

$$\widehat{T}\phi_{\boldsymbol{G}+\boldsymbol{k}}(\boldsymbol{r}) = -\frac{\nabla^2}{2}\mathrm{e}^{i(\boldsymbol{G}+\boldsymbol{k})\cdot\boldsymbol{r}} = \frac{|\boldsymbol{G}+\boldsymbol{k}|^2}{2}\mathrm{e}^{i(\boldsymbol{G}+\boldsymbol{k})\cdot\boldsymbol{r}}. \tag{4-20}$$

The matrix element of the kinetic energy operator is

$$\langle\phi_{\boldsymbol{G}+\boldsymbol{k}}|\widehat{T}|\phi_{\boldsymbol{G}'+\boldsymbol{k}}\rangle = \frac{|\boldsymbol{G}+\boldsymbol{k}|^2}{2}\delta_{\boldsymbol{G},\boldsymbol{G}'}. \tag{4-21}$$

The kinetic energy operator is represented by a diagonal matrix because plane waves are the eigenstates of it. The matrix $\boldsymbol{T}$ only has N_{PW} non-zero elements. When acting on an electronic state $\psi_{n,\boldsymbol{k}}$, one obtains the following vector

$$\begin{aligned}\widehat{T}|\psi_{n,\boldsymbol{k}}\rangle &= \begin{bmatrix} \frac{|\boldsymbol{G}_1+\boldsymbol{k}|^2}{2} & \cdots & 0 \\ \vdots & \ddots & \vdots \\ 0 & \cdots & \frac{|\boldsymbol{G}_{N_{\text{PW}}}+\boldsymbol{k}|^2}{2} \end{bmatrix} \begin{bmatrix} c_{n,\boldsymbol{k}}(\boldsymbol{G}_1) \\ \vdots \\ c_{n,\boldsymbol{k}}(\boldsymbol{G}_{N_{\text{PW}}}) \end{bmatrix} \\ &= \begin{bmatrix} \frac{|\boldsymbol{G}_1+\boldsymbol{k}|^2}{2} c_{n,\boldsymbol{k}}(\boldsymbol{G}_1) \\ \vdots \\ \frac{|\boldsymbol{G}_{N_{\text{PW}}}+\boldsymbol{k}|^2}{2} c_{n,\boldsymbol{k}}(\boldsymbol{G}_{N_{\text{PW}}}) \end{bmatrix}. \end{aligned} \tag{4-22}$$

This finished Task-I, whose primary objective is exactly finding $\hat{A}\,|\psi_{n,\boldsymbol{k}}\rangle$. For Task-II, we proceed as follows. Since the bra of the valence electronic state under investigation is

$$\langle\psi_{n,\boldsymbol{k}}| = \left[c^{*}_{n,\boldsymbol{k}}(\boldsymbol{G}_1),\ c^{*}_{n,\boldsymbol{k}}(\boldsymbol{G}_2), \cdots,\ c^{*}_{n,\boldsymbol{k}}(\boldsymbol{G}_{N_{\text{PW}}})\right] \tag{4-23}$$

the kinetic energy expectation value for $\psi_{n,\boldsymbol{k}}$ is derived through a combination of equations (4-22) and (4-23)

$$\langle\psi_{n,\boldsymbol{k}}|\widehat{T}|\psi_{n,\,k}\rangle=\sum_{\boldsymbol{G}_m}\frac{|\boldsymbol{G}_m+\boldsymbol{k}|^2}{2}|c_{n,\boldsymbol{k}}(\boldsymbol{G}_m)|^2 \qquad (4\text{-}24)$$

where $m=1,2,\cdots N_{\mathrm{PW}}$. Actually, only those $\boldsymbol{G}_m$ values with $|\boldsymbol{G}_m+\boldsymbol{k}|\leqslant G_{\mathrm{cut}}$ are included in the summation. We emphasize that equation (4-24) only characterizes the contribution from a single electronic state. To obtain the total Kohn-Sham kinetic energy T_s (slightly different from the true total kinetic energy T, cf section 2.1), a double sum over band indices and $\boldsymbol{k}$ points is needed, so as to cover all occupied electronic states. The final result is

$$T_s=\sum_{\boldsymbol{k},n}w_{\boldsymbol{k}}\left[\sum_{\boldsymbol{G}_m}\frac{|\boldsymbol{k}+\boldsymbol{G}_m|^2}{2}|c_{n,\boldsymbol{k}}(\boldsymbol{G}_m)|^2\right]. \qquad (4\text{-}25)$$

4.2.2. Hartree energy.

The Hartree energy between electrons (electron merely treated as the carrier of charge) is

$$E_{\mathrm{Hartree}}=\frac{1}{2}\iint\mathrm{d}\boldsymbol{r}\mathrm{d}\boldsymbol{r}'\frac{n(\boldsymbol{r})\,n(\boldsymbol{r}')}{|\boldsymbol{r}-\boldsymbol{r}'|} \qquad (4\text{-}26)$$

whose functional derivative with respect to the electron density is

$$V_{\mathrm{Hartree}}(\boldsymbol{r})=\frac{\delta E_{\mathrm{Hartree}}}{\delta n(\boldsymbol{r})}=\left[\frac{1}{2}\int\mathrm{d}\boldsymbol{r}'\frac{n(\boldsymbol{r}')}{|\boldsymbol{r}-\boldsymbol{r}'|}\right]\times 2=\int\mathrm{d}\boldsymbol{r}'\frac{n(\boldsymbol{r}')}{|\boldsymbol{r}-\boldsymbol{r}'|}. \qquad (4\text{-}27)$$

It may also be obtained by solving the Poisson equation

$$\nabla^2V_{\mathrm{Hartree}}(\boldsymbol{r})=-4\pi n(\boldsymbol{r}). \qquad (4\text{-}28)$$

These two formulations are actually equivalent. Note that both approaches work in the real space, instead of the reciprocal space. There is a simple approach to replace the partial differential equation (4-28) by an algebraic equation. Let us consider an arbitrary real function $g(x)$ and its Fourier transform $\mathcal{F}[g(x)]$. A further Fourier transform of its derivative, $g'(x)=\mathrm{d}g(x)/\mathrm{d}x$, gives

$$\begin{aligned}\mathcal{F}\{g'(x)\}&=\int_{-\infty}^{+\infty}g'(x)\,\mathrm{e}^{-ikx}\mathrm{d}x=g(x)\,\mathrm{e}^{-ikx}|_{-\infty}^{+\infty}\\&\quad-\int_{-\infty}^{+\infty}g(x)(-ik)\,\mathrm{e}^{-ikx}\mathrm{d}x\end{aligned} \qquad (4\text{-}29)$$

where the trick of integration by parts has been applied. Suppose $g(x)$ is continuous in the entire region $(-\infty,+\infty)$, and $g(x)\to0$ as $|x|\to+\infty$. The term $g(x)\,\mathrm{e}^{-ikx}|_{-\infty}^{+\infty}$ will vanish, thus

$$\mathcal{F}[g'(x)]=ik\mathcal{F}[g(x)]. \qquad (4\text{-}30)$$

For higher-order derivatives, provided that the jth order derivative $\mathrm{d}^jg/\mathrm{d}x^j$ is continuous on $(-\infty,+\infty)$, and satisfies $\mathrm{d}^{j-1}g/\mathrm{d}x^{j-1}\to0$ as $|x|\to+\infty$, the Fourier transform of the jth derivative is given by

$$\mathcal{F}\left[\frac{\mathrm{d}^jg(x)}{\mathrm{d}x^j}\right]=(ik)^j\mathcal{F}[g(x)]. \qquad (4\text{-}31)$$

This relation is highly useful for deriving $V_{\mathrm{Hartree}}(\boldsymbol{G})$. First note that the Fourier transform of $V_{\mathrm{Hartree}}(\boldsymbol{r})$ is

$$\mathcal{F}[V_{\mathrm{Hartree}}(\boldsymbol{r})]=V_{\mathrm{Hartree}}(\boldsymbol{G})=\frac{1}{\Omega_{\mathrm{cell}}}\int_{\Omega_{\mathrm{cell}}}\mathrm{d}\boldsymbol{r}\;V_{\mathrm{Hartree}}(\boldsymbol{r})\,e^{-i\boldsymbol{G}\cdot\boldsymbol{r}}. \qquad (4\text{-}32)$$

According to equation (4-31), for higher derivatives one has

$$\mathcal{F}\left\{\boldsymbol{\nabla}^jV_{\mathrm{Hartree}}(\boldsymbol{r})\right\}=(i\boldsymbol{G})^jV_{\mathrm{Hartree}}(\boldsymbol{G}). \qquad (4\text{-}33)$$

Therefore, the Poisson equation is converted into the reciprocal space as, using $j=2$,

$$V_{\mathrm{Hartree}}(\boldsymbol{G})=\frac{4\pi n(\boldsymbol{G})}{|\boldsymbol{G}|^2} \qquad (4\text{-}34)$$

which involves the reciprocal space representation of n, as is straightforwardly available through a Fourier transform of $n(\boldsymbol{r})$. With $n(\boldsymbol{G})$ at hand, $V_{\mathrm{Hartree}}(\boldsymbol{G})$ is simply obtained through multiplication and division. A subsequent inverse Fourier transform yields the real space Hartree potential

$$V_{\mathrm{Hartree}}(\boldsymbol{r})=\sum_{\boldsymbol{G}_m}V_{\mathrm{Hartree}}(\boldsymbol{G}_m)\,\mathrm{e}^{i\boldsymbol{G}_m\cdot\boldsymbol{r}}. \qquad (4\text{-}35)$$

According to equation (4-10), the matrix element of $\widehat{V}_{\mathrm{Hartree}}$ in the reciprocal space is

$$\langle\phi_{\boldsymbol{G}+\boldsymbol{k}}|\,\widehat{V}_{\mathrm{Hartree}}\,|\phi_{\boldsymbol{G}'+\boldsymbol{k}}\rangle=\sum_{\boldsymbol{G}_m}V_{\mathrm{Hartree}}(\boldsymbol{G}_m)\,\delta_{\boldsymbol{G}-\boldsymbol{G}',\boldsymbol{G}_m}. \qquad (4\text{-}36)$$

The matrix $\boldsymbol{V}_{\mathrm{Hartree}}$ is not diagonal, and a series of off-diagonal elements are non-zero provided that their row and column indices satisfy the required condition. And when acting on $|\psi_{n,\boldsymbol{k}}\rangle$, one finds

$$\begin{aligned}\widehat{V}_{\mathrm{Hartree}}\,|\psi_{n,\boldsymbol{k}}\rangle&=\left[\sum_{\boldsymbol{G}_m}V_{\mathrm{Hartree}}(\boldsymbol{G}_m)\,\mathrm{e}^{i\boldsymbol{G}_m\cdot\boldsymbol{r}}\right]\\&\quad\times\left[\sum_{\boldsymbol{G}_{m'}}c_{n,\boldsymbol{k}}(\boldsymbol{G}_{m'})\,\phi_{\boldsymbol{G}_{m'}+\boldsymbol{k}}(\boldsymbol{r})\right]\\&=\sum_{\boldsymbol{G}_{m'}}\left[\sum_{\boldsymbol{G}_m}V_{\mathrm{Hartree}}(\boldsymbol{G}_m)\,\mathrm{e}^{i\boldsymbol{G}_m\cdot\boldsymbol{r}}\right]\\&\quad\times c_{n,\boldsymbol{k}}(\boldsymbol{G}_{m'})\,\phi_{\boldsymbol{G}_{m'}+\boldsymbol{k}}(\boldsymbol{r}).\end{aligned} \qquad (4\text{-}37)$$

Here $c_{n,\boldsymbol{k}}$ are the plane wave expansion coefficients for $\psi_{n,\boldsymbol{k}}$. In the theoretical sense, we have finished Task-I, since $\widehat{V}_{\mathrm{Hartree}}\,|\psi_{n,\boldsymbol{k}}\rangle$ is obtained. Yet, this expression appears to be complicated. Here $\boldsymbol{G}_{m'}$ covers all the plane wave components, and a vector form of $\widehat{V}_{\text{Hartree}}\left|\psi_{n,\boldsymbol{k}}\right\rangle$ is given by, in plane wave representation,

$$\begin{bmatrix} \sum_{\boldsymbol{G}_m} V_{\text{Hartree}}\left(\boldsymbol{G}_m\right)\mathrm{e}^{i\boldsymbol{G}_m\cdot\boldsymbol{r}}c_{n,\boldsymbol{k}}\left(\boldsymbol{G}_1\right) \\ \sum_{\boldsymbol{G}_m} V_{\text{Hartree}}\left(\boldsymbol{G}_m\right)\mathrm{e}^{i\boldsymbol{G}_m\cdot\boldsymbol{r}}c_{n,\boldsymbol{k}}\left(\boldsymbol{G}_2\right) \\ \vdots \\ \sum_{\boldsymbol{G}_m} V_{\text{Hartree}}\left(\boldsymbol{G}_m\right)\mathrm{e}^{i\boldsymbol{G}_m\cdot\boldsymbol{r}}c_{n,\boldsymbol{k}}\left(\boldsymbol{G}_{N_{\text{PW}}}\right) \end{bmatrix}. \tag{4-38}$$

In reality, one tends to simplify the above calculation through Fourier transforms. A convolution operation in reciprocal space is equivalent to a multiplication operation in real space. Unless for the sake of theoretical demonstration, it is not encouraged to use the expression (4-38). Rather, one tends to adopt the following intricate (but efficient!) procedure. $V_{\text{Hartree}}\left(\boldsymbol{G}\right)$ is first calculated in the reciprocal space, through equation (4-34). Subsequently, $V_{\text{Hartree}}\left(\boldsymbol{G}\right)$ is converted into $V_{\text{Hartree}}\left(\boldsymbol{r}\right)$ through an inverse Fourier transform. It is then straightforward to obtain $V_{\text{Hartree}}\left(\boldsymbol{r}\right)\psi_{n,\boldsymbol{k}}\left(\boldsymbol{r}\right)$ at all the real space grid points, through the simple multiplication operation. A final Fourier transform yields the reciprocal space representation of $\widehat{V}_{\text{Hartree}}\left|\psi_{n,\boldsymbol{k}}\right\rangle$. In a practical code, the Hartree potential is only stored on the real space grid points.

We now start Task-II for the Hartree potential part, which is rather simple since $n(r)$ is at our hand. The total Hartree energy is conveniently expressed in real space as

$$E_{\text{Hartree}} = \frac{1}{2}\int_{\Omega_{\text{cell}}} \mathrm{d}\boldsymbol{r}\, V_{\text{Hartree}}\left(\boldsymbol{r}\right)n\left(\boldsymbol{r}\right) \tag{4-39}$$

where the factor 1/2 is essential for the elimination of double counting. This formally finishes Task-II, but it is actually not the case in practical situations. One still needs the reciprocal space expression for E_{Hartree}, because the total energy consists of various types of potential energies, and other potential energies may be more easily evaluated in the reciprocal space. Meanwhile, there is a cancellation of divergent terms within the reciprocal space, which requires the contribution from the Hartree term in the reciprocal space. Hence, E_{Hartree} is first expanded in terms of reciprocal space lattice vectors as

$$\begin{aligned} E_{\text{Hartree}} &= \frac{1}{2}\int_{\Omega_{\text{cell}}} \mathrm{d}\boldsymbol{r}\, V_{\text{Hartree}}\left(\boldsymbol{r}\right)n\left(\boldsymbol{r}\right) \\ &= \frac{1}{2}\int_{\Omega_{\text{cell}}} \mathrm{d}\boldsymbol{r}\left[\sum_{\boldsymbol{G}_m} V_{\text{Hartree}}\left(\boldsymbol{G}_m\right)\mathrm{e}^{i\boldsymbol{G}_m\cdot\boldsymbol{r}}\right]\left[\sum_{\boldsymbol{G}_{m'}} n\left(\boldsymbol{G}_{m'}\right)\mathrm{e}^{i\boldsymbol{G}_{m'}\cdot\boldsymbol{r}}\right] \\ &= \frac{1}{2}\sum_{\boldsymbol{G}_m}\sum_{\boldsymbol{G}_{m'}} V_{\text{Hartree}}\left(\boldsymbol{G}_m\right)n\left(\boldsymbol{G}_{m'}\right)\int_{\Omega_{\text{cell}}} \mathrm{e}^{i\left(\boldsymbol{G}_m+\boldsymbol{G}_{m'}\right)\cdot\boldsymbol{r}}\mathrm{d}\boldsymbol{r} \\ &= \frac{1}{2}\sum_{\boldsymbol{G}_m}\sum_{\boldsymbol{G}_{m'}} V_{\text{Hartree}}\left(\boldsymbol{G}_m\right)n\left(\boldsymbol{G}_{m'}\right)\Omega_{\text{cell}}\delta_{\boldsymbol{G}_m,-\boldsymbol{G}_{m'}} \\ &= \frac{\Omega_{\text{cell}}}{2}\sum_{\boldsymbol{G}_m\neq 0} V_{\text{Hartree}}\left(\boldsymbol{G}_m\right)n\left(-\boldsymbol{G}_m\right) = 2\pi\Omega_{\text{cell}}\sum_{\boldsymbol{G}_m\neq 0}\frac{\left|n\left(\boldsymbol{G}_m\right)\right|^2}{\left|\boldsymbol{G}_m\right|^2} \end{aligned} \tag{4-40}$$

where equation (4-34) has been used. Besides, the electron density value n must be real, satisfying $n\left(-\boldsymbol{G}_m\right) = n^*\left(\boldsymbol{G}_m\right)$ when expressed in the reciprocal space, according to the theory of Fourier transform. Note that $\left|\boldsymbol{G}_m\right| = 0$ (Γ point of the Brillouin zone) is a special case that is excluded here; otherwise $V_{\text{Hartree}}\left(\boldsymbol{G}_m\right)$ diverges. It is temporarily assumed that $V_{\text{Hartree}}\left(\boldsymbol{G}_m = 0\right) = 0$, but actually the corresponding energy term will be cancelled by the local part of the pseudopotential and the $\left|\boldsymbol{G}_m\right| = 0$ term in E_{II}. We shall come to this point later. In equation (4-40), $\boldsymbol{G}_m$ spans over the entire range of $\left|\boldsymbol{G}\right| \leqslant 2G_{\text{cut}}$. Consequently, for the sake of accuracy, the Fourier expansion of the Hartree potential ought to include all those $\boldsymbol{G}$ with $\left|\boldsymbol{G}\right| \leqslant 2G_{\text{cut}}$. However, for Task-I, one only uses the $\left|\boldsymbol{G}+\boldsymbol{k}\right| \leqslant G_{\text{cut}}$ mesh in transforming $\widehat{V}_{\text{Hartree}}\left(\boldsymbol{r}\right)\psi_{n,\boldsymbol{k}}\left(\boldsymbol{r}\right)$ back to the reciprocal space.

4.2.3. Exchange-correlation energy.

The exchange-correlation potential is the functional derivative of E_{XC} with respect to the electron density $n(r)$

$$V_{\text{XC}}\left(\boldsymbol{r}\right) = \frac{\delta E_{\text{XC}}}{\delta n\left(\boldsymbol{r}\right)}. \tag{4-41}$$

Common LDA and GGA functionals all possess their analytical expressions for the exchange-correlation potential [42, 52, 105]. However, one still needs to transform $V_{\text{XC}}\left(\boldsymbol{r}\right)$ into the reciprocal space as $V_{\text{XC}}\left(\boldsymbol{G}\right)$. $V_{\text{XC}}\left(\boldsymbol{r}\right)$ is typically a non-linear function, which should require Fourier components beyond $2G_{\text{cut}}$ if it is to be calculated from the electron density. Yet, in constructing the Hamiltonian, one merely needs those $\boldsymbol{G}$ values with $\left|\boldsymbol{G}+\boldsymbol{k}\right| \leqslant G_{\text{cut}}$, thus the loss of accuracy here is tolerable. Plane wave components with even higher kinetic energies will still be neglected. Hence, $V_{\text{XC}}\left(\boldsymbol{r}\right)$ should be evaluated on real space grid points, which is timed by $\psi_{n,\boldsymbol{k}}\left(\boldsymbol{r}\right)$ to yield $V_{\text{XC}}\left(\boldsymbol{r}\right)\psi_{n,\boldsymbol{k}}\left(\boldsymbol{r}\right)$. This term is subsequently transformed to the reciprocal space using the $\left|\boldsymbol{G}+\boldsymbol{k}\right| \leqslant G_{\text{cut}}$ grid. This completes Task-I. For Task-II, it is straightforward to obtain

$$E_{\text{XC}} = \int_{\Omega_{\text{cell}}} d\boldsymbol{r}\epsilon_{\text{XC}}\left(n\left(\boldsymbol{r}\right)\right)n\left(\boldsymbol{r}\right). \tag{4-42}$$

4.2.4. Contribution from the pseudopotential.

Then it comes to the interaction between ions and electrons. In this review, we only focus on pseudopotential calculations rather than all-electron calculations, but it is crucial to distinguish two fundamentally distinct types of pseudopotentials that regrettably share the same nomenclature. The pseudopotentials discussed in section 3 refer to atomic pseudopotentials, whose central component is the spherical radial function $R_l(r)$. However, the collective potential experienced by a Bloch electron in a solid arises from the superposition of these atomic pseudopotentials, forming a global pseudopotential. Consequently, the atomic structure of the solid plays an essential role in this construction. Take SrTiO_3 as an example. It was reported that this material takes a tetragonal $I4/mcm$ symmetry at 77 K [106]. Yet, at room temperature it is well-known to exhibit the cubic perovskite structure with $Pm\bar{3}m$ space group. This necessitates computational modeling of $\mathrm{SrTiO_3}$ in both $I4/mcm$ and $Pm\bar{3}m$ configurations. Even if the Sr, Ti and O atomic pseudopotentials are taken exactly the same, the two calculations would involve distinct versions of global 'solid-state' pseudopotentials, due to the structural discrepancy. In this sense, an atomic pseudopotential only reflects the basic 'form' what a global pseudopotential should be like, while the 'structure' of the solid dictates how these atomic components coalesce to yield the global pseudopotential of the solid.

Fortunately, there is an elegant solution to bridge the atomic pseudopotentials and the global pseudopotential. Let κ denotes the type of elements in the solid, and various atoms of the same element could be discriminated through a subscript ω. The location of an atom may therefore by denoted by a vector $\boldsymbol{\tau}_{\kappa,\omega}$. The bare pseudopotentials yield, in the solid, a potential term

$$V^{\mathrm{ps}}(\boldsymbol{r}) = \sum_{\kappa}\sum_{\omega}\sum_{\boldsymbol{T}} V^{\kappa}\left(\boldsymbol{r} - \boldsymbol{\tau}_{\kappa,\omega} - \boldsymbol{T}\right) \tag{4-43}$$

where $\boldsymbol{T}$ covers all translations based on the Bravais lattice. In the example of cubic $\mathrm{SrTiO_3}$, this global pseudopotential is specifically formulated as

$$\begin{aligned} V^{\mathrm{ps}}(\boldsymbol{r}) = \sum_{\boldsymbol{T}} \big[& V^{\mathrm{Sr}}\left(\boldsymbol{r} - \boldsymbol{\tau}_{\mathrm{Sr},1} - \boldsymbol{T}\right) + V^{\mathrm{Ti}}\left(\boldsymbol{r} - \boldsymbol{\tau}_{\mathrm{Ti},1} - \boldsymbol{T}\right) \\ & + V^{\mathrm{O}}\left(\boldsymbol{r} - \boldsymbol{\tau}_{\mathrm{O},1} - \boldsymbol{T}\right) + V^{\mathrm{O}}\left(\boldsymbol{r} - \boldsymbol{\tau}_{\mathrm{O},2} - \boldsymbol{T}\right) \\ & + V^{\mathrm{O}}\left(\boldsymbol{r} - \boldsymbol{\tau}_{\mathrm{O},3} - \boldsymbol{T}\right) \big] \end{aligned} \tag{4-44}$$

because its unit cell consists of three O atoms but only one for either Sr or Ti. The sum over $\boldsymbol{T}$ means that, the variable $\boldsymbol{r}$ in equation (4-43) spans the entire volume of the crystal, and the expression can be transformed into reciprocal space as

$$\begin{aligned} V^{\mathrm{ps}}(\boldsymbol{G}) &= \frac{1}{N_{\mathrm{cell}}\Omega_{\mathrm{cell}}} \int_{\infty} \mathrm{d}\boldsymbol{r} V^{\mathrm{ps}}(\boldsymbol{r})\, e^{-i\boldsymbol{G}\cdot\boldsymbol{r}} \\ &= \frac{1}{N_{\mathrm{cell}}\Omega_{\mathrm{cell}}} \sum_{\kappa}\sum_{\omega}\sum_{T} \int_{\infty} \mathrm{d}\boldsymbol{r}\, e^{-i\boldsymbol{G}\cdot\boldsymbol{r}} V^{\kappa}\left(\boldsymbol{r} - \boldsymbol{\tau}_{\kappa,\omega} - \boldsymbol{T}\right) \end{aligned} \tag{4-45}$$

where Ω_{cell} is the unit cell volume, and N_{cell} is the number of such unit cells in the crystal. With a simple coordinate transformation

$$\boldsymbol{r}' = \boldsymbol{r} - \boldsymbol{T} \tag{4-46}$$

it follows that

$$\begin{aligned} V^{\mathrm{ps}}(\boldsymbol{G}) &= \frac{1}{N_{\mathrm{cell}}\Omega_{\mathrm{cell}}} \sum_{\kappa}\sum_{\omega}\sum_{T} \int_{\infty} \mathrm{d}\boldsymbol{r}' \left(e^{-i\boldsymbol{G}\cdot\boldsymbol{r}'} e^{-i\boldsymbol{G}\cdot\boldsymbol{T}} \right) V^{\kappa}\left(\boldsymbol{r}' - \boldsymbol{\tau}_{\kappa,\omega}\right) \\ &= \frac{1}{\Omega_{\mathrm{cell}}} \sum_{\kappa}\sum_{\omega} \int_{\Omega_{\mathrm{cell}}} \mathrm{d}\boldsymbol{r}' V^{\kappa}\left(\boldsymbol{r}' - \boldsymbol{\tau}_{\kappa,\omega}\right) e^{-i\boldsymbol{G}\cdot\boldsymbol{r}'} \end{aligned} \tag{4-47}$$

because of the fundamental relation $\exp\left(i\boldsymbol{G}\cdot\boldsymbol{T}\right) = 1$. The procedure above not only eliminates the $1/N_{\mathrm{cell}}$ factor, but also confines the integration domain to within a single unit cell. A second coordinate transformation should help to eliminate the summation over ω as follows. Let

$$\boldsymbol{r}'' = \boldsymbol{r}' - \boldsymbol{\tau}_{\kappa,\omega}. \tag{4-48}$$

It follows that

$$\begin{aligned} V^{\mathrm{ps}}(\boldsymbol{G}) &= \frac{1}{\Omega_{\mathrm{cell}}} \sum_{k}\sum_{\omega} e^{-i\boldsymbol{G}\cdot\boldsymbol{\tau}_{\kappa,\omega}} \int_{\Omega_{\mathrm{cell}}} \mathrm{d}\boldsymbol{r}' V^{\kappa}\left(\boldsymbol{r}' - \boldsymbol{\tau}_{\kappa,\omega}\right) e^{-i\boldsymbol{G}\cdot\boldsymbol{r}'} \mathrm{e}^{i\boldsymbol{G}\cdot\boldsymbol{\tau}_{\kappa,\omega}} \\ &= \frac{1}{\Omega_{\mathrm{cell}}} \sum_{k}\sum_{\omega} e^{-i\boldsymbol{G}\cdot\boldsymbol{\tau}_{\kappa,\omega}} \int_{\Omega_{\mathrm{cell}}} \mathrm{d}\boldsymbol{r}'' V^{\kappa}\left(\boldsymbol{r}''\right) e^{-i\boldsymbol{G}\cdot\boldsymbol{r}''} \\ &= \frac{1}{\Omega_{\mathrm{cell}}} \sum_{k}\sum_{\omega} e^{-i\boldsymbol{G}\cdot\boldsymbol{\tau}_{\kappa,\omega}} \int_{\Omega_{\mathrm{cell}}} \mathrm{d}\boldsymbol{r} V^{\kappa}(\boldsymbol{r})\, e^{-i\boldsymbol{G}\cdot\boldsymbol{r}} \end{aligned} \tag{4-49}$$

where the last equality is nothing but recovering the dummy symbol to $\boldsymbol{r}$, from $\boldsymbol{r}''$. If one introduces

$$S^{\kappa}(\boldsymbol{G}) = \sum_{\omega} e^{-i\boldsymbol{G}\cdot\boldsymbol{\tau}_{\kappa,\omega}} \tag{4-50}$$

named the 'structure factor', and a 'form factor' (γ is temporarily regarded as an arbitrary scaling factor)

$$V^{\kappa}(\boldsymbol{G}) = \frac{\gamma}{\Omega_{\mathrm{cell}}} \int_{\Omega_{\mathrm{cell}}} \mathrm{d}\boldsymbol{r} V^{\kappa}(\boldsymbol{r})\, e^{-i\boldsymbol{G}\cdot\boldsymbol{r}} \tag{4-51}$$

then equation (4-49) is rephrased as

$$V^{\mathrm{ps}}(\boldsymbol{G}) = \sum_{\kappa} \frac{S^{\kappa}(\boldsymbol{G})\, V^{\kappa}(\boldsymbol{G})}{\gamma}. \tag{4-52}$$

Of course, 'S' abbreviates 'structure', while 'V' is the conventional symbol to represent a potential. Note that γ cannot be moved outside the summation over κ, since there is no guarantee that γ should be independent of the species. Hence, one should explicitly write $\gamma = \gamma_{\kappa}$. Yet, the standard notation in solid-state theory is to define another volume variable that is element-sensitive,

$$\Omega^{\kappa} = \left[\frac{\int_{\infty} \mathrm{d}\boldsymbol{r} V^{\kappa}(\boldsymbol{r})\, e^{-i\boldsymbol{G}\cdot\boldsymbol{r}}}{\gamma_{\kappa} \int_{\Omega_{\mathrm{cell}}} \mathrm{d}\boldsymbol{r} V^{\kappa}(\boldsymbol{r})\, e^{-i\boldsymbol{G}\cdot\boldsymbol{r}}} \right] \Omega_{\mathrm{cell}} \tag{4-53}$$

such that

$$V^{\kappa}(\boldsymbol{G}) = \frac{1}{\Omega^{\kappa}} \int_{\infty} \mathrm{d}\boldsymbol{r} V^{\kappa}(\boldsymbol{r})\, e^{-i\boldsymbol{G}\cdot\boldsymbol{r}}. \tag{4-54}$$

A comparison between equations (4-51) and (4-54) immediately reveals the functionality of Ω^{κ}. The original formula for $V^{\kappa}(\boldsymbol{G})$ involves an integral over a unit cell of the solid, but $V^{\kappa}(\boldsymbol{r})$ is an atomic potential that does not fit the shape of the unit cell. With the assistance of Ω^{κ}, the integral can be carried out over the entire real space, facilitating the Fourier transformation of the atomic potential $V^{\kappa}(\boldsymbol{r})$. And now the reciprocal space representation of V^{ps} becomes

$$V^{\mathrm{ps}}(\boldsymbol{G}) = \sum_{\kappa} \frac{\Omega^{\kappa}}{\Omega_{\mathrm{cell}}} S^{\kappa}(\boldsymbol{G})\, V^{\kappa}(\boldsymbol{G}). \tag{4-55}$$

Proper choices of γ_κ for all elements, or Ω^κ as defined in equation (4-53), could render $V^\kappa(\boldsymbol{G})$ independent of the crystal structure, as explained in Martin's classic book [107]. The separation between the structure factor $S^\kappa(\boldsymbol{G})$ and the form factor $V^\kappa(\boldsymbol{G})$, which provides significant theoretical and computational advantages, is extensively utilized in electronic structure calculations. To sum up, a pseudopotential in reciprocal space is related to the structure factors $S^\kappa(\boldsymbol{G})$ as well as form factors $V^\kappa(\boldsymbol{G})$ for various elements. Since there is no difficulty in obtaining $S^\kappa(\boldsymbol{G})$ as long as the crystal structure is given, the main focus in this subsection has shifted from the pseudopotential to the form factor. This simplification renders the theoretical framework developed in Chapter 3 directly applicable to the current analysis.

In the following discussions, we shall treat the local part $V_{\text{local}}(\boldsymbol{G})$ and the non-local part $V_{\text{NL}}(\boldsymbol{Q},\boldsymbol{Q}')$ separately, where $\boldsymbol{Q}=\boldsymbol{k}+\boldsymbol{G}$ and $\boldsymbol{Q}'=\boldsymbol{k}+\boldsymbol{G}'$. With the plane-wave bases, a function under real radial grid can be transformed to a new form in the reciprocal space under regular grid, through spherical Fourier transform

$$V^\kappa_{\text{local}}(\boldsymbol{G}) = V^\kappa_{\text{local}}(|\boldsymbol{G}|) = \frac{4\pi}{\Omega^\kappa}\int_0^\infty r^2 \mathrm{d}r\, j_0(|\boldsymbol{G}|r)\, V^\kappa(r). \tag{4-56}$$

Since $V^\kappa_{\text{local}}(r)$ is a spherical function and is independent of the angular momentum state, only the zeroth order spherical Bessel function $j_0(x)=\sin(x)/x$ is involved in the integral. The above expression indicates that, for all $\boldsymbol{G}$ values with the same modulus $|\boldsymbol{G}|$, only one-time calculation is necessary. Given a cubic equal-spacing grid in reciprocal space, then the condition $|\boldsymbol{G}|\leqslant 2G_{\text{cut}}$ points to a sphere inside the box. The number of possible $\boldsymbol{G}$ values is proportional to $4\pi(2G_{\text{cut}})^3/3 = 32\pi G^3_{\text{cut}}/3$, but the number of possible $|\boldsymbol{G}|$ values is proportional to the radius $2G_{\text{cut}}$. Hence, as a rough estimation, the number of possible magnitudes of $\boldsymbol{G}$ is approximately $16\pi G^2_{\text{cut}}/3$ times $|\boldsymbol{G}|$.

Suppose a nuclear potential of the form

$$V^\kappa_{\text{nuclear}}(r) = Z^\kappa_{\text{nuclear}}/r \tag{4-57}$$

is under consideration. It maps into the reciprocal space as

$$V^\kappa_{\text{nuclear}}(\boldsymbol{G}) = \begin{cases} -\left(\frac{4\pi}{\Omega^\kappa}\right)\frac{Z^\kappa_{\text{nuclear}}}{|\boldsymbol{G}|^2}, & \boldsymbol{G}\neq 0; \\ 0, & \boldsymbol{G}=0. \end{cases} \tag{4-58}$$

Note that this expression is not derived through spherical Bessel functions, due to the existence of the divergent term. Rather, it is derived through the Poisson equation $\nabla^2 V(\boldsymbol{r}) = -4\pi n(\boldsymbol{r})$. Here the point charge is $n^\kappa_{\text{nuclear}}(r) = Z^\kappa_{\text{nuclear}}\delta(r)$. After Fourier transform, $n^\kappa_{\text{nuclear}}(\boldsymbol{G}) = Z^\kappa_{\text{nuclear}}/\Omega^\kappa$, and the Poisson equation in the reciprocal space yields $V^\kappa_{\text{nuclear}}(\boldsymbol{G}) = -4\pi Z^\kappa_{\text{nuclear}}/(\Omega^\kappa|\boldsymbol{G}|^2)$.

The local part of the pseudopotential is written in reciprocal space as

$$V^{\text{ps}}_{\text{local}}(\boldsymbol{G}) = \sum_\kappa \frac{\Omega^\kappa}{\Omega_{\text{cell}}} S^\kappa(\boldsymbol{G})\, V^\kappa_{\text{local}}(\boldsymbol{G}) \tag{4-59}$$

and the matrix element, with respect to the plane wave basis set, is

$$\langle \phi_{\boldsymbol{G}+\boldsymbol{k}} | V^{\text{ps}}_{\text{local}} | \phi_{\boldsymbol{G}'+\boldsymbol{k}} \rangle = \sum_{\boldsymbol{G}_m}\sum_\kappa \frac{\Omega^\kappa}{\Omega_{\text{cell}}} S^\kappa(\boldsymbol{G}_m)\, V^\kappa_{\text{local}}(\boldsymbol{G}_m)\, \delta_{\boldsymbol{G}-\boldsymbol{G}',\boldsymbol{G}_m}. \tag{4-60}$$

Like the Hartree potential term, a direct reciprocal space representation of $V^{\text{ps}}_{\text{local}}$ is complicated. Consequently, $V^{\text{ps}}_{\text{local}}(\boldsymbol{r})$ is first obtained through an inverse Fourier transform, and the grid corresponding to $|\boldsymbol{G}|\leqslant 2G_{\text{cut}}$ should be used to avoid wrap-around error. Subsequently, $V^{\text{ps}}_{\text{local}}(\boldsymbol{r})$ is multiplied by $\psi_{n,\boldsymbol{k}}(\boldsymbol{r})$ at each real space grid point. Finally, $V^{\text{ps}}_{\text{local}}(\boldsymbol{r})\,\psi_{n,\boldsymbol{k}}(\boldsymbol{r})$ is transformed back to the reciprocal space to yield $V^{\text{ps}}_{\text{local}}(\boldsymbol{G}_m)\,\psi_{n,\boldsymbol{k}}(\boldsymbol{G}_m)$. A grid with $|\boldsymbol{G}_m+\boldsymbol{k}|\leqslant G_{\text{cut}}$ grid is sufficient for this Fourier transform step.

The divergence difficulty of $V_{\text{Hartree}}(\boldsymbol{G}=0)$ has already been mentioned previously. The same problem exists for $V^\kappa_{\text{local}}(\boldsymbol{G}=0)$, and we may temporarily set $V^\kappa_{\text{local}}(\boldsymbol{G}=0)=0$. A rigorous solution is only reached after introducing the treatment of ion-ion interaction energy term (as shown in section 4.2.5).

The local part of the pseudopotential has a contribution to the total energy as

$$E^{\text{ps}}_{\text{local}} = \int_{\Omega_{\text{cell}}} V^{\text{ps}}_{\text{local}}(\boldsymbol{r})\, n(\boldsymbol{r})\, \mathrm{d}\boldsymbol{r} \tag{4-61}$$

which is a real space expression. Like the Hartree energy, its contribution may be decomposed in terms of reciprocal space $\boldsymbol{G}_m$ as

$$\begin{aligned} E^{\text{ps}}_{\text{local}} &= \int_{\Omega_{\text{cell}}} V^{\text{ps}}_{\text{local}}(\boldsymbol{r})\, n(\boldsymbol{r})\, \mathrm{d}\boldsymbol{r} \\ &= \int_{\Omega_{\text{cell}}} \left[\sum_{\boldsymbol{G}_m} V^{\text{ps}}_{\text{local}}(\boldsymbol{G}_m)\, \mathrm{e}^{i\boldsymbol{G}_m\cdot\boldsymbol{r}}\right]\left[\sum_{\boldsymbol{G}_{m'}} n(\boldsymbol{G}_{m'})\, \mathrm{e}^{i\boldsymbol{G}_{m'}\cdot\boldsymbol{r}}\right]\mathrm{d}\boldsymbol{r} \\ &= \Omega_{\text{cell}}\sum_{\boldsymbol{G}_m}\sum_{\boldsymbol{G}_{m'}} V^{\text{ps}}_{\text{local}}(\boldsymbol{G}_m)\, n(\boldsymbol{G}_{m'})\, \delta_{\boldsymbol{G}_m,-\boldsymbol{G}_{m'}} \\ &= \Omega_{\text{cell}}\sum_{\boldsymbol{G}_m\neq 0} S^\kappa(\boldsymbol{G}_m)\, V^\kappa_{\text{local}}(\boldsymbol{G}_m)\, n(-\boldsymbol{G}_m). \end{aligned} \tag{4-62}$$

Up till now, neither Task-I nor Task-II has been finished, because the non-local part of the pseudopotential is not taken into account yet. This term is far more complicated to handle compared with the local part. Here we take the ONCV pseudopotential in equation (3-158) as an example to illustrate the non-local pseudopotential operator in the Hamiltonian. In the pseudopotential file, only the radial part of the projector function $\tilde{\chi}^\kappa_{lm,i}(\boldsymbol{r})$ is stored, which is denoted by $\tilde{R}^\kappa_{l,i}(\boldsymbol{r})$. The subscript i denotes the ith reference energy under angular quantum number l. A radial Fourier transform of $\tilde{R}^{\kappa}_{l,i}(\boldsymbol{r})$ is achieved through equation (3-131). For notation convenience, we use $\boldsymbol{Q}=\boldsymbol{k}+\boldsymbol{G}$. Then the Fourier transform is expressed as

$$P^{\kappa}_{l,i}(|\boldsymbol{Q}|)=4\pi\int_{0}^{\infty} r^{2}\mathrm{d}r\, j_{l}(|\boldsymbol{Q}|r)\,\tilde{R}^{\kappa}_{l,i}(r) \tag{4-63}$$

which, timed by the angular part $(-i)^{l}Y_{lm}\left(\widehat{\boldsymbol{Q}}\right)$ and the structure factor $S^{\kappa}(\boldsymbol{Q})=\sum_{\omega}e^{-i\boldsymbol{Q}\cdot\boldsymbol{\tau}_{\kappa,\omega}}$, gives the reciprocal space representation of $\tilde{\chi}^{\kappa}_{lm,i}(\boldsymbol{r})$

$$X^{\kappa}_{lm,i}(\boldsymbol{Q})=(-i)^{l}P^{\kappa}_{l,i}(|\boldsymbol{Q}|)\,Y_{lm}\left(\widehat{\boldsymbol{Q}}\right)\,S^{\kappa}(\boldsymbol{Q}). \tag{4-64}$$

Here, $\widehat{\boldsymbol{Q}}$ is the unit vector along the direction of $\boldsymbol{Q}$

$$\widehat{\boldsymbol{Q}}=\frac{\boldsymbol{Q}}{|\boldsymbol{Q}|} \tag{4-65}$$

which retains the angular information $(\theta_{\boldsymbol{Q}},\varphi_{\boldsymbol{Q}})$. Consider, for example, a primitive cell of metal Mg that contains two Mg atoms. Their coordinates are denoted by $\boldsymbol{\tau}_1$ and $\boldsymbol{\tau}_2$, respectively. The structure factor is $S^{\mathrm{Mg}}=e^{-i\boldsymbol{Q}\cdot\boldsymbol{\tau}_1}+e^{-i\boldsymbol{Q}\cdot\boldsymbol{\tau}_2}$. While the 3s electrons are the nominal valence electrons for Mg, at least the 2p electrons should be included in the valence for a practical Mg pseudopotential. This is because Mg usually appears as Mg^{2+} in solids, and the 2p electrons are the outermost exposed electrons for Mg^{2+}. In the ONCV pseudopotential file for Mg, the radial parts of two projector functions are stored for the s state, because two reference energies are involved. Similarly, only two projector functions are stored for the p state. Yet, there are three distinct p states, thus finally eight projector functions, denoted by $\left\{X^{\mathrm{Mg}}_{s,1},\ X^{\mathrm{Mg}}_{s,2},X^{\mathrm{Mg}}_{p_x,1},\ X^{\mathrm{Mg}}_{p_x,2},X^{\mathrm{Mg}}_{p_y,1},\ X^{\mathrm{Mg}}_{p_y,2},X^{\mathrm{Mg}}_{p_z,1},X^{\mathrm{Mg}}_{p_z,2}\right\}$ in reciprocal space, are generated.

Let us further utilize the shorthand notation $\boldsymbol{Q}'=\boldsymbol{k}+\boldsymbol{G}'$. The reciprocal-space matrix elements of the non-local pseudopotential $\widehat{V}_{\mathrm{NL}}$ can therefore be expressed as

$$\langle\phi_{\boldsymbol{Q}}|\sum_{\kappa}\widehat{V}^{\kappa}_{\mathrm{NL}}|\phi_{\boldsymbol{Q}'}\rangle=\sum_{\kappa}\sum_{l,m}\sum_{i}\langle\phi_{\boldsymbol{Q}}|X^{\kappa}_{lm,i}\rangle\frac{1}{\tilde{b}^{\kappa}_{l,i}}\langle X^{\kappa}_{lm,i}|\phi_{\boldsymbol{Q}'}\rangle. \tag{4-66}$$

While this expression appears formally complicated due to its nested summations, one may select only one orbital of one particular element for inspection,

$$\begin{aligned}&\sum_{i}\langle\phi_{\boldsymbol{Q}}|X^{\kappa}_{lm,i}\rangle\frac{1}{\tilde{b}^{\kappa}_{l,i}}\langle X^{\kappa}_{lm,i}|\phi_{\boldsymbol{Q}'}\rangle\\&\quad=\left\langle\phi_{\boldsymbol{Q}}\middle|(-i)^{l}P^{\kappa}_{l,1}Y_{lm}S^{\kappa}\right\rangle\frac{1}{\tilde{b}^{\kappa}_{l,1}}\left\langle(-i)^{l}P^{\kappa}_{l,1}Y_{lm}S^{\kappa}\middle|\phi_{\boldsymbol{Q}'}\right\rangle\\&\qquad+\left\langle\phi_{\boldsymbol{Q}}\middle|(-i)^{l}P^{\kappa}_{l,2}Y_{lm}S^{\kappa}\right\rangle\frac{1}{\tilde{b}^{\kappa}_{l,2}}\left\langle(-i)^{l}P^{\kappa}_{l,2}Y_{lm}S^{\kappa}\middle|\phi_{\boldsymbol{Q}'}\right\rangle.\end{aligned} \tag{4-67}$$

Note that for a given atomic site and specific l, m values, the ONCV pseudopotential involves two reference energies, corresponding to two projector functions. Hence, there are two terms in equation (4-67), involving $\left|\cdots P^{\kappa}_{l,1}\cdots\right\rangle\left\langle\cdots P^{\kappa}_{l,1}\cdots\right|$ and $\left|\cdots P^{\kappa}_{l,2}\cdots\right\rangle\left\langle\cdots P^{\kappa}_{l,2}\cdots\right|$ respectively.

For example, we consider the eight projector functions of Mg. Performing inner product calculations between $\langle\phi_{\boldsymbol{Q}}|$ and $\left|X^{\mathrm{Mg}}\right\rangle$, as well between $\left\langle X^{\mathrm{Mg}}\right|$ and $|\phi_{\boldsymbol{Q}'}\rangle$, one obtains eight values of $\left\langle\phi_{\boldsymbol{Q}}\middle|X^{\mathrm{Mg}}_{lm,i}\right\rangle$ and eight values of $\left\langle X^{\mathrm{Mg}}_{lm,i}\middle|\phi_{\boldsymbol{Q}'}\right\rangle$. In the ONCV formalism, a pair of $\left\langle\phi_{\boldsymbol{Q}}\middle|X^{\mathrm{Mg}}_{lm,i}\right\rangle$ and $\left\langle X^{\mathrm{Mg}}_{lm,i}\middle|\phi_{\boldsymbol{Q}'}\right\rangle$, further multiplied by $1/\tilde{b}^{\mathrm{Mg}}_{l,i}$, yields a matrix element. Specifically,

$$\begin{aligned}\left\langle\phi_{\boldsymbol{Q}}\middle|\widehat{V}^{\mathrm{Mg}}_{\mathrm{NL}}\middle|\phi_{\boldsymbol{Q}'}\right\rangle&=\left\langle\phi_{\boldsymbol{Q}}\middle|X^{\mathrm{Mg}}_{s,1}\right\rangle\frac{1}{\tilde{b}^{\mathrm{Mg}}_{s,1}}\left\langle X^{\mathrm{Mg}}_{s,1}\middle|\phi_{\boldsymbol{Q}'}\right\rangle\\&\quad+\left\langle\phi_{\boldsymbol{Q}}\middle|X^{\mathrm{Mg}}_{s,2}\right\rangle\frac{1}{\tilde{b}^{\mathrm{Mg}}_{s,2}}\left\langle X^{\mathrm{Mg}}_{s,2}\middle|\phi_{\boldsymbol{Q}'}\right\rangle\\&\quad+\left\langle\phi_{\boldsymbol{Q}}\middle|X^{\mathrm{Mg}}_{p_x,1}\right\rangle\frac{1}{\tilde{b}^{\mathrm{Mg}}_{p,1}}\left\langle X^{\mathrm{Mg}}_{p_x,1}\middle|\phi_{\boldsymbol{Q}'}\right\rangle\\&\quad+\left\langle\phi_{\boldsymbol{Q}}\middle|X^{\mathrm{Mg}}_{p_x,2}\right\rangle\frac{1}{\tilde{b}^{\mathrm{Mg}}_{p,2}}\left\langle X^{\mathrm{Mg}}_{p_x,2}\middle|\phi_{\boldsymbol{Q}'}\right\rangle+\cdots\end{aligned} \tag{4-68}$$

which is a summation over eight terms.

In the ONCV method, the matrix $\boldsymbol{B}^{\kappa}_{lm}$ is diagonal,

$$\boldsymbol{B}^{\kappa}_{lm}=\begin{bmatrix}1/\tilde{b}^{\kappa}_{l,1}&0\\0&1/\tilde{b}^{\kappa}_{l,2}\end{bmatrix}$$

thus no terms like $\left|\cdots P^{\kappa}_{l,1}\cdots\right\rangle\left\langle\cdots P^{\kappa}_{l,2}\cdots\right|$ should emerge. The fact that $\boldsymbol{B}^{\kappa}_{lm}$ is diagonal reflects an additional optimization in the ONCV formalism. In the general case, however, $\boldsymbol{B}^{\kappa}_{lm}$ has off-diagonal elements. In case there are two reference energies, then

$$\boldsymbol{B}^{\kappa}_{lm}=\begin{bmatrix}\boldsymbol{B}^{\kappa}_{lm,11}&\boldsymbol{B}^{\kappa}_{lm,12}\\\boldsymbol{B}^{\kappa}_{lm,21}&\boldsymbol{B}^{\kappa}_{lm,22}\end{bmatrix}. \tag{4-69}$$

And one must resort to

$$\begin{aligned}&\sum_{i,j}\boldsymbol{B}^{\kappa}_{lm,ij}\langle\phi_{\boldsymbol{Q}}|X^{\kappa}_{lm,i}\rangle\langle X^{\kappa}_{lm,j}|\phi_{\boldsymbol{Q}'}\rangle\\&\quad=\boldsymbol{B}^{\kappa}_{lm,11}\left\langle\phi_{\boldsymbol{Q}}\middle|(-i)^{l}P^{\kappa}_{l,1}Y_{lm}S^{\kappa}\right\rangle\left\langle(-i)^{l}P^{\kappa}_{l,1}Y_{lm}S^{\kappa}\middle|\phi_{\boldsymbol{Q}'}\right\rangle\\&\qquad+\boldsymbol{B}^{\kappa}_{lm,12}\left\langle\phi_{\boldsymbol{Q}}\middle|(-i)^{l}P^{\kappa}_{l,1}Y_{lm}S^{\kappa}\right\rangle\left\langle(-i)^{l}P^{\kappa}_{l,2}Y_{lm}S^{\kappa}\middle|\phi_{\boldsymbol{Q}'}\right\rangle\\&\qquad+\boldsymbol{B}^{\kappa}_{lm,21}\left\langle\phi_{\boldsymbol{Q}}\middle|(-i)^{l}P^{\kappa}_{l,2}Y_{lm}S^{\kappa}\right\rangle\left\langle(-i)^{l}P^{\kappa}_{l,1}Y_{lm}S^{\kappa}\middle|\phi_{\boldsymbol{Q}'}\right\rangle\\&\qquad+\boldsymbol{B}^{\kappa}_{lm,22}\left\langle\phi_{\boldsymbol{Q}}\middle|(-i)^{l}P^{\kappa}_{l,2}Y_{lm}S^{\kappa}\right\rangle\left\langle(-i)^{l}P^{\kappa}_{l,2}Y_{lm}S^{\kappa}\middle|\phi_{\boldsymbol{Q}'}\right\rangle.\end{aligned} \tag{4-70}$$

In order to better illustrate the physics using lighter mathematical illustration, we shall focus more on the ONCV pseudopotentials, and $\widehat{V}_{\mathrm{NL}}|\psi_{n,\boldsymbol{k}}\rangle$ is written as

$$\begin{aligned}\widehat{V}_{\mathrm{NL}}\left|\psi_{n,\boldsymbol{k}}\right\rangle &= \sum_{\kappa}\sum_{l,m}\sum_{i}\left|X^{\kappa}_{lm,i}\right\rangle \frac{1}{\tilde{b}^{\kappa}_{l,i}}\left\langle X^{\kappa}_{lm,i}\right|\psi_{n,\boldsymbol{k}}\rangle \\ &= \sum_{\kappa}\sum_{l,m}\sum_{i}\left|X^{\kappa}_{lm,i}\right\rangle \frac{1}{\tilde{b}^{\kappa}_{l,i}}\sum_{\boldsymbol{G}_m} c_{n,\boldsymbol{k}}\left(\boldsymbol{G}_m\right)\left\langle X^{\kappa}_{lm,i}\right|\phi_{\boldsymbol{k}+\boldsymbol{G}_m}\rangle .\end{aligned} \tag{4-71}$$

The computation can be decoupled into two distinct tasks: (i) to compute the inner product $\left\langle X^{\kappa}_{lm,i}\middle|\psi_{n,\boldsymbol{k}}\right\rangle$; (ii) to multiply the value of $\left\langle X^{\kappa}_{lm,i}\middle|\psi_{n,\boldsymbol{k}}\right\rangle$ by the corresponding projector functions $\left|X^{\kappa}_{lm,i}\right\rangle$ as well as $1/\tilde{b}^{\kappa}_{i}$. Evaluation of $\left\langle X^{\kappa}_{lm,i}\middle|\psi_{n,\boldsymbol{k}}\right\rangle$ can be done either in reciprocal space or in real space. While reciprocal space computation aligns naturally with plane wave formalisms, real space implementation offers better computational efficiency due to the localized nature of these projector functions. However, evaluation of $\left\langle X^{\kappa}_{lm,i}\middle|\psi_{n,\boldsymbol{k}}\right\rangle$ in real space incurs nontrivial tradeoffs in coding complexity.

Let us return to the solid metal Mg example. The application of $\widehat{V}_{\mathrm{NL}}$ upon $|\psi_{n,\boldsymbol{k}}\rangle$ is given explicitly by, within the ONCV formalism,

$$\begin{aligned}\widehat{V}^{\mathrm{Mg}}_{\mathrm{NL}}\left|\psi_{n,\boldsymbol{k}}\right\rangle = {}& \frac{\left\langle X^{\mathrm{Mg}}_{s,1}\middle|\psi_{n,\boldsymbol{k}}\right\rangle}{\tilde{b}^{\mathrm{Mg}}_{s,1}}\left|X^{\mathrm{Mg}}_{s,1}\right\rangle + \frac{\left\langle X^{\mathrm{Mg}}_{s,2}\middle|\psi_{n,\boldsymbol{k}}\right\rangle}{\tilde{b}^{\mathrm{Mg}}_{s,2}}\left|X^{\mathrm{Mg}}_{s,2}\right\rangle \\ &+ \frac{\left\langle X^{\mathrm{Mg}}_{p_x,1}\middle|\psi_{n,\boldsymbol{k}}\right\rangle}{\tilde{b}^{\mathrm{Mg}}_{p_x,1}}\left|X^{\mathrm{Mg}}_{p_x,1}\right\rangle \\ &+ \frac{\left\langle X^{\mathrm{Mg}}_{p_x,2}\middle|\psi_{n,\boldsymbol{k}}\right\rangle}{\tilde{b}^{\mathrm{Mg}}_{p_x,2}}\left|X^{\mathrm{Mg}}_{p_x,2}\right\rangle + \frac{\left\langle X^{\mathrm{Mg}}_{p_y,1}\middle|\psi_{n,\boldsymbol{k}}\right\rangle}{\tilde{b}^{\mathrm{Mg}}_{p_y,1}}\left|X^{\mathrm{Mg}}_{p_y,1}\right\rangle \\ &+ \frac{\left\langle X^{\mathrm{Mg}}_{p_y,2}\middle|\psi_{n,\boldsymbol{k}}\right\rangle}{\tilde{b}^{\mathrm{Mg}}_{p_y,2}}\left|X^{\mathrm{Mg}}_{p_y,2}\right\rangle \\ &+ \frac{\left\langle X^{\mathrm{Mg}}_{p_z,1}\middle|\psi_{n,\boldsymbol{k}}\right\rangle}{\tilde{b}^{\mathrm{Mg}}_{p_z,1}}\left|X^{\mathrm{Mg}}_{p_z,1}\right\rangle + \frac{\left\langle X^{\mathrm{Mg}}_{p_z,2}\middle|\psi_{n,\boldsymbol{k}}\right\rangle}{\tilde{b}^{\mathrm{Mg}}_{p_z,2}}\left|X^{\mathrm{Mg}}_{p_z,2}\right\rangle .\end{aligned} \tag{4-72}$$

In the more general case, $\boldsymbol{B}^{\kappa}_{lm}$ is described by equation (4-69), which is not guaranteed to be diagonal. The effect of $\widehat{V}^{\mathrm{Mg}}_{\mathrm{NL}}$ action on $|\psi_{n,\boldsymbol{k}}\rangle$ is

$$\begin{aligned}\widehat{V}^{\mathrm{Mg}}_{\mathrm{NL}}\left|\psi_{n,\boldsymbol{k}}\right\rangle = {}& \left(\boldsymbol{B}^{\mathrm{Mg}}_{s,11}\left\langle X^{\mathrm{Mg}}_{s,1}\middle|\psi_{n,\boldsymbol{k}}\right\rangle + \boldsymbol{B}^{\mathrm{Mg}}_{s,12}\left\langle X^{\mathrm{Mg}}_{s,2}\middle|\psi_{n,\boldsymbol{k}}\right\rangle\right)\left|X^{\mathrm{Mg}}_{s,1}\right\rangle \\ &+ \left(\boldsymbol{B}^{\mathrm{Mg}}_{s,21}\left\langle X^{\mathrm{Mg}}_{s,1}\middle|\psi_{n,\boldsymbol{k}}\right\rangle\right. \\ &\left.+\boldsymbol{B}^{\mathrm{Mg}}_{s,22}\left\langle X^{\mathrm{Mg}}_{s,2}\middle|\psi_{n,\boldsymbol{k}}\right\rangle\right)\left|X^{\mathrm{Mg}}_{s,2}\right\rangle \\ &+ \left(\boldsymbol{B}^{\mathrm{Mg}}_{p_x,11}\left\langle X^{\mathrm{Mg}}_{p_x,1}\middle|\psi_{n,\boldsymbol{k}}\right\rangle\right. \\ &\left.+\boldsymbol{B}^{\mathrm{Mg}}_{p_x,12}\left\langle X^{\mathrm{Mg}}_{p_x,2}\middle|\psi_{n,\boldsymbol{k}}\right\rangle\right)\left|X^{\mathrm{Mg}}_{p_x,1}\right\rangle \\ &+ \left(\boldsymbol{B}^{\mathrm{Mg}}_{p_x,21}\left\langle X^{\mathrm{Mg}}_{p_x,1}\middle|\psi_{n,\boldsymbol{k}}\right\rangle\right. \\ &\left.+\boldsymbol{B}^{\mathrm{Mg}}_{p_x,22}\left\langle X^{\mathrm{Mg}}_{p_x,2}\middle|\psi_{n,\boldsymbol{k}}\right\rangle\right)\left|X^{\mathrm{Mg}}_{p_x,2}\right\rangle + \cdots\end{aligned} \tag{4-73}$$

where remaining terms regarding p_y and p_z states have been omitted for brevity.

Finally, the contribution from the non-local part of the pseudopotential to the total energy is

$$\begin{aligned}E_{\mathrm{NL}} &= N_{\sigma}\sum_{\boldsymbol{k},n} f_{n,\boldsymbol{k}} w_{\boldsymbol{k}}\left\langle\psi_{n,\boldsymbol{k}}\right|\widehat{V}_{\mathrm{NL}}\left|\psi_{n,\boldsymbol{k}}\right\rangle \\ &= N_{\sigma}\sum_{\boldsymbol{k},n} f_{n,\boldsymbol{k}} w_{\boldsymbol{k}}\sum_{\kappa}\sum_{l,m}\sum_{i}\frac{1}{\tilde{b}^{\kappa}_{i}} \\ &\quad\times\left[\sum_{\boldsymbol{G}_m} c_{n,\boldsymbol{k}}\left(\boldsymbol{G}_m\right)\left\langle\phi_{\boldsymbol{k}+\boldsymbol{G}_m}\middle|X^{\kappa}_{lm,i}\right\rangle\right] \\ &\quad\times\left[\sum_{\boldsymbol{G}_{m'}} c_{n,\boldsymbol{k}}\left(\boldsymbol{G}_{m'}\right)\left\langle X^{\kappa}_{lm,i}\middle|\phi_{\boldsymbol{k}+\boldsymbol{G}_{m'}}\right\rangle\right].\end{aligned} \tag{4-74}$$

4.2.5. Ewald summation.

A final but indispensable part of the total energy comes from the ion-ion interaction. While it is essential for Task-II, it has nothing to do with Task-I. Without this term, the Kohn-Sham equations may still be solved, leading to the electronic energy eigenvalues $\varepsilon_{n,\boldsymbol{k}}$. This implies that researchers focusing exclusively on electronic properties may reasonably skip this subsection without compromising the entire computational framework. To delve into the mathematics of this subsection, however, brings about two benefits. On the one hand, the total energy is key to structural optimization, and almost every electronic structure calculation code involves the functionality of structure relaxation. On the other hand, through the derivation in this subsection, one understands how the divergence problem at the Γ point is finally resolved.

The Coulomb interaction energy between ions could be calculated through Ewald summation [108], which is widely applied in calculating the potential due to point charges arranged periodically. The basic idea is to divide the Coulomb potential into a long-range part and a short-range part, which may be evaluated in reciprocal space and in real space, respectively. The ionic Coulomb interaction energy is

$$E_{\mathrm{II}} = \frac{1}{2}\sum_{s,s'} Z_s Z_{s'}\sum_{\mathbf{T}}{}^{\prime}\frac{1}{\left|\boldsymbol{\tau}_{s,s'}-\mathbf{T}\right|} \tag{4-75}$$

where Z_s is the charge carried by the ion at location $\boldsymbol{\tau}_s$, and $\boldsymbol{\tau}_{s,s'} = \boldsymbol{\tau}_{s'} - \boldsymbol{\tau}_s$. Here the prime mark on top of the second summation symbol means that the $\boldsymbol{T} = 0$, $s = s'$ term should be excluded. The ion-ion interaction energy is expressed as

$$\begin{aligned}E_{\mathrm{II}} = {}& \frac{1}{2}\sum_{s,s'} Z_s Z_{s'}\sum_{\mathbf{T}}{}^{\prime}\frac{\operatorname{erfc}\left(\eta\left|\boldsymbol{\tau}_{s,s'}-\mathbf{T}\right|\right)}{\left|\boldsymbol{\tau}_{s,s'}-\mathbf{T}\right|} \\ &+ \frac{1}{2}\sum_{s,s'} Z_s Z_{s'}\frac{4\pi}{\Omega_{\mathrm{cell}}}\sum_{\boldsymbol{G}}\frac{1}{\left|\boldsymbol{G}\right|^2}e^{-\frac{|\boldsymbol{G}|^2}{4\eta^2}}\cos\left(\boldsymbol{G}\cdot\boldsymbol{\tau}_{s,s'}\right) \\ &- \frac{1}{2}\left[\sum_{s} Z_s^2\right]\frac{2\eta}{\sqrt{\pi}}\end{aligned} \tag{4-76}$$

where η is a broadening factor to convert the point charge into a Gaussian distribution of charge at location $\boldsymbol{\tau}_s$, *i.e.* $\left(\eta^2/\pi\right)^{3/2} e^{-\eta^2|\boldsymbol{r}-\boldsymbol{\tau}_s|^2}$. For a detailed derivation of equation (4-76), the reader is encouraged to refer to the work of Lee and Cai [109].

Next, we address the previously mentioned but unresolved issue: the divergence of $V_{\mathrm{Hartree}}(\boldsymbol{G})$, $V^{\kappa}_{\mathrm{local}}(\boldsymbol{G})$ and the reciprocal term of E_{II} when $\boldsymbol{G}=0$. First introduce a positive compensating charge

$$n_{\mathrm{aux}}(\boldsymbol{r}) = -\sum_s Z_s \left(\frac{\eta^2}{\pi}\right)^{3/2} e^{-2\eta^2|\boldsymbol{r}-\boldsymbol{\tau}_s|^2} \tag{4-77}$$

whose Fourier transform is

$$n_{\mathrm{aux}}(\boldsymbol{G}) = -\frac{1}{\Omega_{\mathrm{cell}}} e^{-|\boldsymbol{G}|^2/8\eta^2} \left[\sum_{\kappa} Z^{\kappa} S^{\kappa}(\boldsymbol{G})\right]. \tag{4-78}$$

We now group E_{Hartree}, the local part of pseudopotential contribution to the total energy, as well as E_{II}, together to obtain

$$\begin{aligned} E_{\mathrm{es}} &= E_{\mathrm{ee}} + E_{\mathrm{ps,local}} + E_{\mathrm{II}} \\ &= \frac{1}{2}\iint \mathrm{d}\boldsymbol{r}\mathrm{d}\boldsymbol{r}' \frac{n(\boldsymbol{r})\, n(\boldsymbol{r}')}{|\boldsymbol{r}-\boldsymbol{r}'|} + \int \mathrm{d}\boldsymbol{r} n(\boldsymbol{r}) \sum_{\kappa,s,\mathbf{T}} V^{\kappa}(\boldsymbol{r}-\boldsymbol{\tau}_{\kappa,s}-\mathbf{T}) \\ &\quad + \frac{1}{2}\sum_{s,s'} Z_s Z_{s'} {\sum_{\mathbf{T}}}' \frac{1}{|\boldsymbol{\tau}_{s,s'}-\mathbf{T}|} + \frac{1}{2}\iint \mathrm{d}\boldsymbol{r}\mathrm{d}\boldsymbol{r}' \frac{n_{\mathrm{aux}}(\boldsymbol{r})\, n_{\mathrm{aux}}(\boldsymbol{r}')}{|\boldsymbol{r}-\boldsymbol{r}'|} \\ &\quad - \frac{1}{2}\iint \mathrm{d}\boldsymbol{r}\mathrm{d}\boldsymbol{r}' \frac{n_{\mathrm{aux}}(\boldsymbol{r})\, n_{\mathrm{aux}}(\boldsymbol{r}')}{|\boldsymbol{r}-\boldsymbol{r}'|}. \end{aligned} \tag{4-79}$$

Here the last two terms sum up to zero, which are manually added. Let $n_{\mathrm{T}}(\boldsymbol{r}) = n(\boldsymbol{r}) + n_{\mathrm{aux}}(\boldsymbol{r})$, and it follows that

$$\begin{aligned} E_{\mathrm{es}} &= \frac{1}{2}\iint \mathrm{d}\boldsymbol{r}\mathrm{d}\boldsymbol{r}' \frac{n_{\mathrm{T}}(\boldsymbol{r})\, n_{\mathrm{T}}(\boldsymbol{r}')}{|\boldsymbol{r}-\boldsymbol{r}'|} \\ &\quad + \int \mathrm{d}\boldsymbol{r} n(\boldsymbol{r}) \left(\sum_{\kappa,s,\mathbf{T}} V^{\kappa}(\boldsymbol{r}-\boldsymbol{\tau}_{\kappa,s}-\mathbf{T}) - \int \mathrm{d}\boldsymbol{r}' \frac{n_{\mathrm{aux}}(\boldsymbol{r}')}{|\boldsymbol{r}-\boldsymbol{r}'|}\right) \\ &\quad + \frac{1}{2}\left[\sum_{s,s'} Z_s Z_{s'} {\sum_{\mathbf{T}}}' \frac{1}{|\boldsymbol{\tau}_{s,s'}-\mathbf{T}|} - \frac{1}{2}\iint \mathrm{d}\boldsymbol{r}\mathrm{d}\boldsymbol{r}' \frac{n_{\mathrm{aux}}(\boldsymbol{r})\, n_{\mathrm{aux}}(\boldsymbol{r}')}{|\boldsymbol{r}-\boldsymbol{r}'|}\right]. \end{aligned} \tag{4-80}$$

The first term in equation (4-80) can be transformed into the reciprocal space as

$$\frac{1}{2}\iint \mathrm{d}\boldsymbol{r}\mathrm{d}\boldsymbol{r}' \frac{n_{\mathrm{T}}(\boldsymbol{r})\, n_{\mathrm{T}}(\boldsymbol{r}')}{|\boldsymbol{r}-\boldsymbol{r}'|} = \frac{1}{2} 4\pi\, \Omega_{\mathrm{cell}} \sum_{\boldsymbol{G}} \frac{n_{\mathrm{T}}(\boldsymbol{G})^2}{|\boldsymbol{G}|^2}. \tag{4-81}$$

At $\boldsymbol{G}=0$, one has $n_{\mathrm{T}}(\boldsymbol{G}=0) = Q_{\mathrm{T}}/\Omega_{\mathrm{cell}}$, while the total charge Q_{T} in the unit cell is zero.

$$Q_{\mathrm{T}} = \int \mathrm{d}\boldsymbol{r} n_{\mathrm{T}}(\boldsymbol{r}) = \int \mathrm{d}\boldsymbol{r} n(\boldsymbol{r}) + \int \mathrm{d}\boldsymbol{r} n_{\mathrm{aux}}(\boldsymbol{r}) = N_{\mathrm{e}} - N_{\mathrm{e}} = 0. \tag{4-82}$$

Here N_{e} is the total number of valence electrons in a unit cell. Note that the divergent terms cancel altogether.

The second term in equation (4-80) is, after Fourier transform,

$$\begin{aligned} &\int \mathrm{d}\boldsymbol{r}\, n(\boldsymbol{r}) \left(\sum_{\kappa,s,\mathbf{T}} V^{\kappa}(\boldsymbol{r}-\boldsymbol{\tau}_{\kappa,s}-\mathbf{T}) - \int \mathrm{d}\boldsymbol{r}' \frac{n_{\mathrm{aux}}(\boldsymbol{r}')}{|\boldsymbol{r}-\boldsymbol{r}'|}\right) \\ &\quad = \Omega_{\mathrm{cell}} \sum_{\boldsymbol{G}} \left[\sum_{\kappa} \frac{\Omega_{\kappa}}{\Omega_{\mathrm{cell}}} S^{\kappa}(\boldsymbol{G})\, V^{\kappa}_{\mathrm{local}}(\boldsymbol{G}) - \frac{4\pi}{|\boldsymbol{G}|^2} n_{\mathrm{aux}}(\boldsymbol{G})\right] n(\boldsymbol{G}). \end{aligned} \tag{4-83}$$

And the local part of the pseudopotential is expressed as

$$\begin{aligned} V^{\kappa}_{\mathrm{local}}(|\boldsymbol{G}|) = V^{\kappa}_{\mathrm{local}}(G) &= \frac{4\pi}{\Omega^{\kappa}} \int_0^{\infty} r^2 \mathrm{d}r\, j_0(|\boldsymbol{G}|\, r)\, V^{\kappa}_{\mathrm{local}}(r) \\ &= \frac{4\pi}{\Omega^{\kappa}} \int_0^{\infty} r^2 \mathrm{d}r\, j_0(|\boldsymbol{G}|\, r) \left(V^{\kappa}_{\mathrm{local}}(r) + \frac{Z^{\kappa}}{r}\right) \\ &\quad + \frac{4\pi}{\Omega^{\kappa}} \int_0^{\infty} r^2 \mathrm{d}r\, j_0(|\boldsymbol{G}|\, r) \left(-\frac{Z^{\kappa}}{r}\right). \end{aligned} \tag{4-84}$$

At $\boldsymbol{G}=0$, the first term in equation (4-84) is proportional to a constant

$$\alpha^{\kappa} = 4\pi \int_0^{\infty} \mathrm{d}r\, r^2 \left[V^{\kappa}_{\mathrm{local}}(r) - \left(-\frac{Z^{\kappa}}{r}\right)\right]. \tag{4-85}$$

In this case, the structure factor equals the number of atoms under the element in a unit cell, $S^{\kappa}(0) = N^{\kappa}$. The contribution of all atoms to the total energy in this term is $\left(\sum_{\kappa} \alpha^{\kappa} N^{\kappa}\right) n(\boldsymbol{G}=0)$, where $n(\boldsymbol{G}=0) = N_e/\Omega_{\mathrm{cell}}$. The result for the second term in equation (4-84) has already been given as $-4\pi Z^{\kappa}/\left(\Omega^{\kappa}|\boldsymbol{G}|^2\right)$, which still diverges at $\boldsymbol{G}=0$. Perform a Taylor expansion of $n_{\mathrm{aux}}(\boldsymbol{G})$ at $\boldsymbol{G}=0$, and

$$\lim_{|\boldsymbol{G}|\to 0} n_{\mathrm{aux}}(\boldsymbol{G}) = -\frac{Q}{\Omega_{\mathrm{cell}}} + \frac{Q}{8\eta^2 \Omega_{\mathrm{cell}}} |\boldsymbol{G}|^2 \tag{4-86}$$

where $Q = \sum_{\kappa} N^{\kappa} Z^{\kappa} = N_{\mathrm{e}}$. After combining it with the second term in equation (4-84), one arrives at

$$\left(-\sum_{\kappa} N^{\kappa} Z^{\kappa} + Q\right) \frac{4\pi}{|\boldsymbol{G}|^2 \Omega_{\mathrm{cell}}} n(0) - \frac{\pi Q}{2\eta^2 \Omega_{\mathrm{cell}}} n(0). \tag{4-87}$$

The divergent terms cancel out, leaving a final result of $-\frac{1}{2}\left[\sum_s Z_s\right]^2 \frac{\pi}{\eta^2 \Omega_{\mathrm{cell}}}$, where $\sum_s Z_s = Q = \sum_{\kappa} N^{\kappa} Z^{\kappa} = N_{\mathrm{e}}$.

For the last term in equation (4-80), one combines the reciprocal space portion of E_{II} provided earlier with the interaction energy of the auxiliary charge. First, express the reciprocal space portion of E_{II} as

$$\begin{aligned} &\frac{1}{2}\sum_{s,s'} Z_s Z_{s'} \frac{4\pi}{\Omega_{\mathrm{cell}}} \sum_{\boldsymbol{G}} \frac{1}{|\boldsymbol{G}|^2} e^{-\frac{|\boldsymbol{G}|^2}{4\eta^2}} \cos(\boldsymbol{G}\cdot\boldsymbol{\tau}_{s,s'}) \\ &\quad = \frac{4\pi}{2\Omega_{\mathrm{cell}}} \sum_{\boldsymbol{G}} \frac{1}{|\boldsymbol{G}|^2} \left|\sum_{\kappa} Z^{\kappa} S^{\kappa}(\boldsymbol{G})\right|^2 e^{-\frac{|\boldsymbol{G}|^2}{4\eta^2}}. \end{aligned} \tag{4-88}$$

Now expand $e^{-|\boldsymbol{G}|^2/\left(4\eta^2\right)}$ as a Taylor series around $\boldsymbol{G}=0$ up to the $|\boldsymbol{G}|^2$ term

$$\lim_{|\boldsymbol{G}|\to 0}\frac{4\pi}{2\Omega_{\text{cell}}}\frac{1}{|\boldsymbol{G}|^2}\left|\sum_{\kappa}Z^{\kappa}S^{\kappa}\left(\boldsymbol{G}\right)\right|^2 e^{-\frac{|\boldsymbol{G}|^2}{4\eta^2}}=\frac{4\pi}{2\Omega_{\text{cell}}}\frac{Q^2}{|\boldsymbol{G}|^2}-\frac{\pi Q^2}{2\eta^2\Omega_{\text{cell}}}. \tag{4-89}$$

The Coulomb interaction among the auxiliary charge distribution is expressed in reciprocal space as

$$\frac{1}{2}\iint \mathrm{d}\boldsymbol{r}\mathrm{d}\boldsymbol{r}'\frac{n_{\text{aux}}\left(\boldsymbol{r}\right)n_{\text{aux}}\left(\boldsymbol{r}'\right)}{|\boldsymbol{r}-\boldsymbol{r}'|}=\frac{1}{2}4\pi\,\Omega_{\text{cell}}\sum_{\boldsymbol{G}}\frac{n_{\text{aux}}^2(\boldsymbol{G})}{|\boldsymbol{G}|^2}. \tag{4-90}$$

Utilizing the previously derived Taylor expansion of $n_{\text{aux}}\left(\boldsymbol{G}\right)$ and substituting it into equation (4-90), while neglecting terms of order higher than $|\boldsymbol{G}|^2$, the expression can be reformulated as

$$\lim_{|\boldsymbol{G}|\to 0}\frac{1}{2}4\pi\,\Omega_{\text{cell}}\sum_{\boldsymbol{G}}\frac{n_{\text{aux}}^2(\boldsymbol{G})}{|\boldsymbol{G}|^2}=\frac{4\pi}{2\Omega_{\text{cell}}}\frac{Q^2}{|\boldsymbol{G}|^2}-\frac{\pi Q^2}{2\eta^2\Omega_{\text{cell}}}. \tag{4-91}$$

It is evident that the two terms in equations (4-89) and (4-91) precisely cancel each other. Therefore, it turns out that the divergent terms at $|\boldsymbol{G}|=0$ from the Hartree energy, the energy contribution of the local pseudopotential, and the inter-ionic contribution mutually offset, ensuring the convergence of the total energy.

To sum up, the Ewald summation formula can be obtained as

$$\begin{aligned}\gamma_{\text{Ewald}}&=\frac{1}{2}\sum_{s,s'}Z_sZ_{s'}\sum_{\mathbf{T}}{}'\frac{1}{|\boldsymbol{\tau}_{s,s'}-\mathbf{T}|}\\&=\frac{1}{2}\sum_{s,s'}Z_sZ_{s'}\sum_{\mathbf{T}}{}'\frac{\operatorname{erfc}\left(\eta\,|\boldsymbol{\tau}_{s,s'}-\mathbf{T}|\right)}{|\boldsymbol{\tau}_{s,s'}-\mathbf{T}|}\\&\quad+\frac{1}{2}\sum_{s,s'}Z_sZ_{s'}\frac{4\pi}{\Omega_{\text{cell}}}\sum_{\boldsymbol{G}\neq 0}\frac{1}{|\boldsymbol{G}|^2}e^{-\frac{|\boldsymbol{G}|^2}{4\eta^2}}\cos\left(\boldsymbol{G}\cdot\boldsymbol{\tau}_{s,s'}\right)\\&\quad-\frac{1}{2}\left[\sum_s Z_s^2\right]\frac{2\eta}{\sqrt{\pi}}-\frac{1}{2}\left[\sum_s Z_s\right]^2\frac{\pi}{\eta^2\Omega_{\text{cell}}}.\end{aligned} \tag{4-92}$$

Finally, the total energy of the system is

$$\begin{aligned}E_{\text{total}}&=N_{\sigma}\sum_{\boldsymbol{k},n}f_{n,\boldsymbol{k}}w_{\boldsymbol{k}}\left[\sum_{\boldsymbol{G}}\frac{|\boldsymbol{k}+\boldsymbol{G}|^2}{2}\left|c_{n,\boldsymbol{k}}\left(\boldsymbol{G}\right)\right|^2\right.\\&\quad\left.+\sum_{\boldsymbol{G},\boldsymbol{G}'}c_{n,\boldsymbol{k}}^{*}\left(\boldsymbol{G}\right)V_{\text{NL}}\left(\boldsymbol{G}+\boldsymbol{k},\boldsymbol{G}'+\boldsymbol{k}\right)c_{n,\boldsymbol{k}}\left(\boldsymbol{G}'\right)\right]\\&\quad+\Omega_{\text{cell}}\sum_{\boldsymbol{G}\neq 0,\kappa}S^{\kappa}\left(\boldsymbol{G}\right)V_{\text{local}}^{\kappa}\left(\boldsymbol{G}\right)n\left(\boldsymbol{G}\right)+\Omega_{\text{cell}}\sum_{\boldsymbol{G}\neq 0}\frac{2\pi\left|n\left(\boldsymbol{G}\right)\right|^2}{|\boldsymbol{G}|^2}\\&\quad+\Omega_{\text{cell}}\sum_{\boldsymbol{G}}\epsilon_{\text{XC}}\left(\boldsymbol{G}\right)n\left(\boldsymbol{G}\right)+\gamma_{\text{Ewald}}+\left(\sum_{\kappa}\alpha^{\kappa}N^{\kappa}\right)\frac{N_e}{\Omega_{\text{cell}}}.\end{aligned} \tag{4-93}$$

The current format has all terms represented in the reciprocal space, but it is up to the user/code to determine whether evaluating any term in the reciprocal space or in the real space, according to the relative efficiency.

4.3. Diagonalization of the Hamiltonian

The total energy expression and Hamiltonian form for the plane wave–pseudopotential system in DFT have already been established, providing a clear physical understanding. The subsequent challenge lies in optimizing the computational approach for efficiency. The objective is to enhance computational speed and scalability, enabling the analysis of larger systems without compromising accuracy. Despite significant advancements in modern computing, the feasible number of atoms per unit cell in DFT calculations remains constrained by computational efficiency and memory capacity. Assuming the number of plane waves is N_{PW}, the Hamiltonian matrix size is therefore $N_{\text{PW}}\times N_{\text{PW}}$. While we have assumed $N_{\text{PW}}\sim 10^3$ in small unit cell calculations (cf section 4.2), the number of plane waves grows dramatically when the cell becomes very large, because the magnitudes of reciprocal basis vectors ($\boldsymbol{G}_m$) shrink sharply. To maintain the same G_{cut} setting, a large cell in real space requires much more plane waves in the basis set. For a typical value $N_{\text{PW}}=10^5$, maintaining double-precision floating-point numbers, and considering that the Hamiltonian is complex, it requires approximately 150 GB of data storage. Furthermore, with 10^5 plane waves and ensuring the accuracy of NCPPs under a G_{cut} of 50 Hartree, the lattice constant for a cubic unit cell would be limited to $a=18.1$ Bohr. This significantly restricts the size of the system that can be calculated efficiently. Therefore, it is still necessary to develop algorithms that are more efficient and require less memory, enabling the study of larger systems while maintaining computational feasibility.

The time complexity to complete Hamiltonian diagonalization is $O\left(N_{\text{PW}}^3\right)$. However, in practical scenarios, only the lowest N_{bands} eigenvalues are required, as electronic states are filled from the ground state to the highest energy level. Advanced numerical algorithms, such as the Arnoldi and Lanczos methods [110, 111], have been designed to efficiently compute the lowest N_{bands} eigenvalues. These iterative methods exploit the sparsity and the particular structure of the Hamiltonian matrix, reducing the time complexity to $O\left(N_{\text{bands}}N_{\text{PW}}^2\right)$. Given that $N_{\text{bands}}\ll N_{\text{PW}}$, as is usually the case for small and medium supercells, this results in a significant improvement in computational efficiency. These approaches avoid full diagonalization during computation and do not require the complete storage of the Hamiltonian matrix. Instead, certain vectors like $\widehat{H}|\psi\rangle$ have to be stored. This not only improves efficiency but also saves computer memory, rendering them standard methods widely used in practical codes [112, 113].

To construct $\widehat{H}|\psi\rangle$, the task involves assembling each term of the Hamiltonian as discussed earlier. The process is summarized in figure 14. First of all, the reciprocal space

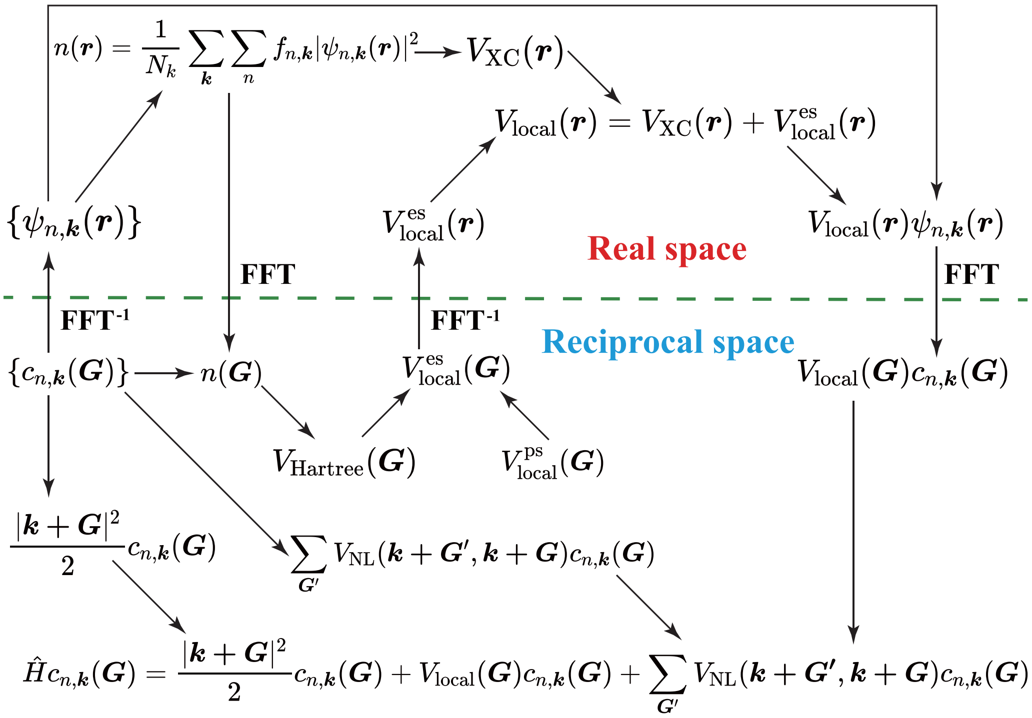

Figure 14. The procedure of constructing $\widehat{H}|\psi\rangle$.

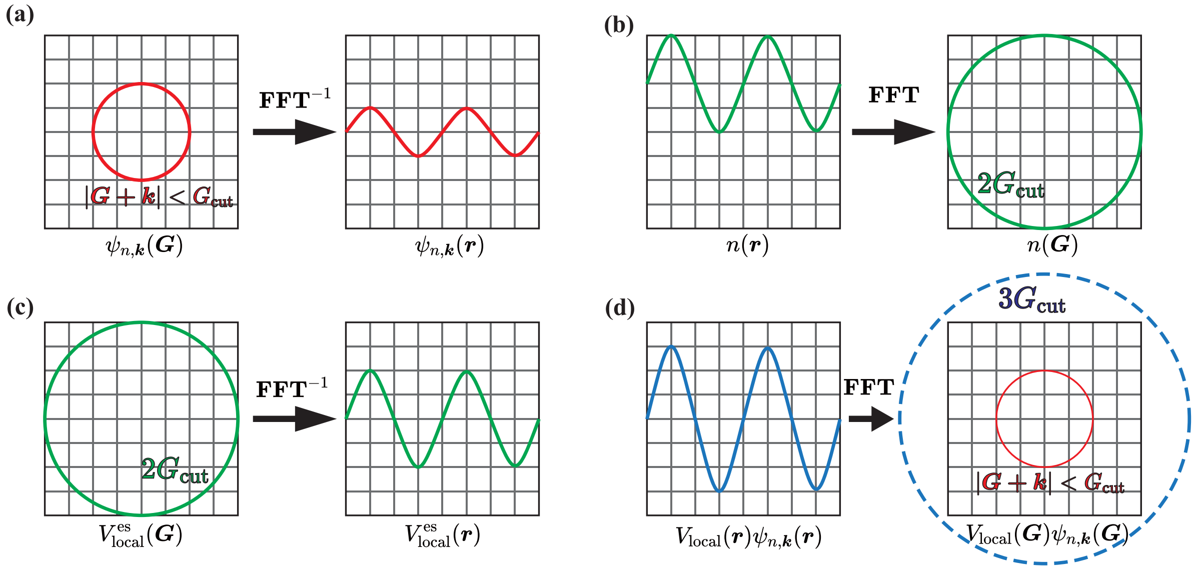

Figure 15. The four FFT/FFT^{-1} processes in constructing $\widehat{H}|\psi\rangle$. (a) The reciprocal space wavefunctions $\psi_{n,\boldsymbol{k}}$ transformed into real space by FFT^{-1}; (b) the electronic density transformed into reciprocal space by FFT for calculating $V_{\mathrm{Hartree}}(\boldsymbol{G})$; (c) $V^{\mathrm{ps}}_{\mathrm{local}}(\boldsymbol{G})$ and $V^{\mathrm{es}}_{\mathrm{local}}(\boldsymbol{G})$ transformed into real space for $V_{\mathrm{local}}(r)\psi_{n,\boldsymbol{k}}(r)$; (d) $V_{\mathrm{local}}(r)\psi_{n,\boldsymbol{k}}(r)$ transformed into reciprocal space, but only the plane waves enclosed by the red circle are used for constructing $\widehat{H}|\psi\rangle$.

wavefunction $\psi_{n,\boldsymbol{k}}$ is transformed into real space using FFT^{-1} for the sake of density $n(\boldsymbol{r})$ calculation. In reciprocal space, the size of the plane-wave basis set is determined by the number of plane waves satisfying $|\boldsymbol{G}+\boldsymbol{k}| \leqslant G_{\mathrm{cut}}$, as represented by the region covered by the red circle in figure 15(a). However, when transformed into real space, the wavefunction spans the entire FFT grid. The density is then transformed into reciprocal space using FFT to compute the Hartree energy E_{Hartree} and the Hartree potential $V_{\mathrm{Hartree}}(\boldsymbol{G})$. As indicated by the green circle in figure 15(b), to avoid the wrap-around error discussed earlier, it is necessary to utilize all plane waves satisfying $|\boldsymbol{G}| \leqslant 2G_{\mathrm{cut}}$. $V_{\mathrm{Hartree}}(\boldsymbol{G})$, combined with the local pseudopotential $V_{\text{local}}^{\text{ps}}(\boldsymbol{G})$ to generate the local electrostatic potential $V_{\text{local}}^{\text{es}}(\boldsymbol{G})$, is then transformed back to real space using inverse FFT as shown in figure 15(c). The exchange-correlation energy E_{XC} and exchange-correlation potential $V_{\text{XC}}(\boldsymbol{r})$ are evaluated directly in real space. Subsequently, the local electrostatic potential $V_{\text{local}}^{\text{es}}(\boldsymbol{r})$ and the exchange-correlation potential $V_{\text{XC}}(\boldsymbol{r})$ are combined in real space, applied to the wavefunction via multiplication, and ultimately transformed into reciprocal space through FFT. For the complete transformation of $V_{\text{local}}^{\text{es}}(\boldsymbol{r})\,\psi_{n,\boldsymbol{k}}(\boldsymbol{r})$, it would theoretically require a plane-wave basis set satisfying $|\boldsymbol{G}+\boldsymbol{k}| \leqslant 3G_{\text{cut}}$, as represented by the dashed blue circle in figure 15(d). However, the final $\widehat{H}c_{n,\boldsymbol{k}}(\boldsymbol{G})$ only requires a plane-wave basis set satisfying $|\boldsymbol{G}+\boldsymbol{k}| \leqslant G_{\text{cut}}$ for diagonalization. Therefore, the last FFT operation needs only the plane-wave bases covered by the red circle. The kinetic energy term and the non-local pseudopotential are computed in reciprocal space. Finally, $\widehat{H}c_{n,\boldsymbol{k}}(\boldsymbol{G})$ is constructed.

With all the required vectors at hand, the problem is ready to be solved. Although there are many available choices for the algorithms, two strategies appear to be very natural.

- Strategy 1: Sequential solution to the eigenvalues. One still works on the $N_{\text{PW}} \times N_{\text{PW}}$ matrix $\boldsymbol{H}_{\text{eff}}$, but no longer diagonalizes it directly to obtain all N_{PW} eigenvalues simultaneously, like in equation (1-16). Rather, the ground state is calculated first through an optimization technique, followed by the higher energy states in a band-by-band manner. Whenever N_{bands} energy eigenvalues are obtained, the calculation finishes. This methodology reduces the amount of energy eigenvalues to be calculated from N_{PW} to N_{bands}. A typical algorithm in this category is the conjugate gradient method.
- Strategy 2: Small matrix diagonalization. Since only N_{bands} eigenvalues are desired, it is in principle possible to transform the $N_{\text{PW}} \times N_{\text{PW}}$ matrix diagonalization problem to an $N_{\text{bands}} \times N_{\text{bands}}$ small matrix diagonalization, finally giving N_{bands} eigenvalues at its diagonal locations. This situation is however overly idealized. In practice, the dimension (row or column) of the matrix to be diagonalized is often several times of N_{bands}, yet still significantly smaller than N_{PW}. The blocked Davidson method, widely employed in modern *ab initio* codes, falls into this category.

4.3.1. The conjugate gradient method. The second property of the Rayleigh quotient, equation (4-15) as introduced in section 4.2, is our starting point. Since the method is iterative, the wavefunction of an electronic state will be denoted as $\psi_{n,\boldsymbol{k},j}$, where the subscripts n, $\boldsymbol{k}$, j represent the band index, the $\boldsymbol{k}$ point and the iteration step index, respectively. For instance, $\langle \psi_{1,\boldsymbol{k},1} | \psi_{1,\boldsymbol{k},1} \rangle = 1$, thus the Rayleigh quotient for $\widehat{H}$ and $\psi_{1,\boldsymbol{k},1}$ is

$$Rq\left(\widehat{H}, \psi_{1,\boldsymbol{k},1}\right) = \langle \psi_{1,\boldsymbol{k},1} | \widehat{H} | \psi_{1,\boldsymbol{k},1} \rangle . \tag{4-94}$$

Finding the minimum of $Rq\left(\widehat{H}, \psi_{1,\boldsymbol{k},1}\right)$ is a quadratic optimization problem, which aligns with the strengths of the conjugate gradient method. The diagonalization process to obtain the lowest eigenvalue can be interpreted as minimizing the Rayleigh quotient. The corresponding gradient is

$$\nabla Rq\left(\widehat{H}, \psi_{1,\boldsymbol{k},1}\right) = 2\left[\widehat{H} - Rq\left(\widehat{H}, \psi_{1,\boldsymbol{k},1}\right)\right] |\psi_{1,\boldsymbol{k},1}\rangle \tag{4-95}$$

but the residual vector is more frequently utilized in practice

$$\boldsymbol{r}_{1,1} = -\left[\widehat{H} - Rq\left(\widehat{H}, \psi_{1,\boldsymbol{k},1}\right)\right] |\psi_{1,\boldsymbol{k},1}\rangle . \tag{4-96}$$

The subscripts in $\boldsymbol{r}_{1,1}$ indicates the first band at the first iteration step.

According to the third property of the Rayleigh quotient, equation (4-19), the wavefunction $\psi_{1,\boldsymbol{k}}$ corresponds to an eigenstate if the condition $\widehat{H}|\psi_{1,\boldsymbol{k}}\rangle = Rq\left(\widehat{H}, \psi_{1,\boldsymbol{k}}\right)|\psi_{1,\boldsymbol{k}}\rangle$ is satisfied. Consequently, the residual vector $\boldsymbol{r}_{1,1}$ provides a direct measure of the numerical error magnitude. This renders the norm of the residual vector a practical criterion for convergence assessment. Notably, $\boldsymbol{r}_{1,i}$ differs from ∇Rq only by a scalar factor, not in direction (since the minimization process adopts the negative gradient as the search direction). The residual vector thus represents the steepest descent direction. In the first iteration step, where no prior constraints exist, the steepest descent direction $\boldsymbol{d}_{1,1}$ is directly employed as the search direction. By minimizing the Rayleigh quotient $Rq\left(\widehat{H}, \psi_{1,\boldsymbol{k},1} + \alpha d_{1,1}\right)$ along this direction, the parameter α is determined. The updated wavefunction $\psi_{1,\boldsymbol{k},1} + \alpha d_{1,1}$ then becomes the input for the next iteration, denoted as $\psi_{1,\boldsymbol{k},2}$. Subsequently, the Rayleigh quotient and the residual vector are re-calculated, yielding the updated steepest descent direction

$$\boldsymbol{r}_{1,2} = -\left[\widehat{H} - Rq\left(\widehat{H}, \psi_{1,\boldsymbol{k},2}\right)\right] |\psi_{1,\boldsymbol{k},2}\rangle . \tag{4-97}$$

However, the residual vector $\boldsymbol{r}_{1,2}$ will not be directly used as the search direction. Instead, the conjugate gradient method imposes foreign orthogonality constraints relative to previous search directions (*e.g.* $\boldsymbol{r}_{1,1}$), a key improvement over the steepest descent method. By enforcing mutual orthogonality between successive search directions, the algorithm achieves accelerated convergence. The iterative process terminates when either the residual norm $\|\boldsymbol{r}_{1,i}\|$ or the difference between two consecutive Rayleigh quotients $\left|Rq\left(\widehat{H}, \psi_{1,\boldsymbol{k},i}\right) - Rq\left(\widehat{H}, \psi_{1,\boldsymbol{k},i-1}\right)\right|$ falls below a pre-defined tolerance threshold. Upon convergence, the ground state energy eigenvalue $\varepsilon_{1,\boldsymbol{k}}$ and its associated eigenvector $\psi_{1,\boldsymbol{k}}$ are formally accepted as numerically exact solutions within the specified tolerance.

Up to now, the algorithm only identifies the lowest-lying energy band. How to compute other energy bands remains a question. Since the conjugate gradient method is an unconstrained optimization technique in its genuine form, the orthogonality of wavefunctions must be incorporated as foreign constraints into the search direction. To preserve orthogonality among the wavefunctions corresponding to different eigenvalues, the search direction for solving the eigenvalue and eigenfunction of the n^{th} band must be orthogonal to the wavefunctions of the $n-1$ lower bands. This can be achieved using Gram-Schmidt orthogonalization to make the search direction orthogonal to the $n-1$ wavefunctions.

$$|\zeta_{n,\boldsymbol{k},i}\rangle = |r_{n,i}\rangle - \sum_{m=1}^{n-1}\langle\psi_{m,\boldsymbol{k}}|r_{n,i}\rangle\,|\psi_{m,\boldsymbol{k}}\rangle. \tag{4-98}$$

Pre-conditioning can perform a similarity transformation on the matrix to make as many eigenvalues as possible degenerate, thereby improving efficiency. Typically, in a plane wave basis set, terms with large $|\boldsymbol{G}|$ are dominated by the kinetic energy term. The pre-conditioning matrix element is given by [9]

$$\boldsymbol{K}_{j,k} = \frac{27+18x+12x^2+8x^3}{27+18x+12x^2+8x^3+16x^4}\delta_{jk} \tag{4-99}$$

where x represents the ratio of the plane wave kinetic energy to the kinetic energy of the wavefunction $\psi_{n,\boldsymbol{k},i}$. The δ_{jk} factor indicates that this is a diagonal matrix.

After multiplied by the search direction vector obtained earlier, the matrix $\boldsymbol{K}$ may disrupt orthogonality, necessitating another round of orthogonalization.

$$|\eta_{n,\boldsymbol{k},i}\rangle = \boldsymbol{K}|\zeta_{n,\boldsymbol{k},i}\rangle \tag{4-100}$$

$$|\eta'_{n,\boldsymbol{k},i}\rangle = |\eta_{n,\boldsymbol{k},i}\rangle - \langle\psi_{n,\boldsymbol{k},i}|\eta_{n,\boldsymbol{k},i}\rangle - \sum_{m=1}^{n-1}\langle\psi_{m,\boldsymbol{k}}|\eta_{n,\boldsymbol{k},i}\rangle\,|\psi_{m,\boldsymbol{k}}\rangle\,. \tag{4-101}$$

Subsequently, following the standard procedure of the conjugate gradient method, the conjugate direction is constructed using $\left|\eta'_{n,\boldsymbol{k},i}\right\rangle$, followed by a 1D search.

The conjugate gradient method is mathematically stable. However, computing the wavefunctions using this method requires a sequential treatment from lower to higher energy levels, processing merely one band at a time. Therefore, Payne *et al* [9] proposed a modified approach that no longer only refers to the $n-1$ lower-energy bands when updating the n^{th} band. Rather, a generalized orthogonality condition involves all wavefunctions except the one from the investigated band itself. This converts equations (4-98) and (4-101) into

$$|\zeta_{n,\boldsymbol{k},i}\rangle = |r_{n,i}\rangle - \sum_{m\neq n}\langle\psi_{m,\boldsymbol{k}}|r_{n,i}\rangle|\psi_{m,\boldsymbol{k}}\rangle \tag{4-102}$$

$$|\eta'_{n,\boldsymbol{k},i}\rangle = |\eta_{n,\boldsymbol{k},i}\rangle - \langle\psi_{n,\boldsymbol{k},i}|\eta_{n,\boldsymbol{k},i}\rangle - \sum_{m\neq n}\langle\psi_{m,\boldsymbol{k}}|\eta_{n,\boldsymbol{k},i}\rangle\,|\psi_{m,\boldsymbol{k}}\rangle\,. \tag{4-103}$$

Such modifications enable the conjugate gradient method to update wavefunctions globally and concurrently, facilitating parallel computing.

4.3.2. The blocked Davidson method. The blocked Davidson method [114, 115] is a subspace iteration approach that is more effective for matrices dominated by diagonal elements, and is closely related to the famous Lanczos method [110]. Modern central processing unit (CPU) cache architectures enable matrix-matrix multiplications to achieve higher computational efficiency, compared to sequential matrix-vector multiplications (*i.e.* splitting matrices into vectors). A Davidson 'block' is a matrix consisting of M state vectors $|\psi_{n,\boldsymbol{k}}\rangle$

$$\boldsymbol{Q}^{[1]} = \left[\begin{array}{cccc}\psi_{1,\boldsymbol{k}} & \psi_{2,\boldsymbol{k}} & \cdots & \psi_{M,\boldsymbol{k}}\end{array}\right].$$

In our case, the dimension of each state vector is $N_{\text{PW}}\times 1$, thus the dimension of $\boldsymbol{Q}^{[1]}$ is $N_{\text{PW}}\times M$, with $N_{\text{PW}}\gg M$. These M state vectors span a subspace $\mathcal{V}=\mathcal{V}^{[1]}$. The functionality of $\boldsymbol{Q}^{[1]}$ is to map the original effective Hamiltonian, an $N_{\text{PW}}\times N_{\text{PW}}$ matrix, into a small matrix $\boldsymbol{H}^{[1]}$

$$\begin{aligned}\boldsymbol{H}^{[1]} &= \left[\boldsymbol{Q}^{[1]}\right]^{\dagger}\boldsymbol{H}\boldsymbol{Q}^{[1]}\\ &= \begin{bmatrix}\left\langle\psi_{1,\boldsymbol{k}}\middle|\widehat{H}\middle|\psi_{1,\boldsymbol{k}}\right\rangle & \left\langle\psi_{1,\boldsymbol{k}}\middle|\widehat{H}\middle|\psi_{2,\boldsymbol{k}}\right\rangle & \cdots & \left\langle\psi_{1,\boldsymbol{k}}\middle|\widehat{H}\middle|\psi_{M,\boldsymbol{k}}\right\rangle\\ \left\langle\psi_{2,\boldsymbol{k}}\middle|\widehat{H}\middle|\psi_{1,\boldsymbol{k}}\right\rangle & \left\langle\psi_{2,\boldsymbol{k}}\middle|\widehat{H}\middle|\psi_{2,\boldsymbol{k}}\right\rangle & \cdots & \left\langle\psi_{2,\boldsymbol{k}}\middle|\widehat{H}\middle|\psi_{M,\boldsymbol{k}}\right\rangle\\ \vdots & \vdots & \ddots & \vdots\\ \left\langle\psi_{M,\boldsymbol{k}}\middle|\widehat{H}\middle|\psi_{1,\boldsymbol{k}}\right\rangle & \left\langle\psi_{M,\boldsymbol{k}}\middle|\widehat{H}\middle|\psi_{2,\boldsymbol{k}}\right\rangle & \cdots & \left\langle\psi_{M,\boldsymbol{k}}\middle|\widehat{H}\middle|\psi_{M,\boldsymbol{k}}\right\rangle\end{bmatrix}\end{aligned} \tag{4-104}$$

whose dimension is merely $M\times M$. Through diagonalizing $\boldsymbol{H}^{[1]}$, one obtains M eigenvectors of $\boldsymbol{H}^{[1]}$, denoted by $\boldsymbol{v}_i^{[1]}$. On the other hand, diagonalizing $\boldsymbol{H}^{[1]}$ also yields its eigenvalues $\lambda_i^{[1]}$, which are the Rayleigh quotients for $\psi_{i,\boldsymbol{k}}^{[1]}=\boldsymbol{Q}^{[1]}\boldsymbol{v}_i^{[1]}$, satisfying

$$\lambda_{\min}(\boldsymbol{H})\leqslant\lambda_{\min}\left(\boldsymbol{H}^{[1]}\right)\leqslant\lambda_{\max}\left(\boldsymbol{H}^{[1]}\right)\leqslant\lambda_{\max}(\boldsymbol{H}) \tag{4-105}$$

because $\mathcal{V}^{[1]}$ is merely a subspace of the entire linear space belonging to $\boldsymbol{H}$. Although the diagonalization of $\boldsymbol{H}^{[1]}$ is mathematically simple because M is small, the problem lies in that the as-derived $\lambda_i^{[1]}$ are in general not the desired lowest few eigenvalues of $\boldsymbol{H}$! The central task of the blocked Davidson method, as well as other similar subspace iteration methods, is to expand and to optimize the subspace $\mathcal{V}$, such that its first M eigenstates correspond to that of $\boldsymbol{H}$ with the lowest energies. In other words, the goal is to ensure that the Rayleigh quotients $Rq\left(\boldsymbol{H}^{[1]},\psi_{i,\boldsymbol{k}}^{[1]}\right)$ closely approximate the lowest few eigenvalues of $\boldsymbol{H}$.

The first challenge, therefore, is constructing an appropriate initial subspace $\mathcal{V}^{[1]}$. For the sake of computational efficiency, one prefers a smaller $\mathcal{V}$ because the subspace diagonalization will be very fast. Yet, a small subspace hardly captures the lowest M eigenstates of $\boldsymbol{H}$, thus the basic strategy is to enlarge $\mathcal{V}^{[1]}$ gradually, until the eigenvalues of $\boldsymbol{H}^{[s]}$ get sufficiently close to the corresponding eigenvalues of $\boldsymbol{H}$, where s is the iteration step index. The methodology of subspace extension lies at the core of such algorithms.

It follows clearly that one cannot work solely within the comfortable small subspace $\mathcal{V}$ to obtain the eigenvalues of $\boldsymbol{H}$. To finally converge to the desired eigenvalues, $\boldsymbol{H}$ itself must participate in the iteration procedure, leading to 'supervised' optimization. This does not imply that the formidable $N_{\mathrm{PW}} \times N_{\mathrm{PW}}$ matrix of $\boldsymbol{H}$ has to be constructed. Rather, the residual vectors can be defined, in the Davidson method, as

$$\boldsymbol{R}_i^{[1]} = \widehat{H}\left|\psi_{i,\boldsymbol{k}}^{[1]}\right\rangle - \lambda^{[1]}\left|\psi_{i,\boldsymbol{k}}^{[1]}\right\rangle \tag{4-106}$$

and the norm $\left\|\boldsymbol{R}_i^{[1]}\right\|$ is used as a criterion for convergence. Note that in this expression, $\widehat{H}$ only appears in the form of $\widehat{H}\left|\psi_{i,\boldsymbol{k}}^{[1]}\right\rangle$, which is an $N_{\mathrm{PW}} \times 1$ vector. Hence, in the same manner as documented in section 4.2, $\widehat{H}\left|\psi_{i,\boldsymbol{k}}^{[1]}\right\rangle$ may be constructed with all contributions to $\widehat{H}$ separated. Yet, the blocked Davidson method derives many $\widehat{H}\left|\psi_{i,\boldsymbol{k}}^{[1]}\right\rangle$ vectors in the same time, through assembling $\left|\psi_{i,\boldsymbol{k}}^{[1]}\right\rangle$ into a matrix block, which greatly improves the efficiency.

At the sth iteration step, given that all $\left\|\boldsymbol{R}_i^{[s]}\right\|$ are below an error threshold σ, the current Rayleigh quotients and state vectors are regarded as reasonable approximations to the energy eigenvalues and eigenvectors for $\boldsymbol{H}$. Otherwise, the subspace must be expanded to include more basis vectors. $\boldsymbol{R}_i^{[1]}$ should indicate new searching directions. Conventionally, they may be orthonormalized with respect to the existing vectors, and included in $\boldsymbol{Q}^{[1]}$ to expand the subspace. However, pre-conditioning of $\boldsymbol{R}_i^{[1]}$ is a key step in the Davidson method, which renders great acceleration in convergence. First of all, the residual vectors are transformed to yield

$$\boldsymbol{t}_i^{[1]} = \left(\boldsymbol{D} - \lambda_i^{[1]}\boldsymbol{I}\right)^{-1}\boldsymbol{R}_i^{[1]} \tag{4-107}$$

where matrix $\boldsymbol{D}$ represents the diagonal matrix of $\boldsymbol{H}$ with all off-diagonal elements set to zero

$$\boldsymbol{D}_{ij} = \begin{cases} \boldsymbol{H}_{ii}, & i = j \\ 0 & i \neq j \end{cases} \tag{4-108}$$

The acceleration due to such pre-conditioning relies on the diagonal dominance of the matrix (as exemplified by the Hamiltonian matrix in reciprocal space), which implies that the eigenvalues typically remain close to its diagonal elements. Hence, off-diagonal terms may be regarded as minor perturbations. Consequently, an input as $\left(\boldsymbol{D} - \lambda_i^{[1]}\boldsymbol{I}\right)^{-1}\boldsymbol{R}_i^{[1]}$ could effectively converge to $\left(\boldsymbol{H} - \lambda_i^{[1]}\boldsymbol{I}\right)^{-1}\boldsymbol{R}_i^{[1]}$ during the entire iterative computation process. Furthermore, the inversion operation $\left(\boldsymbol{D} - \lambda_i^{[1]}\boldsymbol{I}\right)^{-1}$ is computationally straightforward because $\boldsymbol{D} - \lambda_i^{[1]}\boldsymbol{I}$ is merely a diagonal matrix. The existence of such pre-conditioning step renders the subspace $\mathcal{V}^{[s]}$ no longer a Krylov subspace [116] as in the Lanczos method case.

Upon obtaining $\boldsymbol{t}_i^{[1]}$, it should be made orthonormal with respect to all the existing basis vectors in $\boldsymbol{Q}^{[1]}$. This yields the orthonormal version $\bar{\boldsymbol{t}}_i^{[1]}$, which are added to the subspace as new basis vectors. Hence,

$$\boldsymbol{Q}^{[2]} = \begin{bmatrix} \psi_{1,\boldsymbol{k}} & \cdots & \psi_{M,\boldsymbol{k}} & \bar{\boldsymbol{t}}_1^{[1]} & \cdots & \bar{\boldsymbol{t}}_M^{[1]} \end{bmatrix} \tag{4-109}$$

which owns a dimension of $N_{\mathrm{PW}} \times 2M$. Subsequently, the $2M \times 2M$ matrix $\boldsymbol{H}^{[2]} = \left[\boldsymbol{Q}^{[2]}\right]^{\dagger}\boldsymbol{H}\boldsymbol{Q}^{[2]}$ is constructed and diagonalized, leading to $\lambda_j^{[2]}$ and $\boldsymbol{v}_j^{[2]}$, but the range of j is $[1, 2M]$. While $2M$ eigenvalues are obtained, one should select the lowest M eigenvalues $\lambda_i^{[2]}$ and the corresponding eigenstates $\psi_{i,\boldsymbol{k}}^{[2]} = \boldsymbol{Q}^{[2]}\boldsymbol{v}_i^{[2]}$ for convergence evaluation. The residual vector is re-calculated as $\boldsymbol{R}_i^{[2]} = \widehat{H}\left|\psi_{i,\boldsymbol{k}}^{[2]}\right\rangle - \lambda^{[2]}\left|\psi_{i,\boldsymbol{k}}^{[2]}\right\rangle$. Provided that $\left\|\boldsymbol{R}_i^{[2]}\right\| < \sigma$ are fulfilled for $i \in [1, M]$, convergence is reached. Otherwise, the same pre-conditioning procedure is carried out, and the orthonormalized vectors $\bar{\boldsymbol{t}}_i^{[2]}$ are added to the subspace, yielding

$$\boldsymbol{Q}^{[3]} = \begin{bmatrix} \psi_{1,\boldsymbol{k}} & \cdots & \psi_{M,\boldsymbol{k}} & \bar{\boldsymbol{t}}_1^{[1]} & \cdots & \bar{\boldsymbol{t}}_M^{[1]} & \bar{\boldsymbol{t}}_1^{[2]} & \cdots & \bar{\boldsymbol{t}}_M^{[2]} \end{bmatrix}. \tag{4-110}$$

A new round of iteration then starts. Since in each round of iteration, only M new vectors are added, the column size expansion of $\boldsymbol{Q}$ is linear, rather than geometric. This is more efficient than doubling the column size of $\boldsymbol{Q}$ each time.

There are several notes regarding the blocked Davidson method.

(i) Although by default M vectors are added into $\boldsymbol{Q}^{[s]}$, this is not mandatory and one may supplement less or more vectors upon special needs. Yet, the number of newly added vectors in each round cannot exceed the number of existing vectors in $\boldsymbol{Q}^{[s]}$ due to the evaluation of $\boldsymbol{t}_i^{[s]}$ as in equation (4-107). For instance, after the first round of iteration, one cannot supplement more than M vectors in the subspace, since the original $\boldsymbol{Q}^{[1]}$ merely consists of M vectors.

(ii) The ultimate goal is to find out the lowest few energy eigenvalues for $\boldsymbol{H}$. After each round of iteration, only the M lowest eigenvalues of $\boldsymbol{H}^{[s]}$ and the corresponding eigenvectors are considered for convergence inspection, as well as to construct the new vectors.

(iii) In case convergence has not been reached after many rounds of iterations, the subspace is supposed to become too large to be diagonalized directly. This requires a restart of the procedure, but not starting from scratch, because the M lowest energy eigenvalues and the corresponding eigenvectors may be utilized to construct the new initial subspace.

In practical implementation, it is natural to fix $M = N_{\text{bands}}$ whenever the unit cell is very small. Nevertheless, if N_{bands} is also a big number, direct diagonalization of $\boldsymbol{H}^{[s]}$ can be impractical. In that case, multiple subspaces have to be introduced by grouping the N_{bands} eigenvectors into

$$\left[\underbrace{\psi_{1,\boldsymbol{k}} \quad \cdots \quad \psi_{N_1,\boldsymbol{k}}}_{N_1} \quad \Big| \quad \underbrace{\psi_{N_1+1,\boldsymbol{k}} \quad \cdots \quad \psi_{N_2,\boldsymbol{k}}}_{N_2-N_1} \quad \Big| \quad \underbrace{\psi_{N_2+1,\boldsymbol{k}} \quad \cdots \quad \psi_{N_3,\boldsymbol{k}}}_{N_3-N_2} \quad \Big| \quad \cdots \right]. \qquad (4\text{-}111)$$

The blocked Davidson method is applied to each group independently. Eventually, each group only donates a fixed amount of eigenvectors ($[N_1 \mid N_2 - N_1 \mid N_3 - N_2 | \cdots]$) belonging to the lowest few energy eigenvalues in that subspace. And the collection of all these N_{bands} eigenvectors span a final subspace. Carrying out the Rayleigh-Ritz variational calculation within this N_{bands}–dimensional subspace yields the final energy eigenvalues as well as eigenvectors.

4.4. Charge mixing

After diagonalizing the Hamiltonian, the eigenvalues and eigenfunctions are obtained, enabling the calculation of the electronic charge density, which equals the electron density under atomic units. The criterion for self-consistent convergence is that the absolute difference between the input charge density ρ_i^{in} and the output charge density ρ_i^{out} at the ith step, $\rho_i^{\text{out}} - \rho_i^{\text{in}}$, is less than the specified error threshold. However, for random initialization, or using the overlap of atomic valence charge densities for initialization, the initial charge density may differ significantly from the ground-state charge density. In such cases, directly using the output charge density as the input for the next step, $\rho_i^{\text{out}} \Rightarrow \rho_{i+1}^{\text{in}}$, might lead to oscillations and non-convergence. Therefore, the simplest approach is to perform a linear mixing by taking a portion of the input charge density, such as

$$\rho_{i+1}^{\text{in}} = \rho_i^{\text{in}} + \beta\left(\rho_i^{\text{out}} - \rho_i^{\text{in}}\right), \ 0 < \beta \leqslant 1. \qquad (4\text{-}112)$$

For non-spin-polarized systems, the mixing parameter is typically $\beta = 0.3$. For large metallic supercells, however, the charge sloshing failure is frequently encountered. The problem lies in that the free electrons in a metal are quite sensitive to the change of the potential. Indeed, the Coulomb interaction is long-range in nature [117], thus the impact of electron density variation propagates in the entire solid, possibly causing an over-large update in the new version of electron density. The electrostatic potential tends to recover charge equilibrium, but the extent of such recovery may exceed the normal scope. The consequence of such over-correction is that the charges oscillate between distinct regions of the real space, leading to non-convergence of the self-consistent cycle. The ordinary linear mixing scheme uses the same mixing coefficient β for all momentum components, which could fail to inhibit the instability originating from the long wavelength (low frequency) components. To resolve this problem, Kerker proposed a pre-conditioning method [118], which writes the new charge density as

$$\rho_{i+1}^{\text{in}} = \rho_i^{\text{in}} + \beta\frac{G^2}{G^2 + q_0^2}\left(\rho_i^{\text{out}} - \rho_i^{\text{in}}\right) \qquad (4\text{-}113)$$

where $G = |\boldsymbol{G}_m|$ and a constant wavevector q_0 has to be selected. The effect of q_0 is straightforward as follows. For low-frequency components,

$$\frac{G^2}{G^2 + q_0^2} \to \frac{G^2}{q_0^2} \qquad (4\text{-}114)$$

which get suppressed as long as q_0 is large. For high-frequency components, on the other hand,

$$\frac{G^2}{G^2 + q_0^2} \to 1 \qquad (4\text{-}115)$$

where linear mixing is almost recovered. The value of q_0^2 may be optimized based on the specific system under investigation. In practice, a lower-limit ($\beta_{\min}$) may be set for the mixing parameter, to preserve the contributions from low-frequency components

$$\rho_{i+1}^{\text{in}} = \rho_i^{\text{in}} + \max\left(\frac{\beta G^2}{G^2 + q_0^2}, \ \beta_{\min}\right)\left(\rho_i^{\text{out}} - \rho_i^{\text{in}}\right). \qquad (4\text{-}116)$$

And β is typically set to 0.8 in this case [113]. The pre-conditioning method from Kerker may be used in Pulay mixing and Broyden mixing as well (see below), where a pre-conditioning matrix could be defined as

$$\boldsymbol{K} = \begin{bmatrix} \max\left(\frac{\beta G_1^2}{G_1^2+q_0^2},\, \beta_{\min}\right) & 0 & \cdots & 0 \\ 0 & \max\left(\frac{\beta G_2^2}{G_2^2+q_0^2},\, \beta_{\min}\right) & \cdots & 0 \\ \vdots & \vdots & \ddots & \vdots \\ 0 & 0 & \cdots & \max\left(\frac{\beta G_{N_{\mathrm{pw}}}^2}{G_{N_{\mathrm{pw}}}^2+q_0^2},\, \beta_{\min}\right) \end{bmatrix}. \tag{4-117}$$

4.4.1. Pulay mixing. Pulay mixing [119] is sometimes called direct inversion in the iterative subspace (DIIS), whose core concept lies in using the residual errors from the last few mixing steps. The least square method is used for extrapolation, predicting the direction of the new electron density distribution. The next-step electron density is written as a linear combination of the previous few steps. Provided that the residual vector during iteration is subject to a linear variation approximately, the new residual vector could be expressed as a linear combination of the past residual vectors

$$\begin{aligned} \boldsymbol{R}\left[\rho_{N+1}^{\mathrm{in}}\right] &= \boldsymbol{R}\left[\sum_{i=N-M+1}^{N} \alpha_i \rho_i^{\mathrm{in}}\right] \\ &= \sum_{i=N-M+1}^{N} \alpha_i \boldsymbol{R}\left[\rho_i^{\mathrm{in}}\right], \quad \sum_{i=N-M+1}^{N} \alpha_i = 1. \end{aligned} \tag{4-118}$$

Here N is the current step index, and only the last M steps (including the N^{th} step) are utilized to determine the residual vector $\boldsymbol{R}$. Based upon equation (4-118), one strives to minimize the norm of the residual vector to obtain the coefficients, according to $\min\left\{\left\|\boldsymbol{R}\left[\rho_{N+1}^{\mathrm{in}}\right]\right\|\right\} = \min\left\{\left\|\sum_i \alpha_i \boldsymbol{R}\left[\rho_i^{\mathrm{in}}\right]\right\|\right\}$ under the constraint of $\sum_i \alpha_i = 1$. This problem is readily solvable in terms of the Lagrange multiplier method. The Lagrangian function is constructed as

$$L = \boldsymbol{\alpha}^{\mathrm{T}} \boldsymbol{A} \boldsymbol{\alpha} - \lambda \left(\sum_i \alpha_i - 1\right) \tag{4-119}$$

where λ is the Lagrange multiplier and the matrix $\boldsymbol{A}$ is defined through its matrix elements

$$\boldsymbol{A}_{ij} = \left\langle R\left[\rho_i^{\mathrm{in}}\right] \middle| R\left[\rho_j^{\mathrm{in}}\right]\right\rangle. \tag{4-120}$$

And $\boldsymbol{\alpha}$ is an M-dimensional vector assembled through

$$\boldsymbol{\alpha} = \begin{bmatrix} \alpha_{N-M+1} \\ \alpha_{N-M+2} \\ \vdots \\ \alpha_N \end{bmatrix}. \tag{4-121}$$

Differentiating L with respect to λ yields the ordinary normalization constraint for α_i

$$\sum_{i=N-M+1}^{N} \alpha_i = 1 \tag{4-122}$$

which is re-written in matrix form as

$$\mathbf{1}^{\mathrm{T}} \boldsymbol{\alpha} = 1 \tag{4-123}$$

where $\mathbf{1}$ stands for a constant M-dimensional all-ones vector $\begin{bmatrix} 1 & 1 & \cdots & 1 \end{bmatrix}^{\mathrm{T}}$. On the other hand, differentiating L with respect to $\boldsymbol{\alpha}$ yields

$$2\boldsymbol{A}\boldsymbol{\alpha} = \lambda \mathbf{1}. \tag{4-124}$$

The vector $\boldsymbol{\alpha}$ is then readily obtained through matrix inversion

$$\boldsymbol{\alpha} = \frac{\lambda}{2} \boldsymbol{A}^{-1} \mathbf{1} \tag{4-125}$$

which can be combined with the constraint equation (4-123) to yield

$$\mathbf{1}^{\mathrm{T}} \frac{\lambda}{2} \boldsymbol{A}^{-1} \mathbf{1} = \frac{\lambda}{2} \mathbf{1}^{\mathrm{T}} \boldsymbol{A}^{-1} \mathbf{1} = 1. \tag{4-126}$$

The desired Lagrange multiplier follows simply

$$\lambda = \frac{2}{\mathbf{1}^{\mathrm{T}} \boldsymbol{A}^{-1} \mathbf{1}}. \tag{4-127}$$

Bring the λ value back to equation (4-125), and the coefficient vector $\boldsymbol{\alpha}$ is obtained as

$$\boldsymbol{\alpha} = \frac{\boldsymbol{A}^{-1} \mathbf{1}}{\mathbf{1}^{\mathrm{T}} \boldsymbol{A}^{-1} \mathbf{1}}. \tag{4-128}$$

The individual coefficients are

$$\alpha_i = \frac{\sum_j \boldsymbol{A}_{ij}^{-1}}{\sum_k \sum_j \boldsymbol{A}_{kj}^{-1}}. \tag{4-129}$$

The denominator is the sum of all elements in $\boldsymbol{A}^{-1}$, while the numerator sums only the i^{th} row elements of $\boldsymbol{A}^{-1}$.

Usually, only the residual vectors in the past few steps are of significance, thus a direct matrix inversion method is applicable in obtaining the coefficients α_i. Kresse and Furthmüller [113] further took into account the variations in charge density and the residual vector, *i.e.* $\Delta\boldsymbol{\rho}_i = \boldsymbol{\rho}_{i+1}^{\mathrm{in}} - \boldsymbol{\rho}_i^{\mathrm{in}}$ and $\Delta\boldsymbol{R}_i = \boldsymbol{R}\left[\boldsymbol{\rho}_{i+1}^{\mathrm{in}}\right] - \boldsymbol{R}\left[\boldsymbol{\rho}_i^{\mathrm{in}}\right]$, to improve the numerical stability and convergence speed. Specifically, the predicted charge density becomes

$$\boldsymbol{\rho}_{N+1}^{\text{in}} = \boldsymbol{\rho}_{N}^{\text{in}} + \boldsymbol{K}\boldsymbol{R}\left[\boldsymbol{\rho}_{N}^{\text{in}}\right] + \sum_{i=N-M+1}^{N-1} \bar{\alpha}_i \left[\Delta\boldsymbol{\rho}_i + \boldsymbol{K}\Delta\boldsymbol{R}_i\right] \tag{4-130}$$

where the bar on top of α_i emphasizes that this coefficient is within the Kresse–Furthmüller revised formulation. To obtain the new $\bar{\alpha}_i$ values, one may define

$$L = \left\langle \boldsymbol{R}_N + \sum_{i=N-M+1}^{N-1} \bar{\alpha}_i \Delta\boldsymbol{R}_i \middle| \boldsymbol{R}_N + \sum_{j=N-M+1}^{N-1} \bar{\alpha}_j \Delta\boldsymbol{R}_j \right\rangle. \tag{4-131}$$

Differentiate L with respect to $\bar{\alpha}_i$, and one obtains

$$2\left\langle \Delta\boldsymbol{R}_i \middle| \boldsymbol{R}_N + \sum_{j=N-M+1}^{N-1} \bar{\alpha}_j \Delta\boldsymbol{R}_j = 0 \right\rangle. \tag{4-132}$$

Some simple algebra yields the following relation

$$\sum_{j=N-M+1}^{N-1} \left\langle \Delta\boldsymbol{R}_i \middle| \Delta\boldsymbol{R}_j \right\rangle \bar{\alpha}_j = -\left\langle \Delta\boldsymbol{R}_i \middle| \boldsymbol{R}_N \right\rangle. \tag{4-133}$$

One may further introduce

$$\bar{\boldsymbol{A}}_{ij} = \left\langle \Delta\boldsymbol{R}_i \middle| \Delta\boldsymbol{R}_j \right\rangle \tag{4-134}$$

and

$$\boldsymbol{b}_i = -\left\langle \Delta\boldsymbol{R}_i \middle| \boldsymbol{R}_N \right\rangle \tag{4-135}$$

then an expression for $\bar{\alpha}_i$ follows

$$\bar{\alpha}_i = -\sum_{j=N-M+1}^{N-1} \left(\bar{\boldsymbol{A}}^{-1}\right)_{ji} \left\langle \Delta\boldsymbol{R}_j \middle| \boldsymbol{R}_N \right\rangle. \tag{4-136}$$

Similar to Pulay mixing, Anderson mixing [120] is another method that also makes use of historical density profiles and residues. Their difference lies in that, Pulay mixing directly minimizes the norm of the residual vector, but in the scheme of Anderson mixing, an explicit linear combination formula is prescribed to constitute the new density.

4.4.2. Broyden mixing. The charge mixing task is intrinsically equivalent to the $F(\boldsymbol{x}) = \boldsymbol{x}$ problem mathematically, to which the Newton method and quasi-Newton method could apply. Instead of calculating the inverse of the second derivative matrix (Hessian matrix), the quasi-Newton method updates the Jacobian matrix ($\boldsymbol{J}$) for a solution. Broyden proposed to tackle the charge mixing problem using the quasi-Newton method [121]. The predicted charge density is written as

$$\boldsymbol{\rho}_{N+1}^{\text{in}} = \boldsymbol{\rho}_{N}^{\text{in}} + \boldsymbol{J}_N^{-1}\boldsymbol{R}\left[\boldsymbol{\rho}_{N}^{in}\right] \tag{4-137}$$

where $\boldsymbol{J}^{-1}$ lies at the heart of the algorithm. Various Broyden methods and their improved versions differ in the way how $\boldsymbol{J}$ or $\boldsymbol{J}^{-1}$ is updated. For example, the two methods proposed by Broyden only record the density profile and residue information at the current step. Vanderbilt and Louie [122] suggested using all the iterative history, but it will render a very big Jacobian matrix. On the other hand, Johnson [123] proposed a modified Broyden mixing method that has been widely used till now. Like the Pulay method, it only refers to the last few iterative steps. An error function is introduced as

$$E = w_0^2 \left\|\boldsymbol{G}_{N+1} - \boldsymbol{G}_N\right\| + \sum_{i=1}^{N} w_i^2 \left\| \left|\Delta\rho_i\right\rangle + \boldsymbol{G}_{N+1}\Delta\boldsymbol{R}_i \right\| \tag{4-138}$$

where $\boldsymbol{G}_N = \boldsymbol{J}_N^{-1}$ and w_i are weight parameters that are employed to adjust the relative weight from each previous step. In equation (4-138), the first term constrains the variation of $\boldsymbol{G}_N$ in each step. The second term is the quasi-Newton condition, which assumes that the residual vector $\boldsymbol{R}[\rho]$ varies linearly near the minimum. This is formalized as

$$\boldsymbol{R}\left[\rho_{N+1}\right] = \boldsymbol{R}\left[\rho_N\right] - \boldsymbol{J}_N\left(\left|\rho_{N+1}^{\text{in}}\right\rangle - \left|\rho_N^{\text{in}}\right\rangle\right) \Rightarrow \Delta\boldsymbol{\rho}_i = -\boldsymbol{G}_{N+1}\Delta\boldsymbol{R}_i. \tag{4-139}$$

If this equality holds, $\boldsymbol{G}_{N+1}$ coincides with the exact inverse of the Jacobian matrix. Therefore, the second term quantifies the discrepancy between the approximate $\boldsymbol{G}_{N+1}$ and the true $\boldsymbol{J}^{-1}$. Subsequently, one may obtain $\boldsymbol{G}_{N+1}$ according to $\partial E/\partial \boldsymbol{G}_{N+1,ij} = 0$.

$$w_0^2\left(\boldsymbol{G}_{N+1} - \boldsymbol{G}_N\right) + \sum_{i=1}^{N} w_i^2 \left(\left|\Delta\rho_i\right\rangle + \boldsymbol{G}_{N+1}\left|\Delta\boldsymbol{R}_i\right\rangle\right)\left\langle\Delta\boldsymbol{R}_i\right| = 0. \tag{4-140}$$

A simple algebraic rearrangement yields

$$\boldsymbol{G}_{N+1}\left(w_0^2\boldsymbol{I} + \sum_{i=1}^{N} w_i^2 \left|\Delta\boldsymbol{R}_i\right\rangle\left\langle\Delta\boldsymbol{R}_i\right|\right) = w_0^2\boldsymbol{G}_N - \sum_{i=1}^{N} w_i^2 \left|\Delta\rho_i\right\rangle\left\langle\Delta\boldsymbol{R}_i\right| \tag{4-141}$$

thus

$$\boldsymbol{A}_{N+1} = w_0^2\boldsymbol{G}_N - \sum_{i=1}^{N} w_i^2 \left|\Delta\rho_i\right\rangle\left\langle\Delta\boldsymbol{R}_i\right| \tag{4-142}$$

and

$$\boldsymbol{B}_{N+1} = w_0^2\boldsymbol{I} + \sum_{i=1}^{N} w_i^2 \left|\Delta\boldsymbol{R}_i\right\rangle\left\langle\Delta\boldsymbol{R}_i\right|. \tag{4-143}$$

It follows that

$$\boldsymbol{G}_{N+1} = \boldsymbol{A}_{N+1}\left(\boldsymbol{B}_{N+1}\right)^{-1}. \tag{4-144}$$

To proceed, one needs the inverse matrix of $\boldsymbol{B}_{N+1}$, which is expressed as

$$\begin{aligned}\boldsymbol{B}_{N+1} &= w_0^2\left[\boldsymbol{I}+\sum_{i=1}^{N}\left(\frac{w_i}{w_0}\left|\Delta\boldsymbol{R}_i\right\rangle\right)\left(\frac{w_i}{w_0}\left\langle\Delta\boldsymbol{R}_i\right|\right)^{\dagger}\right]\\ &= w_0^2\left(\boldsymbol{D}+\boldsymbol{U}\boldsymbol{U}^{\dagger}\right)\end{aligned} \tag{4-145}$$

where $\boldsymbol{D}=\boldsymbol{I}$ and $\boldsymbol{U}=\left[\begin{array}{ccc}\frac{w_1}{w_0}\left|\Delta\boldsymbol{R}_1\right\rangle & \cdots & \frac{w_N}{w_0}\left|\Delta\boldsymbol{R}_N\right\rangle\end{array}\right]$. The Sherman–Morrison–Woodbury identity [124] states that

$$\left(\boldsymbol{D}+\boldsymbol{U}\boldsymbol{U}^{\dagger}\right)^{-1}=\boldsymbol{D}^{-1}-\boldsymbol{D}^{-1}\boldsymbol{U}\left(\boldsymbol{I}+\boldsymbol{U}^{\dagger}\boldsymbol{D}^{-1}\boldsymbol{U}\right)^{-1}\boldsymbol{U}^{\dagger}\boldsymbol{D}^{-1} \tag{4-146}$$

where

$$\boldsymbol{U}^{\dagger}\boldsymbol{U}=\left[\begin{array}{ccc}\frac{w_1w_1}{w_0^2}\left\langle\Delta\boldsymbol{R}_1\middle|\Delta\boldsymbol{R}_1\right\rangle & \cdots & \frac{w_1w_N}{w_0^2}\left\langle\Delta\boldsymbol{R}_1\middle|\Delta\boldsymbol{R}_N\right\rangle\\ \vdots & \ddots & \vdots\\ \frac{w_Nw_1}{w_0^2}\left\langle\Delta\boldsymbol{R}_N\middle|\Delta\boldsymbol{R}_1\right\rangle & \cdots & \frac{w_Nw_N}{w_0^2}\left\langle\Delta\boldsymbol{R}_N\middle|\Delta\boldsymbol{R}_N\right\rangle\end{array}\right]. \tag{4-147}$$

Consequently, the matrix $\boldsymbol{\beta}$ is defined as

$$\boldsymbol{\beta}=\left[w_0^2\left(\boldsymbol{I}+\boldsymbol{U}^{\dagger}\boldsymbol{U}\right)\right]^{-1} \tag{4-148}$$

and thus

$$\left(\boldsymbol{B}_{N+1}\right)^{-1}=w_0^{-2}\left[\boldsymbol{I}-\sum_{j,k=1}^{N}w_jw_k\boldsymbol{\beta}_{kj}\left|\Delta\boldsymbol{R}_j\right\rangle\left\langle\Delta\boldsymbol{R}_k\right|\right]. \tag{4-149}$$

Here, the complex summation $\sum_{j,k=1}^{N}w_jw_k\boldsymbol{\beta}_{kj}\left|\Delta\boldsymbol{R}_j\right\rangle\left\langle\Delta\boldsymbol{R}_k\right|$ is equivalent to the expanded form of $\boldsymbol{U}\boldsymbol{\beta}\boldsymbol{U}^{\dagger}$. Substituting this back into $\boldsymbol{G}_{N+1}=\boldsymbol{A}_{N+1}\left(\boldsymbol{B}_{N+1}\right)^{-1}$ and neglecting higher-order terms arising from the product of $\left(\boldsymbol{B}_{N+1}\right)^{-1}$ and the second terms in $\boldsymbol{A}_{N+1}$, one obtains

$$\begin{aligned}\boldsymbol{G}_{N+1}\approx\boldsymbol{G}_N&-\sum_{j,k=1}^{N}\left(w_jw_k\boldsymbol{\beta}_{kj}\boldsymbol{G}_N\left|\Delta\boldsymbol{R}_j\right\rangle\right)\left\langle\Delta\boldsymbol{R}_k\right|\\ &-\sum_{j=1}^{N}\frac{w_k^2}{w_0^2}\left|\Delta\rho_j\right\rangle\left\langle\Delta\boldsymbol{R}_k\right|.\end{aligned} \tag{4-150}$$

Kresse and Furthmüller [113] used a simplified relation

$$\boldsymbol{G}_{N+1}=\boldsymbol{G}_N-\sum_{j,k=1}^{N}w_jw_k\boldsymbol{\beta}_{kj}\left(\boldsymbol{G}_N\left|\Delta\boldsymbol{R}_j\right\rangle+\left|\Delta\rho_j\right\rangle\right)\left\langle\Delta\boldsymbol{R}_k\right|, \tag{4-151}$$

assuming $\boldsymbol{G}_N$ takes the following form

$$\boldsymbol{G}_N=\boldsymbol{K}-\sum_{k=1}^{N-1}\left|z_{N-1,k}\right\rangle\left\langle\Delta\boldsymbol{R}_k\right|. \tag{4-152}$$

Substituting this into equation (4-150) via mathematical induction yields the recursive relation for the vectors

$$\left|z_{N,k}\right\rangle=\sum_{i=1}^{N}w_kw_i\boldsymbol{\beta}_{ki}\left|u_i\right\rangle+\sum_{i=1}^{N-1}\overline{\boldsymbol{\beta}}_{ki}\left|z_{N-1,i}\right\rangle \tag{4-153}$$

where

$$\left|u_i\right\rangle=\boldsymbol{K}\left|\Delta\boldsymbol{R}_i\right\rangle+\left|\Delta\rho_i\right\rangle \tag{4-154}$$

and

$$\bar{\beta}_{ki}=\delta_{ki}-\sum_{j=1}^{N}w_kw_j\beta_{kj}\left\langle\Delta\boldsymbol{R}_i\middle|\Delta\boldsymbol{R}_j\right\rangle. \tag{4-155}$$

In practice, one may take a further simplification as to set $w_0=0$, while other w_i values are equal, typically set to 1.

4.5. Strategies in parallel computing

For the sake of efficiency, the design of parallel computing in plane wave–pseudopotential DFT calculations has to consider the characteristic of the plane wave basis as well as the feasibility in task decomposition. From the perspective of data storage, the wavefunction depends on three major quantities in reciprocal space, including the $\boldsymbol{k}$ points, energy band data and the plane-wave bases; in real space it is electron density and local potentials that are stored, which only rely on the variable $\boldsymbol{r}$. There are three levels at which parallelization may be carried out, *i.e.* real space grid and reciprocal space plane-wave basis parallelization, parallelizing in energy bands, as well as parallelizing in $\boldsymbol{k}$ points. Here, we denote the real space as R-space and the reciprocal space as G-space. Consequently, the real space grid–reciprocal space plane waves parallelization can be referred to as R/G parallelization for short. The parallel computing environment is anchored in a multi-core server configuration, and a process (usually carried out on one core) is the basic computing unit.

4.5.1. R/G parallelization. Both R-space and G-space are required in carrying out an electronic structure calculation. The electronic wavefunction in G-space has to be transformed into R-space, through FFT^{-1}, for electron density calculation. Nevertheless, after multiplied by the local effective potential, it has to be transformed back to G-space through FFT. And the Hartree potential is also evaluated in the G-space through an FFT of the real space electron density. There is a strong connection between R-space grid and G-space plane-wave basis, thus a great amount of data are retrieved during the FFT process. However, 3D FFT may be divided into 1D FFTs, which, besides enabling parallel computing, could greatly reduce the amount of data to be processed.

A typical parallelization scheme is illustrated in figure 16. (i) Divide R-space grid into multiple groups of x–y planes, and each group of planes is assigned a process; (ii) in the grid of G-space, separate out several segments along the z-axis, and each segment is assigned a process. The FFT is first carried

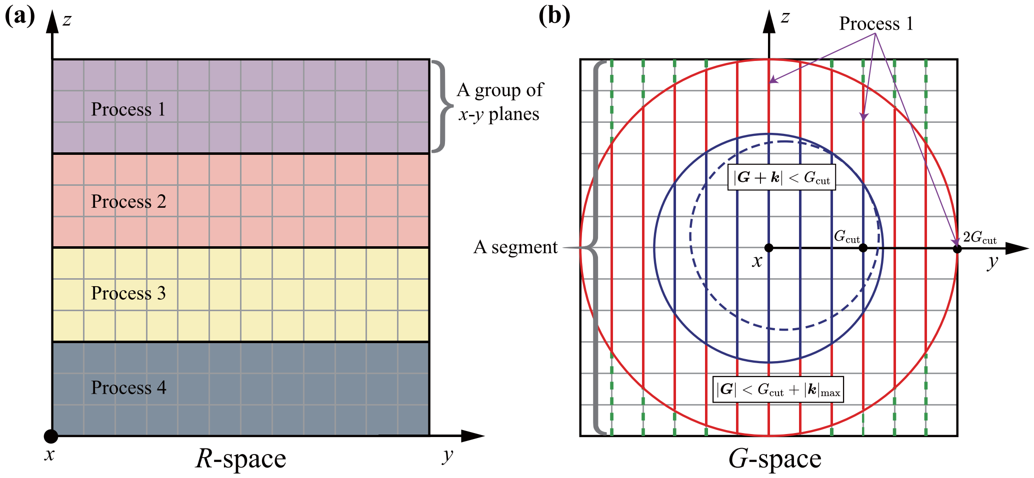

Figure 16. A scheme of parallelization between R-space grid and G-space plane-wave basis. (a) The groups of x–y planes are assigned to various processes in R-space. (b) In G-space, segments parallel to the z-axis are distributed to different processes in a discontinuous manner.

out for the x–y parts of R-space, only after which communication among processes follows. Usually, one utilizes the message passing interface (MPI) for parallel computing. To continue the FFT along the z-direction, data synchronization must be achieved. That is to say, each process should obtain the desired data from other processes, to collect sufficient information for the segments (along the z-direction) assigned to it. Note that each process does not need all the data, since it only accounts for a few segments in G-space. Therefore, the memory usage is minimized. A final FFT for the z-direction finishes the entire procedure. The inverse FFT operation has the inverted sequence. Each process first does FFT^{-1} for its corresponding segments. The FFT^{-1} along x- and y-directions is carried out after data synchronization.

It is important to note that, in G-space, not all reciprocal lattice points on the grid belong to the plane-wave basis set when performing FFT^{-1} of the wavefunction or potential. Only those points satisfying $|\boldsymbol{G}+\boldsymbol{k}| \leqslant G_{\mathrm{cut}}$ or $|\boldsymbol{G}| \leqslant 2G_{\mathrm{cut}}$ are resorted to. In figure 16(b), the green dashed lines in G-space represent the regions where the plane-wave basis set is entirely unnecessary. During the procedure of FFT^{-1}, these points have zero contribution, and their corresponding coefficients do not need to be stored. The region enclosed by the red circle corresponds to $|\boldsymbol{G}| \leqslant 2G_{\mathrm{cut}}$, which is independent of the selected $\boldsymbol{k}$ point. The region marked by the blue dashed line corresponds to $|\boldsymbol{G}+\boldsymbol{k}| \leqslant G_{\mathrm{cut}}$, where the plane waves actually vary with respect to the $\boldsymbol{k}$ point. To account for this, it can be reformulated as $|\boldsymbol{G}| \leqslant G_{\mathrm{cut}} + |\boldsymbol{k}|_{\max}$, such that the region enclosed by the solid blue circle in the figure encompasses the plane-wave bases for all desired $\boldsymbol{k}$ points. Consequently, the G-space can be divided into two distinct basis sets: the red circle serves as the basis set for the charge density and potential, while the solid blue circle serves as the basis set for the wavefunctions.

Accordingly, in specifying the segments in G-space, equal-spacing assignment is not preferred, since various processes may have quite distinct loads. Here, we list a scheme in which the points corresponding to the plane-wave bases on each segment are sorted in descending order based on the number of plane waves. Assume there are M cores and N segments, with $N > M$. In the beginning, the first M segments are randomly assigned to the M cores. Subsequently, the next segment is assigned to the process with the fewest plane waves at the moment. And such assignment repeats for N–M times until all segments find their computing units. As shown in figure 16(b), the segments owned by Process-1 are not continuous. This scheme ensures that the number of plane waves assigned to each process remains comparable, leading to a balanced computational workload across processes. Consequently, it prevents inefficient scenarios characterized by prolonged idle time due to uneven load distribution. For instance, the computation of $\left\langle \psi_i \middle| \widehat{H} \middle| \psi_j \right\rangle$ essentially involves taking the inner product of two vectors, $\langle \psi_i|$ and $\widehat{H}|\psi_j\rangle$. Each process calculates the inner products using its partial plane-wave basis set, yielding a partial result. The overall time cost for this step is determined by the latest completed partial computation among all processes, thus a balanced load distribution is quite necessary. The final result is obtained by summing up these partial contributions across all processes. The diagonalization of the subspace Hamiltonian is performed by a single process, which then broadcasts the eigenvalues and eigenvectors back to all other processes. Subsequently, each process independently carries out additional operations, such as orthogonalization, in parallel.

4.5.2. *Parallelization in bands.*

This methodology divides the energy bands into groups, while each group is assigned a process. For a large supercell with many bands, this becomes extremely efficient. However, in this case the original conjugate gradient method is not applicable, since it has to be carried out in a band-by-band manner, using the known lower energy states as constraints. To address this limitation, the modified pre-conditioned conjugate gradient method by Payne and coworkers [9] should be employed. This improved algorithm enables simultaneous updates of all wavefunctions, making it inherently adaptable for band-parallel computations. The blocked Davidson method [114] is also suitable for parallelization in bands. After each process finishes its relevant energy band calculation, a global optimization is usually required to ensure that the wavefunctions are orthogonal to each other. The communication load among processes is much lighter compared with R/G parallelization, because now the wavefunction for a specific band is stored within a single process, which enables FFT calculations independently. Yet, the real space grid is not separated, which means that each process should maintain a complete grid. Hence, the memory usage is relatively high in this scheme.

4.5.3. Parallelization in $\boldsymbol{k}$ points.

Since the electronic structure of a solid is calculated by specifying a $\boldsymbol{k}$ point first, parallelization in $\boldsymbol{k}$ points is a natural strategy. All the $\boldsymbol{k}$ points are divided into groups, and each group is treated as an individual process. The communication between processes only occurs after the energy eigenvalues and electronic eigenfunctions are obtained for all $\boldsymbol{k}$ points. To calculate the electron density, one must combine the information from all distinct $\boldsymbol{k}$ points. Hence, to be parallel in $\boldsymbol{k}$ points is an efficient scheme, and more CPUs can be used in case there are many $\boldsymbol{k}$ points. The memory usage is also relatively heavy, since each process has to maintain its own real-space grid.

The schemes above may be used jointly according to the practical computational resources. For example, band parallelization may be established upon $\boldsymbol{k}$-point parallelization. Or, the $\boldsymbol{k}$-point parallelization may be applied together with R/G parallelization. That is to say, grid–wavefunction parallelization is further carried out for each well-specified $\boldsymbol{k}$-point.

4.6. Common available codes

Thus far, there have been many computer code implementations of the plane wave–pseudopotential method, and here we could only cover some famous published codes, or those are commercially available. Most of these codes emphasize the application in solid-state and materials science, where the plane wave basis is appropriate, though molecular calculations are in general also permitted through setting up a big box that repeats periodically.

CASTEP (Cambridge sequential total energy package) [125, 126] is one of the earliest plane wave–pseudopotential codes, which was initially developed by Payne and co-workers in the late 1980s. It is designed specially for solid-state materials science, and supports both NCPPs and USPPs. The robust conjugate gradient algorithm is utilized to solve the Hamiltonian, in a fashion of direct energy minimization. The code is very powerful in structural optimization, and it has several integrated modules that deserve special mentioning. The nuclear magnetic resonance (NMR) module enables analyzing the results of solid-state NMR experiments through calculation. And the scanning tunneling microscopy (STM) analysis tool can be used to model STM images at various bias voltages, obtaining the surface structures based on experimental data. CASTEP has full support for mechanical parameters and phonon calculations, even including thermodynamic properties. It has user-friendly graphic interface as integrated into the commercial Materials Studio software, but CASTEP itself now offers free license (Linux version only) for academic use.

VASP (Vienna *ab initio* simulation package) is a commercial code developed mainly by the Kresse group [112, 113] from University of Vienna. It is based on USPP as well as the PAW method, where the implementation of PAW is currently dominating for its application. The full set of PAW potentials by the VASP group was carefully tested in various environments, and the quality of these potentials has been well accepted by the scientific community. It mainly utilizes iterative diagonalization methods such as blocked Davidson and residual minimization (RMM)-DIIS. The code supports DFT + U, van der Waals correction, hybrid functionals, GW calculations as well as solving the Bethe-Salpeter equation (BSE) [127, 128], and performs well for magnetic systems. The full support for GW calculation is one of the prominent features of VASP, which is enabled by recovering the full electron wavefunctions in the PAW formalism. It also supports DFPT and finite difference-based calculations, but phonon calculations are enabled through the joint usage of other codes such as Phonopy and Phono3py [129, 130]. The parallel efficiency of VASP is remarkable, thus it is particularly suitable for the *ab initio* simulation of large supercells.

ABINIT [131, 132] is another widely used plane wave–pseudopotential code that was published in the 1990s, developed and maintained by Gonze and coworkers. As a free and open source package, it was written in Fortran 90. It utilizes DFT, DFPT and many-body perturbation theory to obtain the material properties such as total energy, electronic structure, vibrational and thermodynamic properties, dielectric and non-linear optical properties, and related spectra. It supports meta-GGA [43, 133], time-dependent DFT (TDDFT) [134], GW as well as BSE calculations, using NCPPs as well the PAW method, and has genuine modules for phonon calculations and electron-phonon coupling. ABINIT is a pioneer in the open source solution to *ab initio* calculations, and it has also stimulated the PseudoDojo project [135], which provides server tools to generate pseudopotentials and to validate them against all-electron results.

Quantum Espresso (quantum open source package for research in electronic structure, simulation, and optimization) [136–138] is also an open source software package that simulates materials properties using plane waves and pseudopotentials. It has many modules, among which PWSCF is the central one, accounting for the self-consistent electronic structure calculation. It also has a CP module that carries out Car-Parrinello molecular dynamics [139] simulation. The package supports massive parallelization using OpenMP [140] and MPI jointly, and it is working on graphical processing units (GPUs) since 2021. As an extremely flexible and extendable software, it uses NCPP, USPP as well as the PAW method, and even mixed application of various pseudopotentials is permitted. Electron-phonon coupling and transition state searching are some of the remarkable functionalities of the package. An excellent community is also one of the core features of Quantum Espresso. For example, there is an active mailing list that exchanges questions and answers. New plug-ins and new algorithms can be afforded by the users. The package is maintained and further developed mainly by Giannozzi and Delugas, and it has contributors from all over the world.

CP2K [141] is another widely used program that can perform atomistic simulations of solid state, liquid, molecular, periodic crystal and biological systems. A special feature lies in that, it uses an optimized mixed Gaussian and plane waves approach based on pseudopotentials, though one may also use pure plane waves or pure Gaussian basis sets. The code is maintained by the CP2K foundation founded in Zürich, by Hutter, VandeVondele and Schütt. It is written in Fortran 2008 and can run efficiently in parallel using a combination of multi-threading, MPI, and compute unified device architecture (CUDA). It is freely available under the general public license (GPL). Besides DFT, it allows for post Hartree-Fock calculations as well, and supports *ab initio* molecular dynamics, semi-empirical methods (such as those based on tight binding), and multiscale quantum mechanics/molecular mechanics (QM/MM) simulation.

ABACUS (atomic-orbital based *ab-initio* computation at USTC) is an open source *ab initio* code developed by the He group from University of Science and Technology of China [142, 143], written in C++ 11. It supports both plane wave basis and numerical atomic orbital bases. For plane-wave implementation, it includes certain formats of pseudopotentials such as NCPP and USPP. A special feature of ABACUS lies in that it utilizes highly modular programming with abstract classes, thus the code is relatively easy to read and comprehend. Its plane-wave basis set is primarily utilized for high-throughput calculation of materials datasets, such as preparing training datasets for machine learning potential methods. Furthermore, ABACUS also supports stochastic DFT calculation methods geared towards dense material computations at high temperatures.

GPAW (grid-based projector-augmented wave) [144–146] is an open source DFT code written in Python combined with C, mainly by researchers from the Technical University of Denmark. It is based on the PAW method and the atomic simulation environment (ASE, a Python library) [147]. Besides using the plane wave basis set (PW mode), the code also supports other two modes to represent the wavefunctions. The so-called finite-difference (FD) mode represents the wavefunctions on real-space grids, which can be subject to more flexible boundary conditions. And a basis of numerical atom-centered orbitals in the linear combination of atomic orbitals (LCAOs) mode may also be adopted, in case large supercells are being handled. The three distinct modes bring additional flexibility. For instance, a rough structural optimization may be carried out within the LCAO mode, followed by more accurate calculations in the PW or FD mode.

PWmat is a commercial plane wave–pseudopotential code for material simulations using DFT, developed by the Wang group [148, 149]. With emphasis on GPU-acceleration, it utilizes an innovative mixed single-double precision algorithm. For instance, it was reported in 2019 [150] that a 550-atom supercell was successfully simulated in 6 h using the Heyd-Scuseria-Ernzerhof (HSE) hybrid functional [57, 151], with 8 GPU cards and the PWmat software.

We have not yet mentioned other plane wave (linear APW)-based codes that perform all-electron calculations rather than pseudopotential calculations, such as WIEN2k [47], Exciting [152], and Elk [153]. Some quantum chemistry packages also support plane wave–pseudopotential calculations, such as NWChem [154]. The well-known CPMD package [155] is also based on the plane wave basis set and pseudopotentials, but it is more targeted at *ab initio* molecular dynamics simulations. There are also many other DFT codes for solids, whose basis sets make use of local orbitals, including Siesta [48], OpenMX [72, 156, 157], FHI-aims [158], CRYSTAL [159], BAND [160], ONETEP [161], CONQUEST [162], *etc*. Many of these codes emphasize the linear-scaling computational efficiency, which is however not possible when using a plane-wave basis set.

5. Summary

In summary, we have reviewed the fundamental principles in the band structure calculation for a solid, with emphasis placed on self-consistent calculation, where the treatment of exchange and correlation has become a key factor influencing the accuracy. In this sense, DFT demonstrates its significance. The orthogonal plane-wave basis is very suitable for solid-state calculations, but the relatively large size of the basis requires key techniques such as the introduction of pseudopotentials. The original NCPPs, Kleinman-Bylander type, Vanderbilt's USPP, the projector augmented-wave method as well as the ONCV pseudopotential have been explained and discussed. Finally, it is demonstrated how to construct the Hamiltonian and how to solve it efficiently. Several points specific to code development have also been included for discussion.

Data availability statement

No new data were created or analysed in this study.

Acknowledgment

This work was supported by the National Natural Science Foundation of China under Grant No. 12474230.

ORCID iDs

Shengxin Yang https://orcid.org/0000-0002-8736-2180
Kan-Hao Xue https://orcid.org/0000-0002-2894-7912
Xiangshui Miao https://orcid.org/0000-0002-0546-7692

References

[1] Phillips J C 1962 Band structure of silicon, germanium, and related semiconductors *Phys. Rev.* **125** 1931–6

[2] Imhof S and Thränhardt A 2010 Phonon-assisted transitions and optical gain in indirect semiconductors *Phys. Rev. B* **82** 085303

[3] Bechstedt F and Belabbes A 2013 Structure, energetics, and electronic states of III–V compound polytypes *J. Phys.: Condens. Matter* **25** 273201

[4] Xue K-H, Yuan J-H, Fonseca L R C and Miao X-S 2018 Improved LDA-1/2 method for band structure calculations in covalent semiconductors *Comput. Mater. Sci.* **153** 493–505

[5] Yang S, Wang X, Liu Y, Wu J, Zhou W, Miao X, Huang L and Xue K-H 2022 Enabling *Ab Initio* material design of IN As/Ga Sb superlattices for infrared detection *Phys. Rev. Appl.* **18** 024058

[6] Huang J, Yang W, Chen Z, Yang S, Xue K-H and Miao X 2024 Why Is the Bandgap of GaP Indirect While That of GaAs and GaN Are Direct? *Phys. Status Solidi RRL* **18** 2300489

[7] Wang S Q and Ye H Q 2002 A plane-wave pseudopotential study on III–V zinc-blende and wurtzite semiconductors under pressure *J. Phys.: Condens. Matter* **14** 9579

[8] Ihm J, Zunger A and Cohen M L 1979 Momentum-space formalism for the total energy of solids *J. Phys. C* **12** 4409–22

[9] Payne M C, Teter M P, Allan D C, Arias T A and Joannopoulos J D 1992 Iterative minimization techniques for *ab initio* total-energy calculations: molecular dynamics and conjugate gradients *Rev. Mod. Phys.* **64** 1045–97

[10] Jones R O 2015 Density functional theory: its origins, rise to prominence, and future *Rev. Mod. Phys.* **87** 897–923

[11] Kryachko E S and Ludeña E V 2014 Density functional theory: foundations reviewed *Phys. Rep.* **544** 123–239

[12] Dreizler R M and Gross E K U 1990 *Density Functional Theory* (Springer)

[13] Singh D J 1994 *Planewaves, Pseudopotentials and the LAPW Method* (Springer)

[14] Parr R G and Weitao Y 1995 *Density-Functional Theory of Atoms and Molecules* (Oxford University Press)

[15] Koch W and Holthausen M C 2001 *A Chemist's Guide to Density Functional Theory* (Wiley)

[16] Fiolhais C, Nogueira F and Marques M A L 2003 *A Primer in Density Functional Theory* vol 620 (Springer)

[17] Sholl D S and Steckel J A 2009 *Density Functional Theory: A Practical Introduction* (Wiley)

[18] De Broglie L 1923 Waves and Quanta *Nature* **112** 540

[19] Bloch F 1929 Uber die Quantenmechanik der Elektronen in Kristallgittern *Z. Für Phys.* **52** 555–600

[20] Alase A, Cobanera E, Ortiz G and Viola L 2017 Generalization of Bloch's theorem for arbitrary boundary conditions: theory *Phys. Rev. B* **96** 195133

[21] Herman F and Callaway J 1953 Electronic structure of the germanium crystal *Phys. Rev.* **89** 518–9

[22] Chelikowsky J R and Cohen M L 1976 Nonlocal pseudopotential calculations for the electronic structure of eleven diamond and zinc-blende semiconductors *Phys. Rev. B* **14** 556–82

[23] Griffiths D J 2018 *Introduction to Quantum Mechanics* (Cambridge University Press)

[24] Makov G and Payne M C 1995 Periodic boundary conditions in *ab initio* calculations *Phys. Rev. B* **51** 4014–22

[25] Hartree D R 1928 The wave mechanics of an atom with a non-coulomb central field. Part I. theory and methods *Math. Proc. Camb. Phil. Soc.* **24** 89–110

[26] Andrews S B, Burton N A, Hillier I H, Holender J M and Gillan M J 1996 Molecular electronic structure calculations employing a plane wave basis: a comparison with Gaussian basis calculations *Chem. Phys. Lett.* **261** 521–6

[27] Fan L and Ziegler T 1991 The influence of self-consistency on nonlocal density functional calculations *J. Chem. Phys.* **94** 6057–63

[28] Cui H, Yang S, Xue K-H, Huang J and Miao X 2023 On the self-consistency of DFT-1/2 *J. Chem. Phys.* **158** 094103

[29] De Pablo J J *et al* 2019 New frontiers for the materials genome initiative *npj Comput. Mater.* **5** 41

[30] Born M and Oppenheimer R 1927 Zur Quantentheorie der Molekeln *Ann. Phys.* **389** 457–84

[31] Phillips J C 1958 Energy-band interpolation scheme based on a pseudopotential *Phys. Rev.* **112** 685–95

[32] Hohenberg P and Kohn W 1964 Inhomogeneous electron gas *Phys. Rev.* **136** B864–71

[33] Kohn W and Sham L J 1965 Self-consistent equations including exchange and correlation effects *Phys. Rev.* **140** A1133–8

[34] Thomas L H 1927 The calculation of atomic fields *Math. Proc. Camb. Phil. Soc.* **23** 542–8

[35] Fermi E 1927 Un metodo statistico per la determinazione di alcune priorietà dell'atomo *Rend. Acad. Dei Lincei* **6** 602–7

[36] Dirac P A M 1930 Note on exchange phenomena in the Thomas atom *Math. Proc. Camb. Phil. Soc.* **26** 376–85

[37] Weizsäcker C F V 1935 Zur Theorie der Kernmassen *Z. Für Phys.* **96** 431–58

[38] Levy M 1979 Universal variational functionals of electron densities, first-order density matrices, and natural spin-orbitals and solution of the *v*-representability problem *Proc. Natl Acad. Sci.* **76** 6062–5

[39] Ceperley D M and Alder B J 1980 Ground state of the electron gas by a stochastic method *Phys. Rev. Lett.* **45** 566–9

[40] Xie Q-X, Wu J and Zhao Y 2021 Accurate correlation energy functional for uniform electron gas from an interpolation ansatz without fitting parameters *Phys. Rev. B* **103** 045130

[41] Becke A D 1988 Density-functional exchange-energy approximation with correct asymptotic behavior *Phys. Rev. A* **38** 3098–100

[42] Perdew J P, Burke K and Ernzerhof M 1996 Generalized gradient approximation made simple *Phys. Rev. Lett.* **77** 3865–8

[43] Tao J, Perdew J P, Staroverov V N and Scuseria G E 2003 Climbing the density functional ladder: nonempirical meta–generalized gradient approximation designed for molecules and solids *Phys. Rev. Lett.* **91** 146401

[44] Zhao Y and Truhlar D G 2008 The M06 suite of density functionals for main group thermochemistry, thermochemical kinetics, noncovalent interactions, excited states, and transition elements: two new functionals and systematic testing of four M06-class functionals and 12 other functionals *Theor. Chem. Acc.* **120** 215–41

[45] Chai J-D and Head-Gordon M 2008 Systematic optimization of long-range corrected hybrid density functionals *J. Chem. Phys.* **128** 084106

[46] Sun J, Ruzsinszky A and Perdew J P 2015 Strongly constrained and appropriately normed semilocal density functional *Phys. Rev. Lett.* **115** 036402

[47] Blaha P, Schwarz K, Tran F, Laskowski R, Madsen G K H and Marks L D 2020 WIEN2k: an APW+lo program for calculating the properties of solids *J. Chem. Phys.* **152** 074101

[48] Soler J M, Artacho E, Gale J D, García A, Junquera J, Ordejón P and Sánchez-Portal D 2002 The SIESTA method for *ab initio* order- *N* materials simulation *J. Phys.: Condens. Matter* **14** 2745–79

[49] Burke K 2012 Perspective on density functional theory *J. Chem. Phys.* **136** 150901

[50] French M, Schwartz R, Stolz H and Redmer R 2009 Electronic band structure of Cu_2O by spin density functional theory *J. Phys.: Condens. Matter* **21** 015502

[51] Hasnip P J, Refson K, Probert M I J, Yates J R, Clark S J and Pickard C J 2014 Density functional theory in the solid state *Phil. Trans. R. Soc. A* **372** 20130270

[52] Mao G-Q, Yan Z-Y, Xue K-H, Ai Z, Yang S, Cui H, Yuan J-H, Ren T-L and Miao X 2022 DFT-1/2 and shell DFT-1/2 methods: electronic structure calculation for semiconductors at LDA complexity *J. Phys.: Condens. Matter* **34** 403001

[53] Fock V 1930 Näherungsmethode zur Lösung des quantenmechanischen Mehrkörperproblems *Z. Phys.* **61** 126–48

[54] Slater J C 1929 The theory of complex spectra *Phys. Rev.* **34** 1293–322

[55] Löwdin P 1995 The historical development of the electron correlation problem *Int. J. Quantum Chem.* **55** 77–102

[56] Becke A D 1993 Density-functional thermochemistry. III. The role of exact exchange *J. Chem. Phys.* **98** 5648–52

[57] Heyd J, Scuseria G E and Ernzerhof M 2003 Hybrid functionals based on a screened Coulomb potential *J. Chem. Phys.* **118** 8207–15

[58] Stephens P J, Devlin F J, Chabalowski C F and Frisch M J 1994 *Ab initio* calculation of vibrational absorption and circular dichroism spectra using density functional force fields *J. Phys. Chem.* **98** 11623–7

[59] Grimme S 2006 Semiempirical hybrid density functional with perturbative second-order correlation *J. Chem. Phys.* **124** 034108

[60] Benighaus T, DiStasio R A, Lochan R C, Chai J-D and Head-Gordon M 2008 Semiempirical double-hybrid density functional with improved description of long-range correlation *J. Phys. Chem. A* **112** 2702–12

[61] Zhang Y, Xu X and Goddard W A 2009 Doubly hybrid density functional for accurate descriptions of nonbond interactions, thermochemistry, and thermochemical kinetics *Proc. Natl Acad. Sci.* **106** 4963–8

[62] Toulouse J, Sharkas K, Brémond E and Adamo C 2011 Communication: rationale for a new class of double-hybrid approximations in density-functional theory *J. Chem. Phys.* **135** 101102

[63] Brémond É, Pérez-Jiménez Á J, Sancho-García J C and Adamo C 2019 Range-separated hybrid density functionals made simple *J. Chem. Phys.* **150** 201102

[64] Pernal K and Giesbertz K J H 2015 Reduced density matrix functional theory (RDMFT) and linear response time-dependent RDMFT (TD-RDMFT) *Density-Functional Methods for Excited States* (Topics in Current Chemistry) vol 368, ed N Ferré, M Filatov and M Huix-Rotllant (Springer) pp 125–83

[65] Gilbert T L 1975 Hohenberg-Kohn theorem for nonlocal external potentials *Phys. Rev. B* **12** 2111–20

[66] Wang J and Baerends E J 2022 Self-consistent-field method for correlated many-electron systems with an entropic cumulant energy *Phys. Rev. Lett.* **128** 013001

[67] Liu D, Yan B, Irimia M and Wang J 2024 Potential energy curves for F_2, Cl_2, and Br_2 with the *i*-DMFT method *J. Chem. Phys.* **161** 044118

[68] Liu D, Irimia M, Wang J and Yan B 2025 Potential energy curves of hydrogen halides HX(F, Cl, Br) with the *i*-DMFT method *J. Phys. Chem. A* **129** 415–22

[69] Francl M M, Pietro W J, Hehre W J, Binkley J S, Gordon M S, DeFrees D J and Pople J A 1982 Self-consistent molecular orbital methods. XXIII. A polarization-type basis set for second-row elements *J. Chem. Phys.* **77** 3654–65

[70] Wannier G H 1937 The structure of electronic excitation levels in insulating crystals *Phys. Rev.* **52** 191–7

[71] Marzari N and Vanderbilt D 1997 Maximally localized generalized Wannier functions for composite energy bands *Phys. Rev. B* **56** 12847–65

[72] Ozaki T and Kino H 2004 Numerical atomic basis orbitals from H to Kr *Phys. Rev. B* **69** 195113

[73] Phillips J C and Kleinman L 1959 New method for calculating wave functions in crystals and molecules *Phys. Rev.* **116** 287–94

[74] Schwerdtfeger P 2011 The pseudopotential approximation in electronic structure theory *ChemPhysChem* **12** 3143–55

[75] Herring C 1940 A new method for calculating wave functions in crystals *Phys. Rev.* **57** 1169–77

[76] Slater J C 1937 Wave functions in a periodic potential *Phys. Rev.* **51** 846–51

[77] Hellmann H 1935 A new approximation method in the problem of many electrons *J. Chem. Phys.* **3** 61

[78] Hamann D R, Schlüter M and Chiang C 1979 Norm-conserving pseudopotentials *Phys. Rev. Lett.* **43** 1494–7

[79] Kleinman L and Bylander D M 1982 Efficacious form for model pseudopotentials *Phys. Rev. Lett.* **48** 1425–8

[80] Vanderbilt D 1990 Soft self-consistent pseudopotentials in a generalized eigenvalue formalism *Phys. Rev. B* **41** 7892–5

[81] Blöchl P E 1994 Projector augmented-wave method *Phys. Rev. B* **50** 17953–79

[82] Baroni S, Giannozzi P and Testa A 1987 Green's-function approach to linear response in solids *Phys. Rev. Lett.* **58** 1861–4

[83] Hamann D R 2013 Optimized norm-conserving Vanderbilt pseudopotentials *Phys. Rev. B* **88** 085117

[84] Weeks J D, Hazi A and Rice S A 1969 On the use of pseudopotentials in the quantum theory of atoms and molecules *Advances in Chemical Physics* vol 16, ed I Prigogine and S A Rice (Wiley) pp 283–342

[85] Cohen M L 1984 Electronic structure of solids *Phys. Rep.* **110** 293–309

[86] Pickett W E 1989 Pseudopotential methods in condensed matter applications *Comput. Phys. Rep.* **9** 115–97

[87] Stoll H, Metz B and Dolg M 2002 Relativistic energy-consistent pseudopotentials—recent developments *J. Comput. Chem.* **23** 767–78

[88] Cohen M L 2009 Fifty years of pseudopotentials *Int. J. Quantum Chem.* **24** 583–95

[89] Herring C and Hill A G 1940 The theoretical constitution of metallic beryllium *Phys. Rev.* **58** 132–62

[90] Antončík E 1959 Approximate formulation of the orthogonalized plane-wave method *J. Phys. Chem. Solids* **10** 314–20

[91] Louie S G, Froyen S and Cohen M L 1982 Nonlinear ionic pseudopotentials in spin-density-functional calculations *Phys. Rev. B* **26** 1738–42

[92] Mehrem R 2011 The plane wave expansion, infinite integrals and identities involving spherical Bessel functions *Appl. Math. Comput.* **217** 5360–5

[93] Bachelet G B, Hamann D R and Schlüter M 1982 Pseudopotentials that work: from H to Pu *Phys. Rev. B* **26** 4199–228

[94] Kerker G P 1980 Non-singular atomic pseudopotentials for solid state applications *J. Phys. C* **13** L189–94

[95] Troullier N and Martins J L 1991 Efficient pseudopotentials for plane-wave calculations *Phys. Rev. B* **43** 1993–2006

[96] Grinberg I, Ramer N J and Rappe A M 2000 Transferable relativistic Dirac-Slater pseudopotentials *Phys. Rev. B* **62** 2311–4

[97] Slater J C 1964 Energy band calculations by the augmented plane wave method *Advances in Quantum Chemistry* vol 1 (Elsevier) pp 35–58

[98] Hedin L 1965 New method for calculating the one-particle Green's function with application to the electron-gas problem *Phys. Rev.* **139** A796–823

[99] Kresse G and Joubert D 1999 From ultrasoft pseudopotentials to the projector augmented-wave method *Phys. Rev. B* **59** 1758–75

[100] Rappe A M, Rabe K M, Kaxiras E and Joannopoulos J D 1990 Optimized pseudopotentials *Phys. Rev. B* **41** 1227–30

[101] Löwdin P 1950 On the non-orthogonality problem connected with the use of atomic wave functions in the theory of molecules and crystals *J. Chem. Phys.* **18** 365–75

[102] Hamann D R 2017 Erratum: optimized norm-conserving Vanderbilt pseudopotentials [Phys. Rev. B 88, 085117 (2013)] *Phys. Rev. B* **95** 239906

[103] Methfessel M and Paxton A T 1989 High-precision sampling for Brillouin-zone integration in metals *Phys. Rev. B* **40** 3616–21

[104] Monkhorst H J and Pack J D 1976 Special points for Brillouin-zone integrations *Phys. Rev. B* **13** 5188–92

[105] Perdew J P and Wang Y 1992 Accurate and simple analytic representation of the electron-gas correlation energy *Phys. Rev. B* **45** 13244–9

[106] Fujishita H, Shiozaki Y and Sawaguchi E 1979 X-ray crystal structure analysis of low temperature phase of $SrTiO_3$ *J. Phys. Soc. Jpn.* **46** 581–6

[107] Martin R M 2004 *Electronic Structure: Basic Theory and Practical Methods* (Cambridge University Press)

[108] Ewald P P 1921 Die Berechnung optischer und elektrostatischer Gitterpotentiale *Ann. Phys.* **369** 253–87

[109] Lee H B and Cai W Ewald summation for coulomb interactions in a periodic supercell

[110] Lanczos C 1950 An iterative method for the solution of the eigenvalue problem of linear differential and integral *J. Res. Natl Bur. Stand* **45** 255–82

[111] Arnoldi W E 1951 The principle of minimized iterations in the solution of the matrix eigenvalue problem *Q. Appl. Math.* **9** 17–29

[112] Kresse G and Furthmüller J 1996 Efficient iterative schemes for *ab initio* total-energy calculations using a plane-wave basis set *Phys. Rev. B* **54** 11169–86

[113] Kresse G and Furthmüller J 1996 Efficiency of *ab-initio* total energy calculations for metals and semiconductors using a plane-wave basis set *Comput. Mater. Sci.* **6** 15–50

[114] Davidson E R 1975 The iterative calculation of a few of the lowest eigenvalues and corresponding eigenvectors of large real-symmetric matrices *J. Comput. Phys.* **17** 87–94

[115] Morgan R B 1990 Davidson's method and preconditioning for generalized eigenvalue problems *J. Comput. Phys.* **89** 241–5

[116] Krylov A N 1931 On the numerical solution of the equation by which the frequency of small oscillations is determined in technical problems *Izv SSSR* **VII** 491–539

[117] Siklitskaya A, Bednarek T, Pogrebetsky J and Kubas A 2025 An overview of physical and chemical long-range phenomena governed by Friedel oscillations: a bridge between physics and chemistry *Mater. Chem. Front.* **9** 541–79

[118] Kerker G P 1981 Efficient iteration scheme for self-consistent pseudopotential calculations *Phys. Rev. B* **23** 3082–4

[119] Pulay P 1980 Convergence acceleration of iterative sequences. the case of scf iteration *Chem. Phys. Lett.* **73** 393–8

[120] Anderson D G 1965 Iterative procedures for nonlinear integral equations *J. ACM* **12** 547–60

[121] Broyden C G 1965 A class of methods for solving nonlinear simultaneous equations *Math. Comput.* **19** 577–93

[122] Vanderbilt D and Louie S G 1984 Total energies of diamond (111) surface reconstructions by a linear combination of atomic orbitals method *Phys. Rev. B* **30** 6118–30

[123] Johnson D D 1988 Modified Broyden's method for accelerating convergence in self-consistent calculations *Phys. Rev. B* **38** 12807–13

[124] Sherman J and Morrison W J 1950 Adjustment of an inverse matrix corresponding to a change in one element of a given matrix *Ann. Math. Stat.* **21** 124–7

[125] Clark S J, Segall M D, Pickard C J, Hasnip P J, Probert M I J, Refson K and Payne M C 2005 First principles methods using CASTEP *Z. Krist.—Cryst. Mater.* **220** 567–70

[126] Milman V, Winkler B, White J A, Pickard C J, Payne M C, Akhmatskaya E V and Nobes R H 2000 Electronic structure, properties, and phase stability of inorganic crystals: a pseudopotential plane-wave study *Int. J. Quantum Chem.* **77** 895–910

[127] Salpeter E E and Bethe H A 1951 A relativistic equation for bound-state problems *Phys. Rev.* **84** 1232–42

[128] Hanke W and Sham L J 1979 Many-particle effects in the optical excitations of a semiconductor *Phys. Rev. Lett.* **43** 387–90

[129] Togo A and Tanaka I 2015 First principles phonon calculations in materials science *Scr. Mater.* **108** 1–5

[130] Togo A 2023 First-principles phonon calculations with phonopy and Phono3py *J. Phys. Soc. Jpn.* **92** 012001

[131] Gonze X *et al* 2009 ABINIT: first-principles approach to material and nanosystem properties *Comput. Phys. Commun.* **180** 2582–615

[132] Gonze X *et al* 2020 The Abinit project: impact, environment and recent developments *Comput. Phys. Commun.* **248** 107042

[133] Tran F and Blaha P 2009 Accurate band gaps of semiconductors and insulators with a semilocal exchange-correlation potential *Phys. Rev. Lett.* **102** 226401

[134] Ullrich C A 2011 *Time-Dependent Density-Functional Theory: Concepts and Applications* (Oxford University Press)

[135] Van Setten M J, Giantomassi M, Bousquet E, Verstraete M J, Hamann D R, Gonze X and Rignanese G-M 2018 The PseudoDojo: training and grading a 85 element optimized norm-conserving pseudopotential table *Comput. Phys. Commun.* **226** 39–54

[136] Giannozzi P *et al* 2009 QUANTUM ESPRESSO: a modular and open-source software project for quantum simulations of materials *J. Phys.: Condens. Matter* **21** 395502

[137] Giannozzi P *et al* 2017 Advanced capabilities for materials modelling with Quantum ESPRESSO *J. Phys.: Condens. Matter* **29** 465901

[138] Giannozzi P *et al* 2020 Quantum ESPRESSO toward the exascale *J. Chem. Phys.* **152** 154105

[139] Car R and Parrinello M 1985 Unified approach for molecular dynamics and density-functional theory *Phys. Rev. Lett.* **55** 2471–4

[140] Beyer J C, Stotzer E J, Hart A and De Supinski B R 2011 *OpenMP for Accelerators OpenMP in the Petascale Era* (Lecture Notes in Computer Science) vol 6665, ed B M Chapman, W D Gropp, K Kumaran and M S Müller (Springer) pp 108–21

[141] Hutter J, Iannuzzi M, Schiffmann F and VandeVondele J 2014 CP2K: atomistic simulations of condensed matter systems *Wiley Interdiscip. Rev. Comput. Mol. Sci.* **4** 15–25

[142] Li P, Liu X, Chen M, Lin P, Ren X, Lin L, Yang C and He L 2016 Large-scale *ab initio* simulations based on systematically improvable atomic basis *Comput. Mater. Sci.* **112** 503–17

[143] Lin P, Ren X, Liu X and He L 2024 *Ab initio* electronic structure calculations based on numerical atomic orbitals: basic fomalisms and recent progresses *Wiley Interdiscip. Rev. Comput. Mol. Sci.* **14** e1687

[144] Mortensen J J, Hansen L B and Jacobsen K W 2005 Real-space grid implementation of the projector augmented wave method *Phys. Rev. B* **71** 035109

[145] Enkovaara J *et al* 2010 Electronic structure calculations with GPAW: a real-space implementation of the projector augmented-wave method *J. Phys.: Condens. Matter* **22** 253202

[146] Mortensen J J *et al* 2024 GPAW: an open Python package for electronic structure calculations *J. Chem. Phys.* **160** 092503

[147] Hjorth Larsen A *et al* 2017 The atomic simulation environment—a Python library for working with atoms *J. Phys.: Condens. Matter* **29** 273002

[148] Jia W, Cao Z, Wang L, Fu J, Chi X, Gao W and Wang L-W 2013 The analysis of a plane wave pseudopotential density functional theory code on a GPU machine *Comput. Phys. Commun.* **184** 9–18

[149] Jia W, Fu J, Cao Z, Wang L, Chi X, Gao W and Wang L-W 2013 Fast plane wave density functional theory molecular dynamics calculations on multi-GPU machines *J. Comput. Phys.* **251** 102–15

[150] Liu Y-Y, Zheng F, Jiang X, Luo J-W, Li S-S and Wang L-W 2019 *Ab initio* investigation of charge trapping across the crystalline-Si–amorphous-SiO_2 interface *Phys. Rev. Appl.* **11** 044058

[151] Heyd J, Scuseria G E and Ernzerhof M 2006 Erratum: "Hybrid functionals based on a screened Coulomb potential" [J. Chem. Phys. 118, 8207 (2003)] *J. Chem. Phys.* **124** 219906

[152] Gulans A, Kontur S, Meisenbichler C, Nabok D, Pavone P, Rigamonti S, Sagmeister S, Werner U and Draxl C 2014 Exciting: a full-potential all-electron package implementing density-functional theory and many-body perturbation theory *J. Phys.: Condens. Matter* **26** 363202

[153] The Elk Code (available at: http://elk.sourceforge.net)

[154] Aprà E *et al* 2020 NWChem: past, present, and future *J. Chem. Phys.* **152** 184102

[155] Hutter J, Alavi A, Deutsch T, Bernasconi M, Goedecker S, Marx D, Tuckerman M and Parrinello M (CPMD) (MPI Für Festkörperforschung And IBM Zurich Research Laboratory) (available at: www.cpmd.org)

[156] Ozaki T 2003 Variationally optimized atomic orbitals for large-scale electronic structures *Phys. Rev. B* **67** 155108

[157] Ozaki T and Kino H 2005 Efficient projector expansion for the *ab initio* LCAO method *Phys. Rev. B* **72** 045121

[158] Blum V, Gehrke R, Hanke F, Havu P, Havu V, Ren X, Reuter K and Scheffler M 2009 *Ab initio* molecular simulations with numeric atom-centered orbitals *Comput. Phys. Commun.* **180** 2175–96

[159] Erba A *et al* 2023 CRYSTAL23: a program for computational solid state physics and chemistry *J. Chem. Theory. Comput.* **19** 6891–932

[160] Te Velde G and Baerends E J 1991 Precise density-functional method for periodic structures *Phys. Rev. B* **44** 7888–903

[161] Prentice J C A *et al* 2020 The ONETEP linear-scaling density functional theory program *J. Chem. Phys.* **152** 174111

[162] Nakata A *et al* 2020 Large scale and linear scaling DFT with the CONQUEST code *J. Chem. Phys.* **152** 164112